


Spring 4-15-2019

Detection and classification of vibrating objects in SAR images

Francisco German Perez Venegas
University of New Mexico

Follow this and additional works at: https://digitalrepository.unm.edu/ece_etds

 Part of the [Electrical and Computer Engineering Commons](#), and the [Other Mechanical Engineering Commons](#)

Recommended Citation

Perez Venegas, Francisco German. "Detection and classification of vibrating objects in SAR images." (2019).
https://digitalrepository.unm.edu/ece_etds/455

This Dissertation is brought to you for free and open access by the Engineering ETDs at UNM Digital Repository. It has been accepted for inclusion in Electrical and Computer Engineering ETDs by an authorized administrator of UNM Digital Repository. For more information, please contact amywinter@unm.edu.

Francisco Germán Pérez Venegas

Candidate

Electrical and Computer Engineering

Department

This dissertation is approved, and it is acceptable in quality and form for publication: *Approved*

by the Dissertation Committee:

Dr. Balasubramaniam Santhanam, Chair

Dr. Majeed M. Hayat, Co-Chair

Dr. Walter Gerstle, Member

Dr. Marios Pattichis, Member

Dr. Armin W. Doerry, Member

Detection and classification of vibrating objects in SAR images

by

Francisco Germán Pérez Venegas

B.S. in Engineering, University of Concepción, 2011

M.S. in Electrical Engineering, University of Concepción, 2014

DISSERTATION

Submitted in Partial Fulfillment of the
Requirements for the Degree of

Doctor of Philosophy in Engineering

The University of New Mexico

Albuquerque, New Mexico

May, 2019

©2019, Francisco Germán Pérez Venegas

Dedication

To my parents, Néstor F. and María T., for their unconditional support and encouragement during all these years.

“As caged lion I used to feel in my hometown. Everyday that I was spending there, it was a day that I was wasting. The prejudices were transforming my dreams into nightmares but I couldn’t stop thinking that life was a different thing. Walking around the world I confirmed what I suspected. Life is a party if one does what one loves”

– Facundo Cabral

Acknowledgments

This work was performed at the University of New Mexico and supported by the United States Department of Energy (Award No. DE-NA0002494). The author would like to thank General Atomics Aeronautical Systems, Incorporated (San Diego, CA) for making the Lynx system available for this research. The author acknowledges the support of CONICYT scholarship CONICYT-PCHA, Becas Chile, 2016-72170043.

Detection and classification of vibrating objects in SAR images

by

Francisco Germán Pérez Venegas

B.S. in Engineering, University of Concepción, 2011

M.S. in Electrical Engineering, University of Concepción, 2014

Ph.D., Engineering, University of New Mexico, 2019

Abstract

The vibratory response of buildings and machines contains key information that can be exploited to infer their operating conditions and to diagnose failures. Furthermore, since vibration signatures observed from the exterior surfaces of structures are intrinsically linked to the type of machinery operating inside of them, the ability to monitor vibrations remotely can enable the detection and identification of the machinery.

This dissertation focuses on developing novel techniques for the detection and M-ary classification of vibrating objects in SAR images. The work performed in this dissertation is conducted around three central claims. First, the non-linear transformation that the micro-Doppler return of a vibrating object suffers through SAR sensing does not destroy its information. Second, the *instantaneous frequency* (IF) of the SAR signal has sufficient information to characterize vibrating objects. Third, it is possible to develop a detection model that encompasses multiple scenarios in-

cluding both mono-component and multi-component vibrating objects immersed in noise and clutter.

In order to cement these claims, two different detection and classification methodologies are investigated. The first methodology is data-driven and utilizes features extracted with the help of the *discrete fractional Fourier transform* (DFRFT) to feed *machine-learning algorithms* (MLAs). Specifically, the DFRFT is applied to the IF of the slow-time SAR data, which is reconstructed using techniques of time-frequency analysis. The second methodology is model-based and employs a probabilistic model of the SAR slow-time signal, the *Karhunen-Loève transform* (KLT), and a likelihood-based decision function. The performance of the two proposed methodologies is characterized using simulated data as well as real SAR data. The suitability of SAR for sensing vibrations is demonstrated by showing that the separability of different classes of vibrating objects is preserved even after non-linear SAR processing.

Finally, the proposed algorithms are studied when the range-compressed phase-history data is contaminated with noise and clutter. The results show that the proposed methodologies yields reliable results for *signal-to-noise ratios* (SNRs) and *signal-to-clutter ratios* (SCRs) greater than -5 dB. This requirement is relaxed to SNRs and SCRs greater than -10 dB when the range-compressed phase-history data is pre-processed with the *Hankel rank reduction* (HRR) clutter-suppression technique.

Contents

List of Figures	xiii
List of Tables	xvii
Acronyms	xix
1 Introduction	1
1.1 Overview	1
1.2 Motivation	3
1.3 State of the art	5
1.4 Contributions	8
2 Theoretical background	11
2.1 Motion model	11
2.2 Signal model	12
2.3 Binary hypothesis testing problem	17

Contents

2.4	M-ary hypothesis testing problem	18
3	Binary detection models	20
3.1	Vibration detection scheme based on machine-learning classifiers and the DFRFT	20
3.1.1	Feature extraction	21
3.1.2	Machine-learning classifiers	24
3.2	Vibration detection based on a probabilistic model of the SAR slow- time signal	25
3.2.1	Probabilistic model of the binary hypothesis testing problem .	26
3.2.2	Direct detection approach	27
3.2.3	Detection approach using the KL expansion	28
3.3	Performance evaluation	31
3.3.1	Dataset description	31
3.3.2	Performance metrics	34
3.3.3	Demonstration and performance evaluation	34
3.3.4	Characterization of performance in the presence of noise and clutter	37
4	M-ary detection models	39
4.1	Vibration classification scheme based on machine-learning classifiers and the DFRFT	39

Contents

4.2	Maximum-likelihood M-ary detector based on a probabilistic model of the SAR signal and the Karhunen-Loève expansion	40
4.2.1	Probabilistic model of the M-ary hypothesis testing problem	40
4.2.2	M-ary maximum-likelihood detector based on the KL expansion	43
4.2.3	Optimal data-driven approach for determining the prior probabilities	44
4.3	Performance Evaluation	46
4.3.1	Specification of classes and dataset description	46
4.3.2	Performance metrics	49
4.3.3	Demonstration and performance evaluation	49
4.3.4	Characterization of the performance in presence of noise and clutter	53
5	Preservation of class-separability of vibrations in SAR images	55
5.1	Library of machine vibrations	56
5.2	Separability test	60
5.3	Preservation of the separability in SAR sensing	64
5.4	Classification test using pre-built classifiers	68
6	Clutter-noise suppression via Hankel rank reduction	69
6.1	The Hankel rank reduction method	69

Contents

6.2	Application to the machine-learning-based detection and classification framework	71
6.3	Application to the probabilistic detection and classification framework	73
7	Conclusions	75
7.1	Summary and conclusions	75
7.2	Suggestions for future work	77
A	Vibration detection based on the CSD of the SAR signal	79
B	Smoothed pseudo Wigner-Ville time-frequency distribution	80
C	Multi-angle centered-discrete fractional Fourier transform	82
D	DFRFT-based spectrogram	84
E	Recovering IF signals: SPWVTFD and DFRFT-based spectrogram	86
F	Statistical analysis of clutter-noise in SAR images	91
G	Probability density functions of the direct binary-detection approach	95
H	Covariance matrices for the binary probabilistic detector	99

Contents

I	Karhunen-Loève transform	104
J	Covariance matrices of the M-ary detection problem	106
	References	111

List of Figures

1.1	Synthetic aperture radar operating in spotlight mode	2
1.2	Vibration phenomenology in spotlight SAR	4
1.3	Analysis of vibrating objects in SAR images using the CSD.	6
1.4	Block diagram of the proposed methodologies for the detection and classification of vibrating objects in SAR images.	10
2.1	A three-dimensional SAR flight geometry	12
2.2	Reconstruction of a SAR image from its range-compressed phase history	15
2.3	Example of the slow-time signal for a static and a vibrating targets .	16
3.1	Feature extraction using the SPWVTFD and the DFRFT.	23
3.2	General scheme of the proposed neural network for classification of vibrating objects in SAR images.	25
3.3	Examples of the 2 different types of SAR signatures simulated. . . .	33
3.4	ROC curves of the MLAs for the binary detection problem.	35

List of Figures

3.5	ROC curves of the probabilistic detector for the binary detection problem.	35
3.6	Feature usage of the constructed Random Forest classifier for the binary classification problem.	36
3.7	Performance characterization of the proposed detectors at various noise and clutter intensity levels.	38
4.1	Examples of the 4 different types of SAR signatures simulated. . . .	47
4.2	Signal of interest of the 4 different types of SAR signatures simulated.	48
4.3	Confusion matrices of the MLAs for the quaternary classification problem.	50
4.4	Feature usage of the constructed Random Forest classifier for the quaternary classification problem.	51
4.5	Confusion matrices of the maximum-likelihood M-ary classifier for the quaternary classification problem.	52
4.6	Performance characterization of the proposed M-ary detectors at various noise and clutter intensity levels.	54
5.1	Steps involved in the study of the preservation of class-separability of vibrations in SAR images.	56
5.2	Classes that conform the machine vibration library, Fig. No. 1 of 3.	58
5.3	Classes that conform the machine vibration library, Fig. No. 2 of 3.	59
5.4	Classes that conform the machine vibration library, Fig. No. 3 of 3.	60

List of Figures

5.5	Normalized confusion matrices evaluated on a testing set formed by vibration displacement waveforms.	62
5.6	Eight-class average ROC curve evaluated on a testing set formed by vibration displacement waveforms.	63
5.7	Feature usage of the constructed Random Forest classifier, 8-class classification problem.	63
5.8	Normalized confusion matrices evaluated on a testing set formed by SAR signals generated from vibration displacement waveforms. . . .	66
5.9	Eight-class average ROC curve evaluated on a testing set formed by SAR signals generated from vibration displacement waveforms. . . .	67
5.10	Feature usage of the constructed Random Forest classifier using simulated SAR data, 8-class classification problem.	67
6.1	Performance characterization of the detection and classification algorithms based on MLAs using the HRR technique for noise and clutter suppression.	72
6.2	Performance characterization of the probabilistic detection and classification algorithms using the HRR technique for noise and clutter suppression.	74
E.1	Displacement functions used for the characterization of the SPWTFD and the Piece-wise linear DFRFT-based spectrogram.	88
E.2	SPWTFD applied to slow-time signals with different vibration modulation.	89

List of Figures

E.3	Piece-wise linear DFRFT-based spectrogram applied to slow-time signals with different vibration modulation.	90
F.1	SAR image used for clutter-noise characterization.	92
F.2	Analysis of the clutter-noise signal using histograms.	93
F.3	Distribution of the real part of the clutter-noise signal vs its imaginary part in the complex plane.	94

List of Tables

2.1	SAR system parameters for simulations	17
3.1	Area under the ROC curve of the proposed detectors for the binary detection problem.	36
4.1	Overall accuracy of the proposed M-ary classifiers for the quaternary classification problem.	51
5.1	Separability of displacement waveforms.	61
5.2	Separability of SAR signals generated from displacement waveforms.	64
5.3	Classification of machine vibration data using the binary MLA of Sec. 3.1.	68

List of Algorithms

1	Feature extraction using the DFRFT and time-freq. analysis tools . .	24
2	Vibration detection scheme using a probabilistic model and the KLT.	30
3	M-ary detection of vibrations using a probabilistic model of the SAR signal and the KLT.	45
4	Vibration detection via the generalized likelihood ratio of the CSD . .	79

Acronyms

AUROCC	Area under the ROC curve
CACF	Cyclic autocorrelation function
CSD	Cyclic spectral density
CZT	Chirp z-transform
DFRFT	Discrete fractional Fourier transform
DFT	Discrete Fourier transform
DPCA	Displaced-phase-center antenna
HRR	Hankel rank reduction
IF	Instantaneous frequency
KL	Karhunen-Loève
KLT	Karhunen-Loève transform
MA- CDFRFT	Multi-angle centered-discrete fractional Fourier transform
MLA	Machine-learning algorithm

Acronyms

NN	Neural network
PDF	Probability density function
PFA	Polar-format algorithm
PRF	Pulse-repetition frequency
RCS	Radar cross section
RFC	Random-forest classifier
ROC	Receiver operating characteristic
SAR	Synthetic aperture radar
SCR	Signal-to-clutter ratio
SNR	Signal-to-noise ratio
SoI	Signal of interest
SPWVTFD	Smoothed pseudo Wigner–Ville time-frequency distribution
SVD	Singular-value decomposition
SVM	Support-vector machine
UNM	The University of New Mexico
WVTFD	Wigner–Ville time-frequency distribution

Chapter 1

Introduction

1.1 Overview

Synthetic aperture radar (SAR) is a ubiquitous coherent imaging technique designed for generating high-resolution terrain images. Synthetic aperture radar operates by illuminating the target scene with electromagnetic pulses, typically in the microwave band, and measures the amplitude and phase of the return signal. After substantial signal processing of the collected data, the final product is a two-dimensional image where each pixel in the image represents the reflectivity of a region at the transmitted frequency [1]. The relatively long wavelengths, compared with those of optical sensors, make SAR systems capable of remote imaging over thousands of kilometers regardless of weather conditions. The typical range of these systems can be anywhere from 25km for the Lynx radar¹ [2] to well over 800 km for the RADARSAT-2 [3]. These SAR-collection platforms can generate images at a variety of resolution scales.

¹Lynx is a high resolution, SAR that has been designed and built by General Atomics Aeronautical Systems, Inc., in collaboration with Sandia National Laboratories. The Lynx SAR has been used in various vibrometry experiments coordinated by the SAR research group at the University of New Mexico.

Chapter 1. Introduction

For example, the Lynx radar has the ability to generate 0.1m (4in.) and 0.3m (1ft.) resolution images [2].

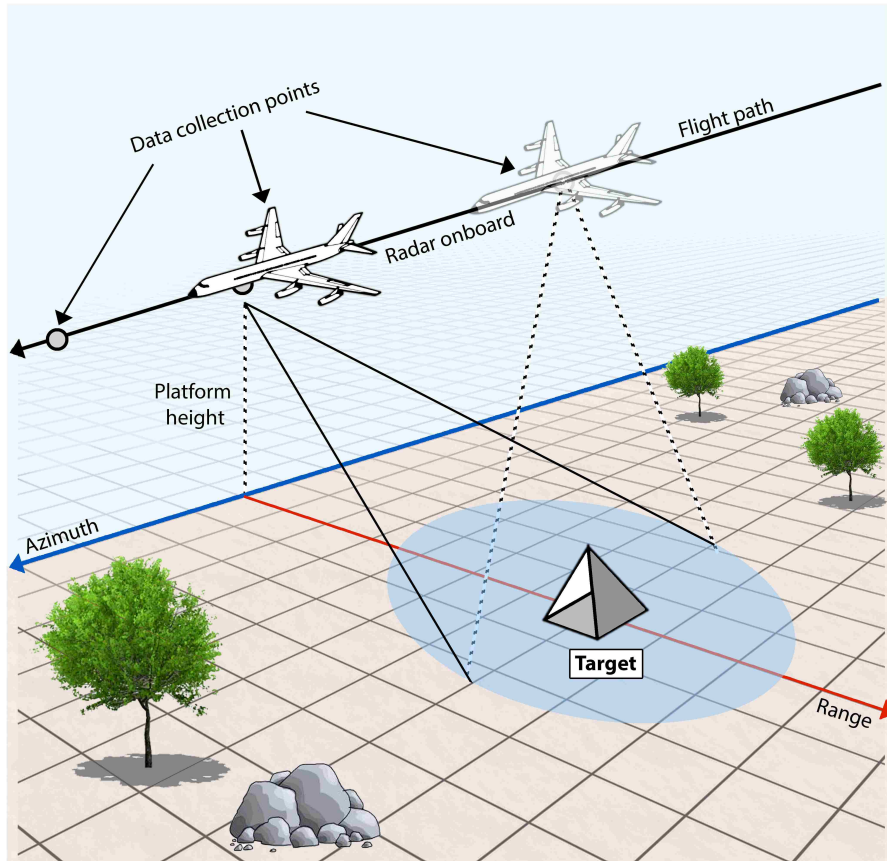


Figure 1.1: Synthetic aperture radar operating in spotlight mode. The radar beam is continually steered to constantly illuminate the same ground patch from all positions of the flight path.

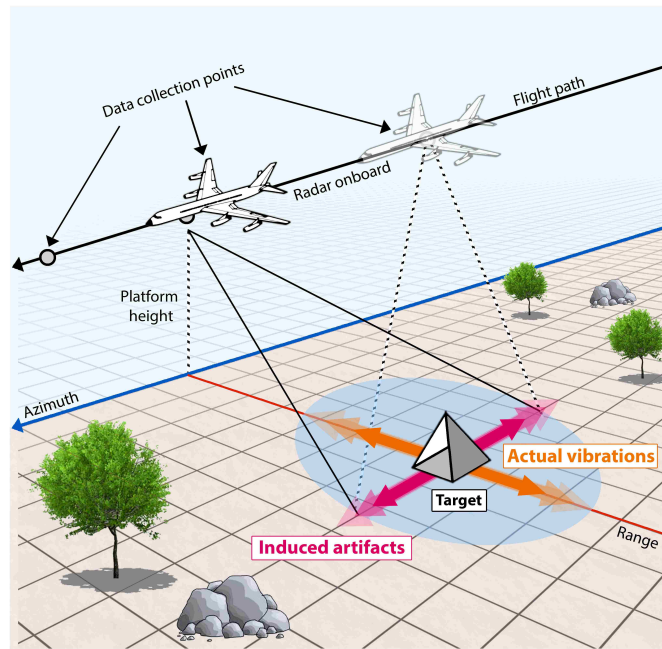
For common imaging applications, a typical airborne SAR platform operating in spotlight-mode illuminates the ground scene for at least several seconds to create a single SAR image. Figure 1.1 shows the typical three-dimensional data acquisition geometry for the spotlight SAR. During the data-collection process, the image formation technique, often the *polar-format algorithm* (PFA) [4], assumes all targets in the

ground scene are static. This assumption, makes SAR particularly sensitive to low-level target vibrations [5–13]. More specifically, ground target vibrations introduce a phase modulation, termed the micro-Doppler effect [10], into each returned SAR signal. Any target, with a strong *radar cross section* (RCS) relative to its surroundings, vibrating in 90° with respect to the flight path will produce observable artifacts in the image called ghost targets. These ghost targets degrade the image quality. An example of these ghost targets is shown in Fig. 1.2. While ground target vibrations may introduce distortion in some regions of a SAR image [5, 10], they contain vital information about the frequency and amplitude of the vibration of a target. In turn, the vibration history, if reliably detected, can aid in the identification of the targets imaged.

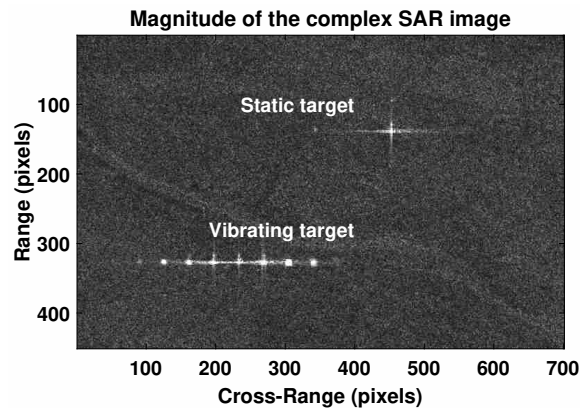
1.2 Motivation

During the past few years, the analysis of mechanical vibration (i.e., vibrometry) has become a prominent field of study. Particularly, the vibratory response of buildings and machines carries key information that can be exploited to infer their operating condition and to diagnose failures. Furthermore, since vibration signatures observed from the exterior surfaces of structures are intrinsically linked to the type of machinery operating inside of them, the ability to monitor vibrations remotely can facilitate the detection and identification of the machinery.

Mechanical vibrations from machines and buildings are normally low in amplitude (app. 1 mm - 10 cm) and low in frequency (app. 1 Hz - 500 Hz). The study of this type of vibrations in SAR images is carried out by analyzing slow-time data. The slow-time data of a SAR image corresponds to all the cross-range slices of the range-compressed phase history data of the SAR image. To date, many high-precision vibration-estimation algorithms have been developed for reconstruct-



(a)



(b)

Figure 1.2: Vibration phenomenology in spotlight SAR. (a) Collection geometry and vibrating target. (b) SAR image containing a static and vibrating target, both with strong RCS. The vibration of the target is in the range direction. The induced ghost artifacts are exhibited in the azimuth (cross-range) direction. The SAR image (b) has a pixel resolution of 4-in and was generated by the GA-ASI Lynx SAR in collaboration with the University of New Mexico for various vibrometry experiments.

Chapter 1. Introduction

ing surface-vibration waveforms from SAR images [14–18]. The next challenge towards a complete characterization and understanding of surface vibrations in SAR images is in the development of algorithms for detecting and classifying vibrating objects based on their SAR signature.

In the past, a method based on a cyclostationary model and the generalized likelihood ratio was proposed to detect vibrating objects from slow-time SAR signals [19]. This detection scheme was based on the correlation between the *cyclic spectral density* (CSD) of a slow-time signal and a stored template of the expected CSD of the vibration. However, the match between a vibration CSD template and the CSD of the input signal is susceptible to errors because the CSD of SAR signals is impulsive in nature, it is affected by signal noise and terrain clutter, and it also changes with the vibration frequency. Furthermore, this detection scheme is unpractical for more complex types of vibrations, such as chirped vibrations, for which the CSD does not produce a reliable characterization. Due to the aforementioned weaknesses of the existing technique for detecting vibrating objects in SAR images, it is clear that new signal-processing methods are needed for detecting and classifying vibrating objects in SAR images.

1.3 State of the art

During the last few years, numerous works have been published on the study of the effects of vibrating objects in SAR images [5–19]. However, among all these works only one has focused on the development of a detection algorithm for vibrating objects in SAR images.

In 1998, *Subotic et al.* proposed a method based on a cyclostationary model and the generalized likelihood ratio for detecting vibrating objects from slow-time SAR signals [19]. Specifically, they found that the slow-time signal of a vibrating

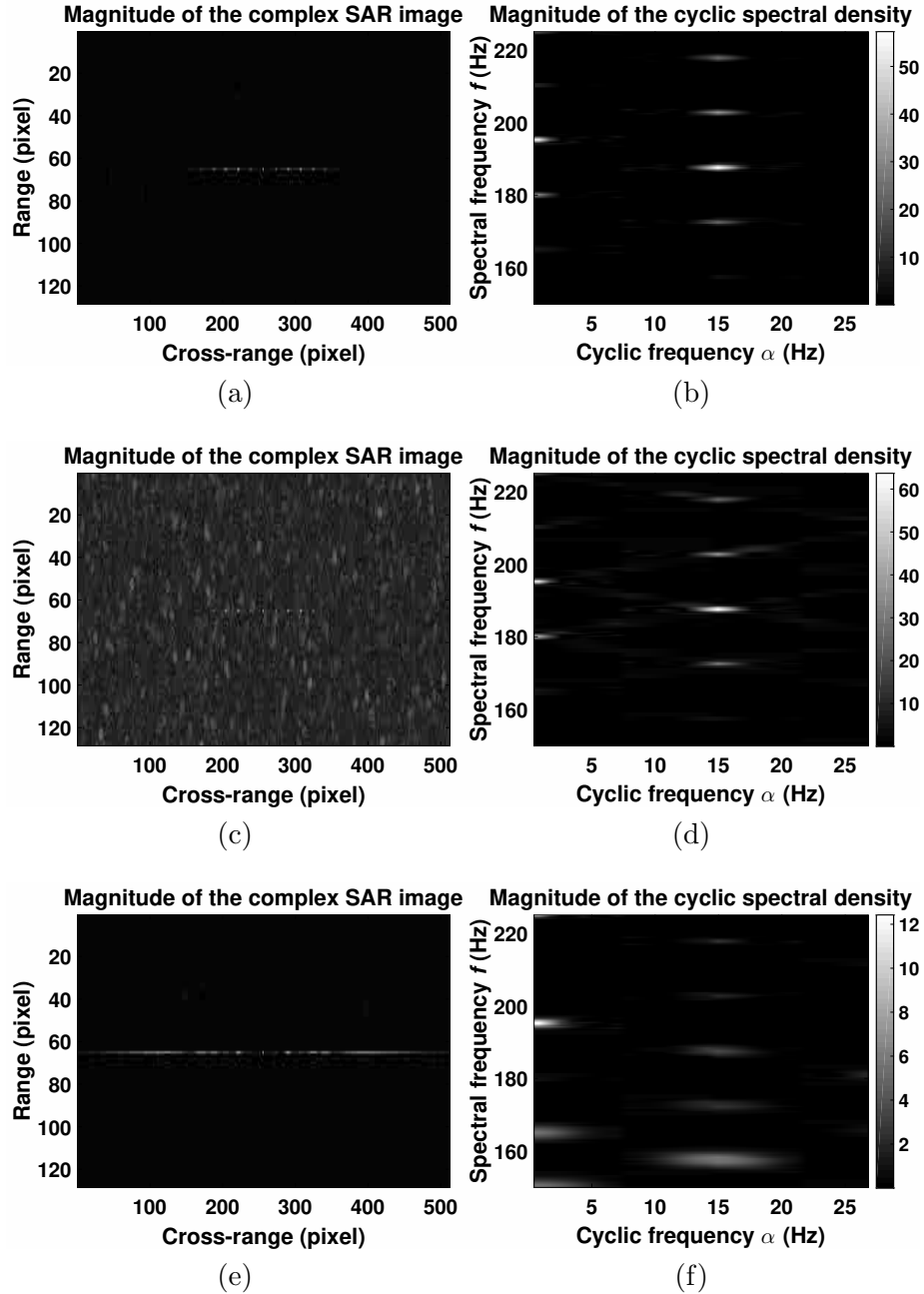


Figure 1.3: Analysis of vibrating objects in SAR images using the CSD. (a) SAR image containing a vibrating point-object with a 1.5 mm, 15 Hz simple sinusoidal vibration. (c) SAR image containing the same object as in (a) with additive clutter and noise at SCR=10dB and SNR=10dB. (e) SAR image containing the same object as in (a) with additional chirp of 1 Hz/s. (b), (d), (f) are the CSD planes of the corresponding slow-time signals at range 65 of (a), (c) and (e), respectively.

Chapter 1. Introduction

object exhibited cyclostationary characteristics as result of the phase modulation that the vibration produces on the slow-time signal. Therefore, if a vibration has a fundamental period τ_0 , then the mean and auto-correlation functions of the slow-time signal are also τ_0 -periodic. Subotic et al. proposed to use the CSD to exploit this cyclostationary property. For every cyclic frequency α , the CSD compresses the periodic information of the *cyclic autocorrelation function* (CACF) via the Fourier transform. As result, the periodic vibration-information of the slow-time signal is mapped to the region of the CSD plane with $\alpha \neq 0$ whereas the stationary clutter is restricted to the region $\alpha = 0$. Subotic et al. proposed to detect vibrations using an approximation of the generalized likelihood ratio, which correlates the CSD of the signal under analysis with a CSD template of the expected vibration. The complete detection scheme is presented in Appx. (A).

Figure 1.3 shows the magnitude of the SAR image and the corresponding CSD for various types of SAR signals. Figure 1.3 (b) shows the CSD for a slow-time signal containing a point-object exhibiting a 1.5 mm, 15 Hz simple sinusoidal vibration. As can be observed, the CSD of this signal exhibits an impulse-like behavior at $\alpha = 15$ due to the phase modulation that the 15 Hz vibration induces on the SAR signal. Figure 1.3 (d) shows the CSD for the same signal in presence of additive a clutter and additive noise at a *signal-to-noise ratio* (SNR) of 10 dB and *signal-to-clutter ratio* (SCR) of 10 dB. As can be observed, even though the clutter and noise are completely stationary, they presence also alters the definition of the 15 Hz signature on the CSD plane. Finally, Fig. 1.3 (f) presents the CSD plane for the original 15 Hz vibration with an extra chirp parameter of 1 Hz/s. In this case, the CSD losses definition as a result of the chirped vibration.

This detection method based on signatures of the CSD plane has three important drawbacks. First, the method requires a template of the CSD plane for each vibration under study and, therefore, it does not scale conveniently for detecting families of

vibrations such as simple sinusoidal waves, sinusoidal waves of multiple frequency components, or chirped waves. Second, the quality of the vibration signatures on the CSD is affected by the stationary noise and clutter which is not exclusively mapped to the region $\alpha = 0$. Third, for complex types of vibrations, such as chirp vibrations, the CSD plane loses definition and becomes ambiguous.

1.4 Contributions

This dissertation focuses on developing novel detection schemes for the detection and M-ary classification of vibrating objects in SAR images. Specifically, the work performed in this dissertation is conducted around following three central claims. First, the non-linear transformation that the micro-Doppler return of a vibrating object suffers through SAR sensing does not destroy its information. Second, the *instantaneous frequency* (IF) of the SAR signal has sufficient information to characterize vibrating objects. Third, it is possible to develop a detection model that encompasses multiple scenarios including both mono-component and multi-component vibrating objects immersed in noise and clutter.

In order to cement these claims, two different schemes are developed for both the detection and M-ary classification of vibrating objects in SAR images. The first scheme is data-driven and utilizes features extracted with the help of the *discrete fractional Fourier transform* (DFRFT) to feed *machine-learning algorithms* (MLAs). Specifically, the DFRFT is applied to the IF of the slow-time SAR data, which is reconstructed using enhanced spectrograms based on the *smoothed pseudo Wigner–Ville time-frequency distribution* (SPWVTFD) and the DFRFT. The MLAs studied in this work are: a linear *support-vector machine* (SVM), a 3-layer fully-connected *neural network* (NN), and a *random-forest classifier* (RFC). The details of this vibration detection and classification approach are provided in Chapter 3.1

Chapter 1. Introduction

and 4.1. The second scheme is model-based and employs a probabilistic model of the SAR slow-time signal, the *Karhunen-Loève transform* (KLT), and a likelihood-based decision function. Particularly, the KLT is used to decorrelate the samples of the SAR slow-time signal via *singular-value decomposition* (SVD). The details of the probabilistic detection scheme are provided in Chapters 3.2 and 4.2. Figure 1.4 summarizes the proposed detection methodologies in a block diagrams. The performance of the two proposed detection schemes is characterized using simulated data as well as real SAR data collected with the Lynx SAR system. The results shows that the two proposed schemes can be used to achieve high-performance vibrating-object detectors and classifiers.

The suitability of SAR for sensing surface vibrations is demonstrated by showing that the separability of different classes of vibrating objects is preserved even after non-linear SAR processing. For this purpose, an empirical experiment has been performed using MLAs, a library of vibration data from real machines (instantaneous position data) and simulated SAR data. Specifically, the simulated SAR data was generated using the machine-vibration data as input for the micro-Doppler return of a vibrating object (point-object). The classification results of a set of two MLAs, one trained with the real vibration data and the other with the simulated SAR data, show that the separation of classes produced by the MLA trained with simulated SAR data is the same that the one provided by the MLA trained with the machine-vibration data. The details of this work are presented in Chapter 5.

Finally, the proposed algorithms are studied when the SAR slow-time signals are contaminated with noise and clutter. The results show that the proposed detection and classification schemes yields reliable results for SNRs and SCRs greater than -5 dB. To loosen these requirements, the *Hankel rank reduction* (HRR) technique, previously used for suppressing ocean clutter in ground-wave radar, is adapted to suppress clutter-noise in SAR images. The result shows that the proposed detection

schemes yields reliable results for SNRs and SCRs greater than -10 dB when the SAR images are pre-processed with the HRR method. This extends the capabilities of the proposed detection algorithms in presence of noise and clutter, and also corroborates the fitness of the HRR technique for performing noise and clutter suppression in SAR imaging.

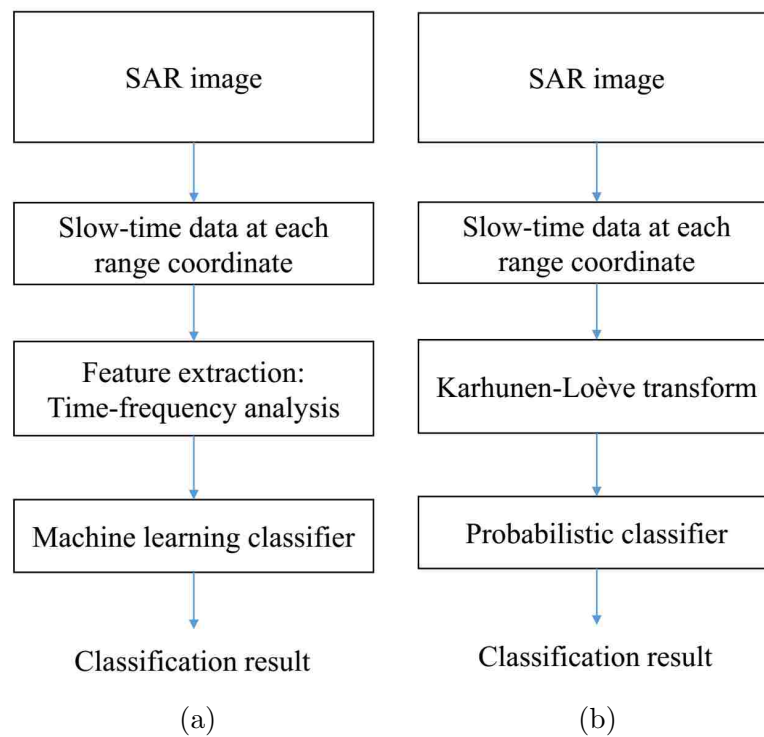


Figure 1.4: Block diagram of the proposed methodologies for the detection and classification of vibrating objects in SAR images. (a) Data-driven approach based on MLAs. (b) Approach based on a probabilistic model of the SAR slow-time signal.

Chapter 2

Theoretical background

2.1 Motion model

Figure 2.1 shows a three-dimensional SAR flight geometry for a vibrating target located at the origin. The nominal line-of-sight distance from the target to the radar sensor is r_0 , with the radar sensor located at polar angles ψ and θ to the target. Let $r_d(t)$ denote the projection of the vibration displacement onto the line-of-sight from the target to the SAR sensor, the range of the vibrating target becomes

$$r(t) \approx r_0 - r_d(t). \quad (2.1)$$

Due to the change of aspect angle of the target during the SAR data-collection process, the range r_0 also slightly changes. However, modern SAR compensates for the change via proper modeling and post signal-processing techniques [20–22]. The projection, $r_d(t)$, is also modulated by the change of aspect angle. For broadside SAR, the projection can be approximated by

$$r_d(t) \approx r_{d0} \cos \theta(t), \quad (2.2)$$

where r_{d0} represents the projection of the vibration displacement for $\theta = 0$. The change of aspect angle $\theta(t)$ due to the SAR geometry is known; therefore, $r_{d0}(t)$ can be estimated from $r_d(t)$. For spotlight-mode SAR, the change of aspect angle is usually small [20]. In this case $r_d(t) \approx r_{d0}(t)$.

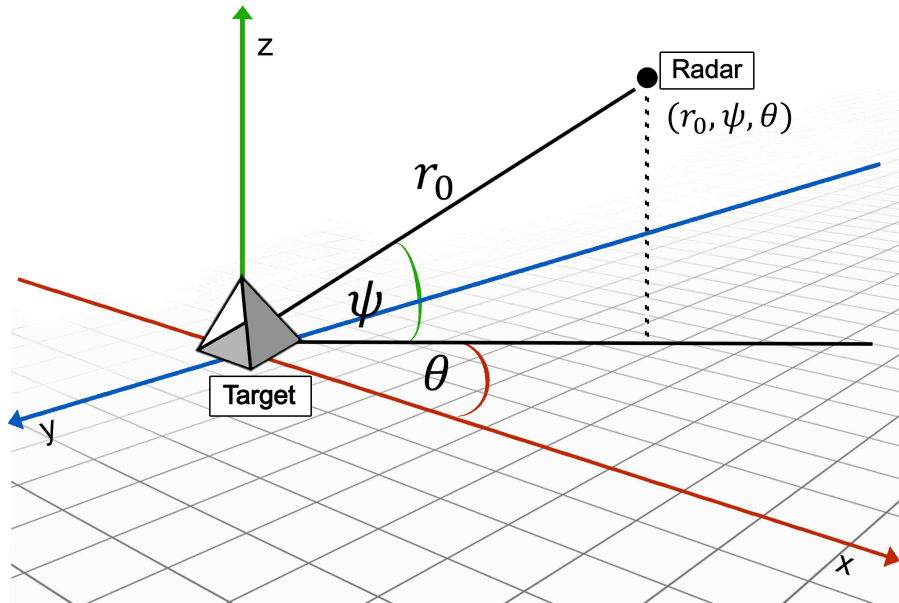


Figure 2.1: A three-dimensional SAR flight geometry. The vibrating target is located at the origin and the radar sensor is located at (r_0, ψ, θ) .

2.2 Signal model

The small range perturbation of the vibrating target modulates the collected SAR phase history. Consider a spotlight-mode SAR whose transmitted pulse is a chirp signal, with carrier frequency and chirp rate f_c and K , respectively. Each returned SAR pulse is demodulated by the transmitted pulse delayed appropriately by the round-trip time to the center of the illuminated patch. A demodulated pulse can be

Chapter 2. Theoretical background

written as [20, Ch. 1]

$$r(t) = \sum_i \sigma_i \exp \left[-j \frac{4\pi(r_i - r_c)}{c} \left(f_c + K \left(t - \frac{2r_c}{c} \right) \right) \right], \quad (2.3)$$

where σ_i is the reflectivity of the i th scatterer, c is the propagation speed of the pulse, and r_c is the distance from the patch center to the antenna. The polar-to-rectangular resampling approach is then applied to the SAR phase history [20, Sec. 3.5] to correct for range cell migration. The autofocus is also performed at this stage. For small vibrations, the vibration-induced phase modulation in range direction is very small [10, 23, 24]; therefore, it is ignored. Range compression is applied to the phase history to separate the scatterers in range. Figure 2.2 shows the magnitude of the range-compressed SAR phase history containing one static point target and one vibrating point target. Assuming that all scatterers at a specific range are static, the range-compressed phase history at this specific range can be written as

$$s[n] = \sum_i \sigma_i[n] \exp \left[j \left(f_y y_i n - \frac{4\pi f_c}{c} r_i + \phi_i \right) \right] + w[n], \quad (2.4)$$

for $0 \leq n < N - 1$, where n is the index of the collected returned pulses, N represents the total number of collected returned pulses, y_i is the cross-range position of the i th target, ϕ_i represents all additional (constant) phase terms and $w[n]$ is the signal noise. The imaging factor, f_y , is known and used to estimate the cross-range of the target. For spotlight-mode SAR, f_y can be written as [20, 21]

$$f_y = \frac{4\pi f_c}{c} \frac{V}{R_0 f_{prf}}, \quad (2.5)$$

where V is the nominal speed of the SAR antenna, R_0 is the distance from the patch center to the mid-aperture, and f_{prf} is the *pulse-repetition frequency* (PRF). The SAR integration time is given by $T_I = N/f_{prf}$.

The signal $s[n]$ in (2.4) is a stationary signal if all scatterers are static. The azimuth compression, accomplished by applying the *discrete Fourier transform* (DFT)

Chapter 2. Theoretical background

to $s[n]$, will focus the static scatterers on the correct cross-range positions. However, when a vibrating scatterer is present, $s[n]$ has a non-stationary component because r_i is now a function of n for the vibrating scatterer. The cross-range y_i is also changing for the vibrating scatterer. However, because R_0 is very large (tens of kilometers), f_y is usually much smaller than $4\pi f_c/c$; therefore, the phase modulation induced by time-varying y_i is ignored [10, 24]. As such, \bar{y}_i is used to denote the average cross-range position of the vibrating scatterer. For the same reason, a small change in r_i causes a relatively large fluctuation in the Doppler frequency $f_y y_i$. It is important to emphasize that azimuth compression cannot focus the vibrating scatterer on the correct cross-range position because the DFT spectrum of the non-stationary component usually has significant side lobes [25]. Figure 2.2 (b) shows the reconstructed SAR image by applying azimuth compression to the phase history as shown in Fig. 2.2 (a). The side lobes near the vibration target are commonly referred to as the *ghost targets* [25]. The vibration-induced phase modulation is referred to as the *micro-Doppler effect* [10]. Analysis tools other than the DFT are required to estimate and characterize vibrations and non-stationary targets in general.

The *signal of interest* (SoI) is defined as the slow-time signal (range line) in the range-compressed phase history containing vibrating targets. Figure 2.2 (a) shows the SoI of a static target and a vibrating target displayed in a range-compressed phase history image, and Fig. 2.3 shows the SoI of a static target and a vibrating target displayed as functions of the slow time.

When a vibrating scatterer is well-separated from other scatterers in range, which may be possible by choosing a proper data collection orientation, the SoI can be written as

$$s[n] = \sigma[n] \exp \left[j \left(f_y \bar{y}_i n - \frac{4\pi f_c}{c} r_d[n] + \phi \right) \right] + w[n] \quad (2.6)$$

for $0 \leq n < N - 1$. In this model, the signal contribution of all other scatterers have been collapsed into $w[n]$. Because of this, $w[n]$ is a clutter-noise signal.

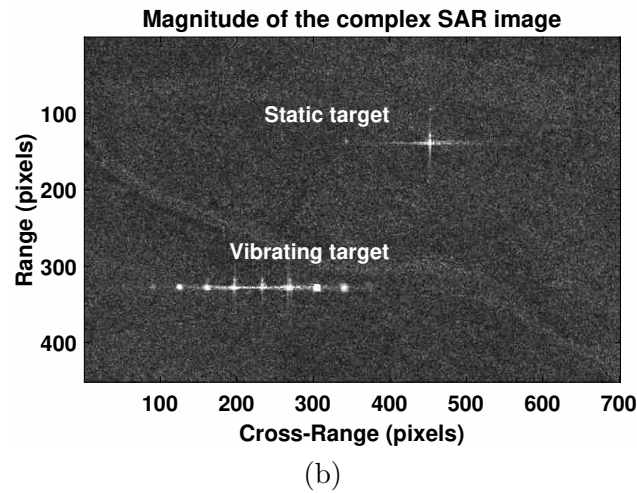
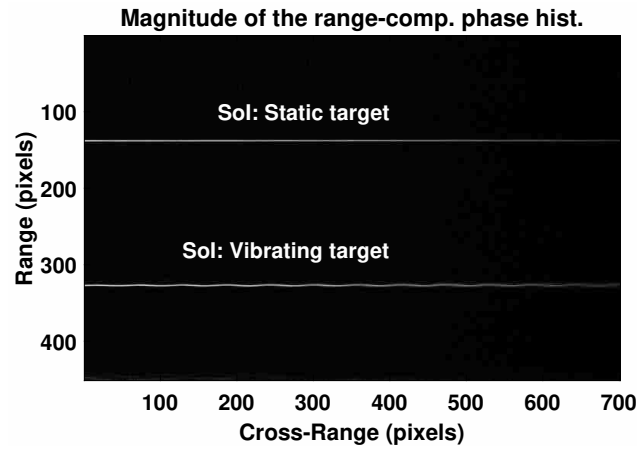


Figure 2.2: Reconstruction of a SAR image from its range-compressed phase history. (a) The magnitude of the range-compressed SAR phase history containing one static target and one vibrating target. The two targets are separated in range after range compression. (b) The reconstructed SAR image using the SAR phase history in (a). The vibrations of the target introduces ghost artifacts along the azimuth (cross-range) direction.

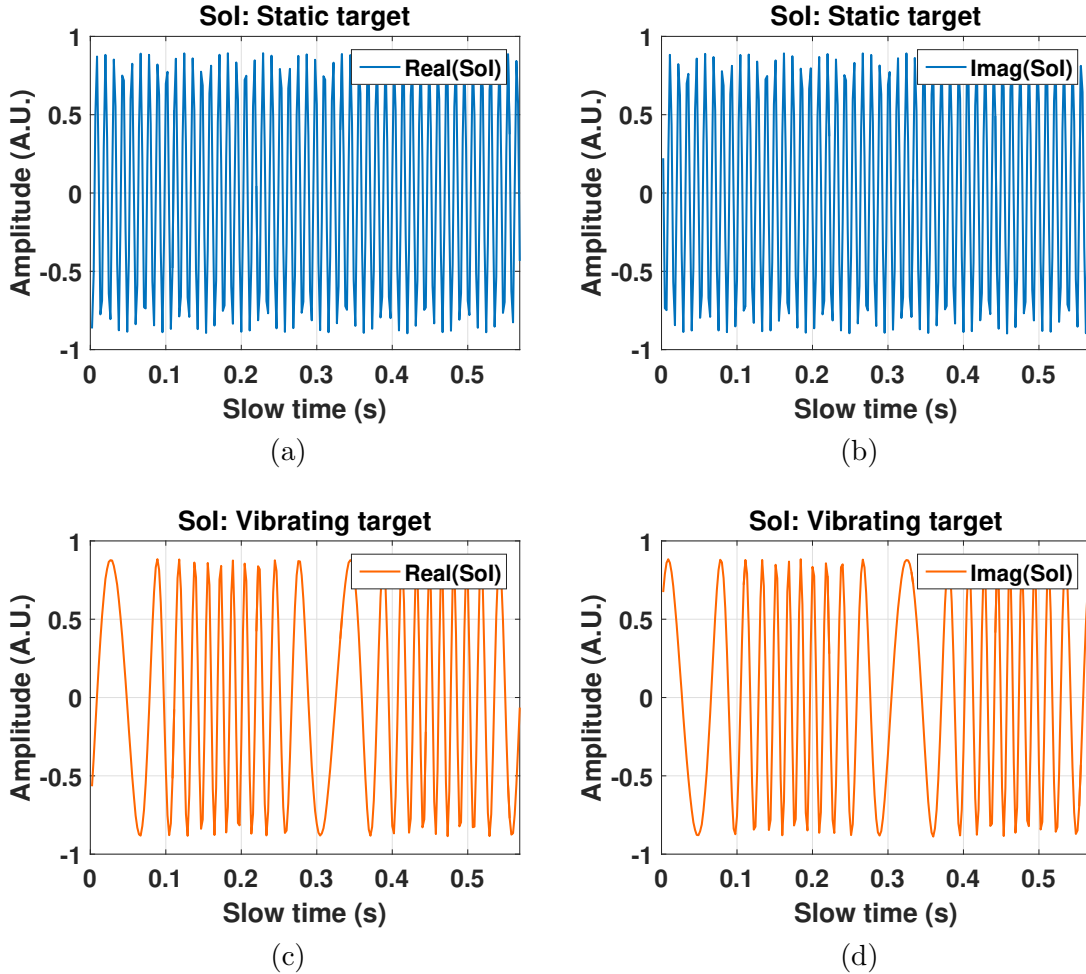


Figure 2.3: Example of the slow-time signal for a static and a vibrating targets. Complex Sol simulated for a (a,b) static target, (c,d) vibrating target. In (c,d) the target vibration induces phase modulation on the signal of (a,b). The vibration was assumed to be a sinusoidal function of amplitude 1cm and frequency 3.5Hz. The Lynx radar parameters of Table 2.1 and the signal model (2.6) were used for generating the signals.

All the simulations of SAR signals performed in this dissertation make use of 2.6 in conjunction with the Lynx radar parameters of Table 2.1.

Table 2.1: SAR system parameters for simulations. The parameters were extracted from SAR images generated with the Lynx radar operating at 1ft. resolution.

Parameter	Quantity
Pixel dimension	$0.25 \times 0.25 \text{ m}^2$
Nominal resolution	$0.3 \times 0.3 \text{ m}^2$
Carrier frequency	$f_c = 16.7 \text{ GHz}$
Slant range	$R_0 = 10 \text{ Km}$
Plane velocity	$V = 100 \text{ m/s}$
Effective pulse-repetition frequency	$f_{prf} = 450 \text{ Hz}$
Number of collected pulses	$N = 1024$
SNR	30 dB, unless otherwise specified
SCR	30 dB, unless otherwise specified

2.3 Binary hypothesis testing problem

In the signal model for the SAR SOI (2.6), the term $r_d[n]$ is the projection of the instantaneous position of the target onto the line of sight from the target to the SAR. Hence, when the target is static, the term $r_d[n]$ is a constant for all slow-time index n , but when the target is vibrating, $r_d[n]$ is the projection of the vibration displacement and, therefore, it varies over time. The only exception to this is when the vibration is unidirectional and it occurs parallel to the flight path of the sensor. This will cause the slow-time signal of the vibrating object to be identical as the slow-time signal of a static object. Nevertheless, this will not be considered as a concern because when imaging a site using an airborne SAR system, multiple passes from different azimuthal angles can be performed in order to ensure capturing micro-Doppler modulation of vibrating objects. Therefore, in consideration of the signal model (2.6) a binary hypothesis-testing problem is defined as follows. The null hypothesis, H_0 , represents the case in which the slow-time signal, $s[n]$, contains the return $s_0[n]$ from a static object; and the alternative hypothesis, H_1 , represents the case in which the slow-time signal, $s[n]$, contains the return $s_1[n]$ from a vibrating object. In this first formulation, it will be assumed that $r_d[n]$ corresponds to a pure

sinusoidal function. Also, without loss of generality, the constant phase terms in the signal model can be combined into a single one. Then, the hypotheses for a point object in a SAR image can be stated as follows:

$$\begin{aligned} H_0 : s[n] &= s_0[n] + w[n] = \sigma \exp(jf_y \bar{y}n + j\phi) + w[n], \\ H_1 : s[n] &= s_1[n] + w[n] = \sigma \exp(jf_y \bar{y}n + j\phi + jx[n]) + w[n], \end{aligned} \quad (2.7)$$

where $x[n] = \frac{4\pi f_c}{c} r_d[n]$ and it is been assumed that the reflectivity of the target σ does not change for $0 \leq n < N - 1$. Since in a SAR image the slow-time signal at a given range position consists of a total of N samples, the hypothesis-testing problem can be restated in the following vector form

$$H_0 : \mathbf{s} = [s[0], \dots, s[N - 1]]^T = \mathbf{s}_0 + \mathbf{w} = \begin{bmatrix} s_0[0] \\ \vdots \\ s_0[N - 1] \end{bmatrix} + \begin{bmatrix} w[0] \\ \vdots \\ w[N - 1] \end{bmatrix}, \quad (2.8)$$

vs.

$$H_1 : \mathbf{s} = [s[0], \dots, s[N - 1]]^T = \mathbf{s}_1 + \mathbf{w} = \begin{bmatrix} s_1[0] \\ \vdots \\ s_1[N - 1] \end{bmatrix} + \begin{bmatrix} w[0] \\ \vdots \\ w[N - 1] \end{bmatrix}.$$

Therefore, given a slow-time vector $\mathbf{s} = [s[0], \dots, s[N - 1]]^T$ from a SAR image, the ultimate goal is to determine if \mathbf{s} belongs either to H_0 or H_1 .

2.4 M-ary hypothesis testing problem

In the previous section, a probabilistic vibration detection model for addressing the binary hypothesis testing problem for a static object vs an object that exhibits a simple sinusoidal vibration has been mathematically developed. In this section, the probabilistic detection model is extended to a M-ary hypothesis testing problem for a point object in a SAR image. Specifically, the detection model is extended to

Chapter 2. Theoretical background

also consider $x[n]$ as multicomponent sinusoidal vibration and/or a multi-component chirped vibration for each one of the M hypotheses. This is

$$\begin{aligned} H_0 : s[n] &= s_0[n] + w[n] = \sigma \exp(jf_y \bar{y}n + j\phi + jx_0[n]) + w[n], \\ &\vdots \\ H_{M-1} : s[n] &= s_{M-1}[n] + w[n] = \sigma \exp(jf_y \bar{y}n + j\phi + jx_{M-1}[n]) + w[n], \end{aligned} \quad (2.9)$$

where $x_j[n]$ is a function defining the vibration pattern, i.e., mono-component sinusoid, multi-component sinusoid, mono-component chirp, multi-component chirp, or identically zero in for the case of a static object, $0 \leq j \leq M - 1$, $0 \leq n < N - 1$. Since in a SAR image the slow-time signal at a given range position consists of a total of N samples, the hypothesis-testing problem can be restated in the following vector form

$$\begin{aligned} H_0 : \mathbf{s} &= [s[0], \dots, s[N - 1]]^T = \mathbf{s}_0 + \mathbf{w} = \begin{bmatrix} s_0[0] \\ \vdots \\ s_0[N - 1] \end{bmatrix} + \begin{bmatrix} w[0] \\ \vdots \\ w[N - 1] \end{bmatrix}, \\ &\vdots \\ H_{M-1} : \mathbf{s} &= [s[0], \dots, s[N - 1]]^T = \mathbf{s}_{M-1} + \mathbf{w} = \begin{bmatrix} s_{M-1}[0] \\ \vdots \\ s_{M-1}[N - 1] \end{bmatrix} + \begin{bmatrix} w[0] \\ \vdots \\ w[N - 1] \end{bmatrix}. \end{aligned} \quad (2.10)$$

Therefore, given a slow-time vector $\mathbf{s} = [s[0], \dots, s[N - 1]]^T$ from a SAR image, the ultimate goal of the M-ary classification problem is to determine if \mathbf{s} belongs either to H_0 , H_1 , \dots , or H_{M-1} .

Chapter 3

Binary detection models

3.1 Vibration detection scheme based on machine-learning classifiers and the DFRFT

This detection scheme corresponds to a model-based data-driven approach for classifying vibration signatures in SAR images. Model-based data-driven approaches are appealing because they use data generated via simulation to train machine learning algorithms (detectors/classifiers), supplying in this way the need of thousands of samples that the training of these type classifiers normally require. For this purpose, SAR data is simulated combining the signal model for the SAR slow-time history (2.6) with different vibration waveforms. The simulated data goes through the feature extraction process described in Sec. 3.1.1. The feature data is labeled (static object, vibrating object) and compiled into datasets for training, validating and testing the MLA under study.

3.1.1 Feature extraction

The proposed feature extraction process makes use of an enhanced spectrogram and the DFRFT. The DFRFT, or more specifically the *multi-angle centered-discrete fractional Fourier transform* (MA-CDFRFT) [26], is a parametric extension of the centered DFT that describes the magnitude and phase of signals consisting in sinusoids of given frequency and chirp-rate. For a given a vector $\mathbf{s} = [s[0], \dots, s[N - 1]]^T$ consisting of N samples of the slow-time signal at given range coordinate of the SAR image, first, the SPWVTFD or a DFRFT-based fractional-spectrogram is applied to estimate the IF of the slow-time signal. On the one hand, the SPWVTFD is a bilinear time-frequency transform (time-dependent autocorrelation function) designed to reduce the cross-term interference¹ of the Wigner-Ville time-frequency distribution [10, 27]. On the other hand, a DFRFT-based spectrogram [28–30] is a linear time-frequency analysis technique that uses the DFRFT to produce sharper spectrograms for multicomponent chirp analysis. Unlike the SPWVTFD, since the DFRFT is a linear transformation, DFRFT-based spectrograms does not suffer from cross-term interference. A more detailed description of these techniques is given in Appendices B, C, D. Particularly, in App. E a qualitative study is performed, between the SPWVTFD and a piece-wise linear DFRFT-spectrogram, for reconstructing vibration-modulated IF signals from simulated SAR data. Similar to the common Fourier spectrogram, both the SPWVTFD and a DFRFT-based spectrogram does not yield a direct, quantitative interpretation of IF of the signal but instead it produces a graphical illustration of it, which must be further interpreted and analyzed if multiple frequencies or non-stationary frequencies are present in the vibration. Nevertheless, here it is assumed that the instantaneous position of vibration can be recovered from the SPWVTFD or a DFRFT-based spectrogram of the SAR slow-time signal by comparing its magnitude with a threshold. Once an estimation of the

¹The Wigner-Ville time-frequency distribution of the sum of two signals is not the sum of their individual Wigner-Ville time-frequency distributions.

Chapter 3. Binary detection models

IF signal is obtained, then the DFRFT is applied to characterize the vibration in terms of number of components, center-frequency and chirp-rate of each component. Even though the traditional DFT is sufficient for characterizing simple sinusoidal vibrations, the use of the DFRFT has the advantage that this same approach can be used for more complex type of vibrations, such as chirped vibrations, without the need of changing the feature extraction process. Finally, the feature extraction process concludes by computing the kurtosis, energy, variance and histogram of the IF signal. Algorithm 1 summarizes the feature extraction process of this detection scheme and Fig. 3.1 illustrates the feature extraction process step by step.

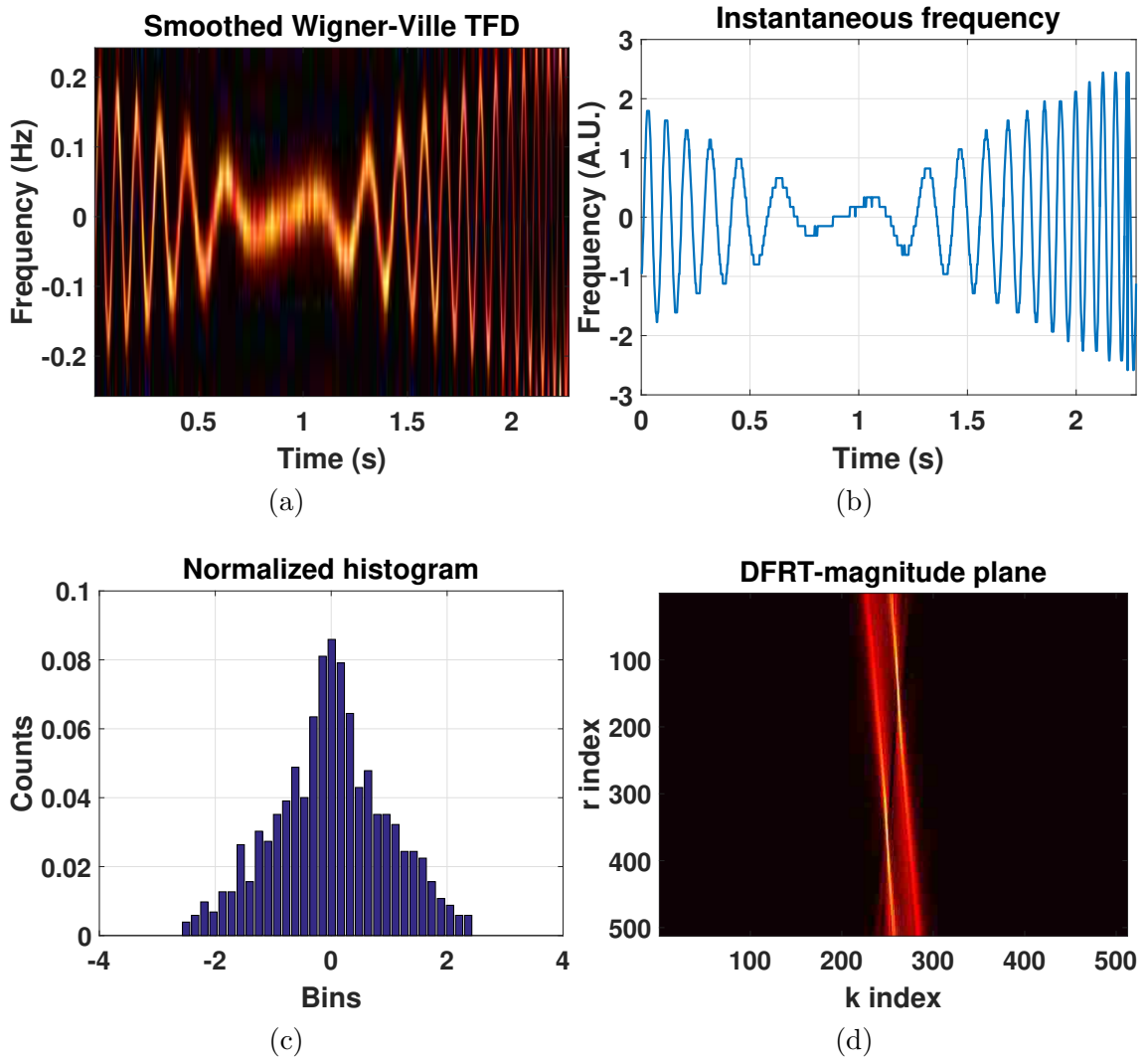


Figure 3.1: Feature extraction using the SPWVTFD and the DFRFT. (a) SPWVTFD of a SAR signal generated from a object exhibiting a chirp vibration. (b) IF recovered from (a) by thresholding. (c) Normalized histogram of (b) using 32 bins. (d) Magnitude plane of the 512-points DFRFT of (b).

Algorithm 1 Feature extraction using the DFRFT and time-frequency analysis tools.

- 1: $\mathbf{s} = [s[0], \dots, s[N - 1]]^T$: a slow-time vector from a SAR image.
 - 2: Apply the SPWVTFD, or the piece-wise linear DFRFT-based spectrogram, to \mathbf{s} to generate a N_b -frequency-bins spectrogram of the slow-time signal (e.g. $N_b=32$).
 - 3: The IF curve (vibration waveform) of the slow-time signal is then extracted from the previous spectrogram using thresholding.
 - 4: Compute the kurtosis, variance and energy on the extracted IF curve.
 - 5: Compute the N_b -bins histogram of the IF.
 - 6: Apply the DFRFT to the IF and store the information of the N_c -most prominent peaks of magnitude plane (e.g. $N_c=6$). Specifically, the magnitude of each peak, its center frequency and its chirp-rate value are considered.
 - 7: Finally, the features computed in 4), 5) and 6) are concatenated in a single feature vector of dimension $N = N_b + 3 + 3N_c$ (e.g. 53×1 , for $N_b=32$ and $N_c=6$).
-

3.1.2 Machine-learning classifiers

Three different types of data-driven machine-learning architectures are studied for sake of the analysis. The first classifier is a linear SVM [31] that divides the feature space using hyper-planes as boundaries. The second classifier is a 3-layer fully-connected NN [31]. Specifically, the classifier corresponds to a NN consisting of 2 hidden layers with rectified linear units as activation functions and a “logits” (output) layer that feeds a softmax function. A general scheme of the NN architecture is pictured in Fig. 3.2. The total number of neurons per layer is 53:30:10:2:1. The third classifier is a RFC [31] that averages the predictions of multiple decision trees on random subsets of the feature space. Both the NN and the RFC produce non-linear division of the feature space. The linear SVM and the RFC are trained using a

3-fold procedure with stratification and no hyperparameter tuning. The training of the NN is carried out in 50 epochs using a data batch of size 50 and minimizing a softmax cross-entropy loss function. In order to reduce overfitting and to produce a more compact network, dropout hyperparameter tuning, at a rate of 50% is considered. The implementation of these three classifiers is carried out using TensorFlowTM [32].

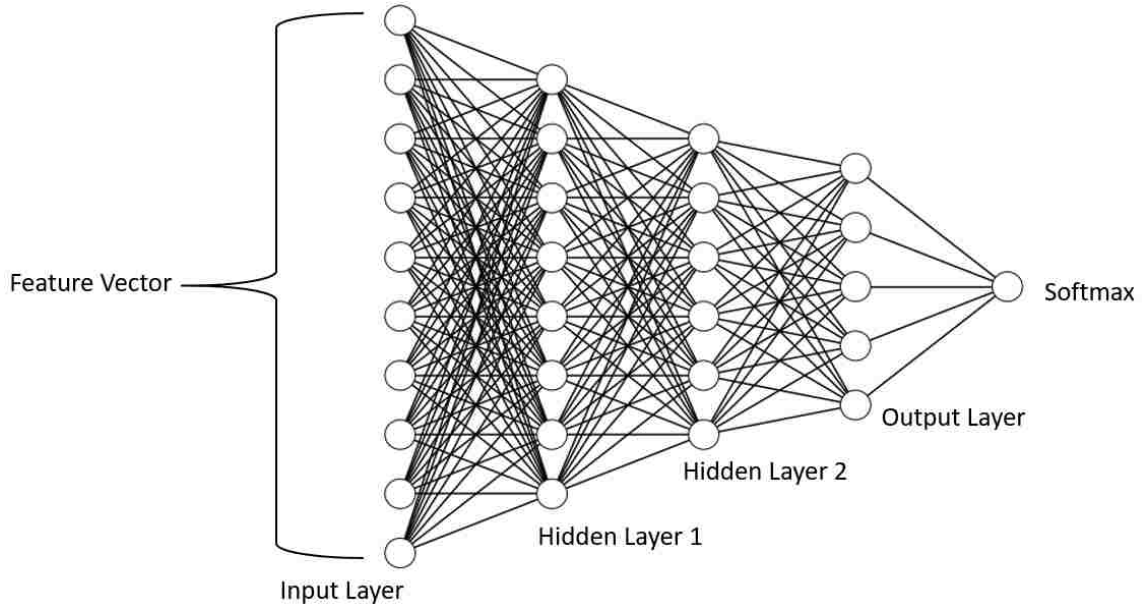


Figure 3.2: General scheme of the proposed neural network for classification of vibrating objects in SAR images.

3.2 Vibration detection based on a probabilistic model of the SAR slow-time signal

This detection approach is model-based and uses a probabilistic representation of the SAR signal under each hypothesis. The detection algorithm is based on a likelihood ratio function of the SAR slow-time signal. The *Karhunen-Loève* (KL) expansion is introduced to pre-process the slow-time signals due to the inconveniences that arise

when working with the joint *probability density functions* (PDFs) of the SAR signal. Specifically, the KL expansion is used to transform the hypothesis testing problem to an equivalent one, where the samples of transformed signal are now statistically independent.

3.2.1 Probabilistic model of the binary hypothesis testing problem

Recall the hypothesis testing problem (2.7) and (2.8) for an N -samples slow-time vector, where $s_0[n]$ is the part of the slow-time signal that corresponds to the return of a static object, $s_1[n]$ is the part of the slow-time signal that corresponds to the return of a vibrating object, and $w[n]$ is an additive term to represent noise and clutter. Due to physical properties of a SAR, there are natural constraints for the variables σ , ϕ , \bar{y} for an object within a SAR image. Similarly, due the limitations of a sensing vibrations with SAR [17], some constraints also apply to the vibration waveform (instantaneous position) $x[n]$, $0 \leq n \leq N - 1$. In light of this limitations, consider the following probabilistic model of (2.7) for a vibration described by a simple sinusoidal function

$$\begin{aligned} H_0 : S[n] &= S_0[n] + W[n] = \Sigma \exp(jf_y Y n + j\Phi) + W[n], \\ H_1 : S[n] &= S_1[n] + W[n] = \Sigma \exp(jf_y Y n + j\Phi + jX[n]) + W[n], \end{aligned} \quad (3.1)$$

where $\Sigma \sim U[\sigma_{min}, \sigma_{max}]$ (the symbol “ \sim ” means “distributed as”) is the reflectivity of the object, $Y \sim U[-y_o, y_o]$ is its cross-range coordinate (deviation from the center of the SAR image) with $y_o > 0$, $\Phi \sim U[-\pi, \pi]$ is a constant (yet random) phase term, and $W[n] \sim \mathcal{CN}(0, \sigma_w^2)$ is circularly-symmetric complex Gaussian noise, $0 \leq n \leq N - 1$. The reasons supporting these assumption on $W[n]$ arise from a statistical analysis performed on SAR images, see for instance App. F. The term $X[n] = A \cos(\Phi_x + 2\pi n F)$ is the projection of the instantaneous position of the vibrating object onto the line of sight from the object to the SAR, where $\Phi_x \sim U[-\pi, \pi]$

Chapter 3. Binary detection models

is a vibration phase term, $F \sim U[f_{min}, f_{max}]$ is directly proportional to the vibration frequency, and $A \sim U[a_{min}, a_{max}]$ is directly proportional to the vibration amplitude. The scaling factor for the vibration frequency is $1/f_{prf}$, and for the vibration amplitude is $\frac{4\pi f_c}{c}$. It is important to recall that all the parameters that determine the distribution of these random variables can be estimated from the SAR specifications. In the vector form of the hypothesis testing problem (2.8), the random variables $S[0], S[1], \dots, S[N-1]$ are correlated under both hypotheses. However, the noise samples $W[0], W[1], \dots, W[N-1]$ are considered to be independent and identically distributed.

3.2.2 Direct detection approach

This detection approach is based on the likelihood ratio between the PDFs of the SAR signal under the two hypothesis. In order to compute the joint PDF of the random slow-time vector $\mathbf{S} = [S[0], S[1], \dots, S[N-1]]^T$ under both hypotheses, i.e., $f_{\mathbf{S}}|_{H_0}$ and $f_{\mathbf{S}}|_{H_1}$, one can employ the fact that the noise samples are independent and, therefore, the PDF of \mathbf{S} for a given realization of the remaining random variables is the collective product of the noise PDFs. This is

$$\begin{aligned} f_{\mathbf{S}|\Sigma, \Phi, Y}(\mathbf{s}|\sigma, \phi, y)|_{H_0} &= \\ &= \prod_{n=0}^{N-1} \left(\frac{1}{\pi\sigma_w^2} \right) \exp \left(- \frac{|s[n]-s_0[n]|^2}{\sigma_w^2} \right) \\ &= \prod_{n=0}^{N-1} \left(\frac{1}{\pi\sigma_w^2} \right) \exp \left(- \frac{|s[n]-\sigma \exp(jf_y y n + j\phi)|^2}{\sigma_w^2} \right), \end{aligned} \quad (3.2)$$

$$\begin{aligned} f_{\mathbf{S}|\Sigma, \Phi, Y, A, F, \Phi_x}(\mathbf{s}|\sigma, \phi, y, a, f, \phi_x)|_{H_1} &= \\ &= \prod_{n=0}^{N-1} \left(\frac{1}{\pi\sigma_w^2} \right) \exp \left(- \frac{|s[n]-s_1[n]|^2}{\sigma_w^2} \right) \\ &= \prod_{n=0}^{N-1} \left(\frac{1}{\pi\sigma_w^2} \right) \exp \left(- \frac{|s[n]-\sigma \exp(jf_y y n + j\phi + ja \cos(\phi_x + 2\pi n f))|^2}{\sigma_w^2} \right). \end{aligned} \quad (3.3)$$

The next step on determining $f_{\mathbf{S}}|_{H_0}$ and $f_{\mathbf{S}}|_{H_1}$ consists on integrating the expressions above using the marginal probability distributions of the random variables that the

define the vibration signature under each hypothesis. This is performed in App. G. Finally, in consideration of (G.11) and (G.20), it is possible to define a binary detector for the hypothesis testing problem (2.8) based on the likelihood ratio of these probability density functions as

$$L(\mathbf{s}) = \frac{f_{\mathbf{s}}(\mathbf{s})|_{H_1}}{f_{\mathbf{s}}(\mathbf{s})|_{H_0}} = \frac{R_1(\mathbf{s})}{L_0(\mathbf{s})}. \quad (3.4)$$

The likelihood ratio detector (3.4) produces an optimal detector for the hypothesis testing problem (2.8), [33]. However, its implementation is unappealing because of the elevated number of iterated numerical integrations that are required to evaluate $L(\mathbf{s})$ for a given slow-time vector \mathbf{s} . Particularly, this approach requires of 2 numerical integrations for computing $f_{\mathbf{s}}(\mathbf{s})|_{H_0}$ and 5 for computing $f_{\mathbf{s}}(\mathbf{s})|_{H_1}$. Even though the number of numerical integrations can be slightly reduced by collapsing the terms of the form $(\Phi + f_y Y n)$ and $(\Phi_x + 2\pi n F)$ into a single random variable using a trapezoidal distribution, the complexity of the algorithm still remains high. This is mainly due to the fact that the random samples $S[0], S[1], \dots, S[N - 1]$ of the slow-time signal are correlated. In order to overcome this issue and reduce the complexity of the proposed detection algorithm, in the next section an equivalent detector is developed using the KLT, which is capable of removing the temporal correlation of $S[0], S[1], \dots, S[N - 1]$ by diagonalizing the auto-covariance matrix of the random slow-time vector \mathbf{S} .

3.2.3 Detection approach using the KL expansion

The KL expansion allows one to decorrelate the components of the slow-time vector \mathbf{S} and, at the same time, it permits one to work with simpler probability density functions. Specifically, in the KL expansion the eigenvectors of the covariance matrix of the signal capture the temporal correlation of the signal. The randomness of \mathbf{S} is captured in the KL coefficients which correspond to the projections of \mathbf{S} onto the

Chapter 3. Binary detection models

set of eigenvectors of the covariance matrix.

Recall the hypothesis testing problem (3.1) defined in Sec. 3.2.1, where the reflectivity, phase and position of a point object are modeled as random variables as well as the amplitude, frequency and phase of the simple sinusoidal vibration $X[n] = A \cos(\Phi_x + 2\pi nF)$. In order to construct a detection scheme based on the KL expansion the first step is to compute the covariance matrices of the slow-time vector \mathbf{S} under both hypothesis, H_0 and H_1 . This is performed in App. H. Then, based on the previous KL expansion, App. I, it is possible to define a new likelihood ratio as a decision tool for detecting vibrating objects in SAR images. For this purpose, given a signal \mathbf{S} from a SAR image, a likelihood ratio function of using its KL coefficients is defined.

A slow-time signal $\mathbf{s} = [s[0], \dots, s[N-1]]^T$ can be expanded using the eigenvectors of the covariance matrix computed under each hypothesis. This is, given a slow-time vector \mathbf{s} from a SAR image, one can compute the KL coefficients under H_0 , $z_k^0 = (\mathbf{v}_k^0)^* \mathbf{s}$, and under H_1 , $z_k^1 = (\mathbf{v}_k^1)^* \mathbf{s}$, for $k = 0, 1, 2, \dots, N-1$. If \mathbf{S} is assumed to be complex-normal distributed, then resulting KL coefficients are also complex-normal distributed (and zero-mean, because \mathbf{S} is zero-mean) since they are a linear combination of complex-normal distributed random variables (I.3). Therefore, they can be completely described by their first- and second-order statistics. Furthermore, since $E\{Z_k^j Z_m^j\} = \mathbf{v}_k^{j*} E\{\mathbf{S}\mathbf{S}^T\} \mathbf{v}_m^{jT} = 0$ because $E\{\mathbf{S}\mathbf{S}^T\} = \mathbf{0}$ for H_j , $j = 0, 1$; the pseudo-covariance matrix of \mathbf{Z} is $\mathbf{0}_{N \times N}$ under H_0 and H_1 . Since the KL coefficients are independent, then

$$Z_k^0 \sim \mathcal{CN}(0, \lambda_k^0), \quad \text{and} \quad Z_k^1 \sim \mathcal{CN}(0, \lambda_k^1), \quad (3.5)$$

where λ_k^0 and λ_k^1 are the eigenvalues of $\mathbf{cov}\{\mathbf{S}\}$ under H_0 and H_1 , respectively. Therefore, an equivalent hypothesis testing problem to (3.1) can be stated as

$$\begin{aligned} H_1 : \mathbf{Z} &= \{Z_k\}_{k=0}^{N-1}, \quad Z_k \text{'s independent, with } Z_k \sim \mathcal{CN}(0, \lambda_k^1) \\ H_0 : \mathbf{Z} &= \{Z_k\}_{k=0}^{N-1}, \quad Z_k \text{'s independent, with } Z_k \sim \mathcal{CN}(0, \lambda_k^0). \end{aligned} \quad (3.6)$$

Algorithm 2 Vibration detection scheme using a probabilistic model and the KLT.

- 1: Determine the distributions of $\Sigma, Y, \Phi, A, f, \Phi_x$ based on radar specifications.
 - 2: Compute the covariance matrices under hypothesis H_0 and H_1 using (H.15) and (H.24), respectively.
 - 3: Perform the spectral decomposition of the two covariance matrices (I.1).
 - 4: For every slow-time vector $\mathbf{s} = [s[0], \dots, s[N-1]]^T$, compute $\{z_k^0\}_{k=0}^{N-1}$ and $\{z_k^1\}_{k=0}^{N-1}$ using (I.3) and the eigenvectors of $\mathbf{cov}(\mathbf{S})$ under H_0 and H_1 , respectively.
 - 5: Compute the likelihood ratio (3.8).
 - 6: Compare the likelihood ratio with a threshold to determine if \mathbf{s} belongs either to H_0 or H_1 .
-

Since the KL coefficients are independent, it is possible to define a likelihood ratio for a slow-time vector \mathbf{s} consisting of N samples, i.e., consisting of N KL coefficients under each hypothesis, as

$$L(\mathbf{s}) = \frac{f_{\mathbf{s}}(\mathbf{s})|_{H_1}}{f_{\mathbf{s}}(\mathbf{s})|_{H_0}} = \frac{f_{\mathbf{z}}(\mathbf{z})|_{H_1}}{f_{\mathbf{z}}(\mathbf{z})|_{H_0}} = \frac{\prod_{k=0}^{N-1} \frac{1}{\pi \lambda_k^1} \exp\left(-\frac{|z_k^1|^2}{\lambda_k^1}\right)}{\prod_{k=0}^{N-1} \frac{1}{\pi \lambda_k^0} \exp\left(-\frac{|z_k^0|^2}{\lambda_k^0}\right)}, \quad (3.7)$$

$$L(\mathbf{s}) = \prod_{k=0}^{N-1} \frac{\lambda_k^0}{\lambda_k^1} \exp\left(\frac{|z_k^0|^2}{\lambda_k^0} - \frac{|z_k^1|^2}{\lambda_k^1}\right). \quad (3.8)$$

The latter expression defines a likelihood ratio that can be compared with a threshold in order to decide if the slow-time signal \mathbf{s} , via its KL coefficients $\{z_k^0\}_{k=0}^{N-1}$ and $\{z_k^1\}_{k=0}^{N-1}$, corresponds to a signal generated by a vibrating object or a static object. Algorithm 2 summarizes the steps involved in this detection scheme.

3.3 Performance evaluation

In this section, the performance of the proposed detection schemes is evaluated. Specifically, the performance of the proposed algorithms is tested using both simulated and real SAR data. The purpose of this study is: (i) to understand the limits of the proposed detection schemes, (ii) to characterize their performance in terms of the *receiver operating characteristic* (ROC) curve, (iii) to study their robustness against a mixed dataset of real SAR data, which contains data from a collection of different vibrometry experiments, and (iv) to characterize its performance in the presence of noise and clutter at different intensity levels.

3.3.1 Dataset description

Two datasets are used to study the performance of the binary detectors. A simulated dataset, consisting of SAR images generated via simulation using the parameters of the Lynx Radar, see Table 2.1, is used to test the proposed detectors. Specifically, 80% of the dataset is used for training and validation of the MLAs. The remaining 20% is used to evaluate the performance of the all the proposed detectors. A second dataset, consisting of real SAR images collected with the Lynx Radar is also used to report the performance of the proposed detectors. The purpose of these two datasets is, one, to study how feasible it is to develop data-driven model-based detectors for the vibrating objects in SAR images and two, to test the performance of the proposed detectors using real SAR data. The details of each one of these two datasets is provided below.

Simulated dataset:

The vibrating objects were simulated using single-component sinusoidal vibrations with amplitude between 8 mm and 1.5 cm, and frequency between 2 Hz and 10 Hz.

Chapter 3. Binary detection models

For the two classes of objects, the simulated data was contaminated with additive noise and additive clutter at a SNR of 30 dB and a SCR of 30 dB. The noise was simulated as independent, circularly symmetric, complex Gaussian distributed samples. The clutter magnitude was generated by performing circular averaging filter on uniformly random distributed clutter matrix of the same dimensions of the radar synthetic aperture. The circular averaging filter employed a kernel of size of 3×3 pixels. The clutter phase was considered to be uniformly distributed between $-\pi$ and π . A total of 5,000 samples per class were generated. The division of samples within the dataset was 50% and 50% between static objects and vibrating objects. The objects were simulated assuming a deviation no greater than 15% from the center of the SAR image. Figure 3.3 shows an example of a pair of SAR images generated with these specifications.

Lynx dataset:

This dataset contains a total of 200 samples of SAR slow-time signals collected in previous vibrometry experiments. One hundred of this samples correspond to static objects and the remaining 100 samples correspond to vibrating objects. This dataset is heterogeneous in terms of resolution and contains SAR signatures collected with resolution of 1foot and 4in. Also, the plane velocity parameter varies from 80 m/s to 100 m/s and the pulse repetition frequency between 200 Hz - 500 Hz. The SNR of the samples of this dataset is 30 dB. Similarly, the SCR of the samples of this dataset is also 30 dB. The carrier frequency and R0, the distance to the center of the patch, are as in Table 2.1. Quad-corner reflectors were used as study objects (point-objects). The vibrations were induced by off-balanced motors and had frequency in the range 2 Hz - 6 Hz and amplitude between 2 mm and 5 cm. The position of the objects had a deviation less than 15% from the center of the SAR image. Figure 2.2 shows an example of a SAR image containing a static object and a vibrating object used in this dataset.

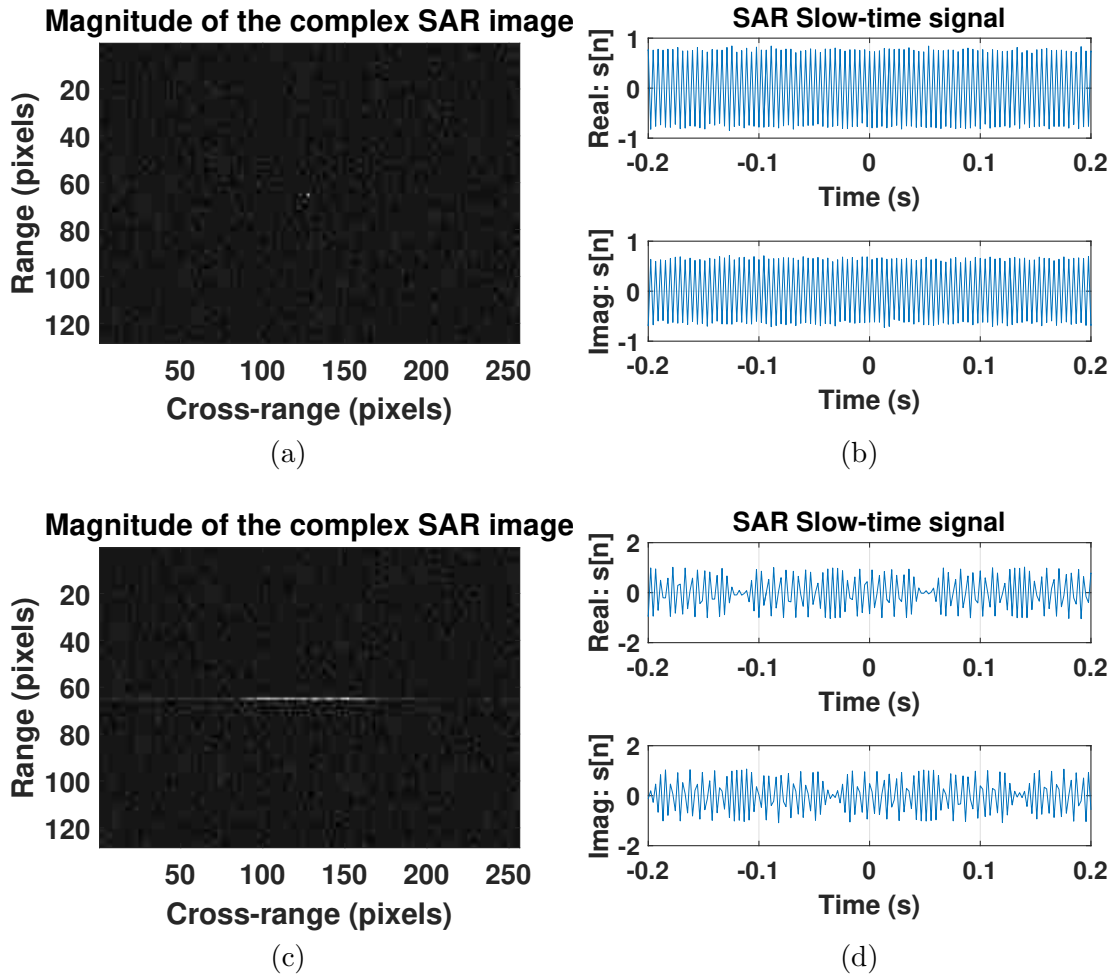


Figure 3.3: Examples of the 2 different types of SAR signatures simulated. SAR image and slow-time signal (range line 65 of the SAR image) of an (a,b) static point-object, (c,d) point-object with a single-component sinusoidal vibration. Note: for display purposes SAR images of size 128×256 pixels were generated.

3.3.2 Performance metrics

The performance of the proposed vibration-detection algorithms is mainly measured using the ROC curve and its convexity as indicators. Specifically, the ROC curve reports how well a detector performs in terms of detection ratio vs false-alarm ratio. The ROC curve, in the case of the MLAs, is computed by recording the performance while moving boundaries in the feature space and, in the case of the likelihood-ratio-based probabilistic detector, by increasing and decreasing the threshold. The convexity of the ROC curve is quantified by the *area under the ROC curve* (AUROCC). In addition, the feature usage in the construction of the random forest classifier is also analyzed for studying the suitability of the feature extraction process proposed in Sec. 3.1.

3.3.3 Demonstration and performance evaluation

The performance evaluation of the proposed detectors is presented in Figs. 3.4 and 3.5, and Table 3.1. First, as can be observed in Fig. 3.4 and Table 3.1, among the three machine-learning detectors implemented, the RFC is the one with the highest performance. Even though, the three MLAs perform similarly on the simulated dataset, on the Lynx dataset their performance drops about 0.2 to 0.3 in terms of the AUROCC. Also, similar to the case of the MLAs, the performance of the probabilistic detector also drops on the Lynx dataset. Specifically, the performance decreases about 0.076 points in terms of the AUROCC. These mismatches in performance may be attributed to several modeling errors including: (i) Imperfect radar cross-section modeling, since the objects contained in the Lynx dataset are quad-corner reflectors and not ideal point-objects; and (ii) variations of radar parameters across the Lynx dataset, since the Lynx dataset contains data from different vibrometry experiments collected at different PRF and resolution.

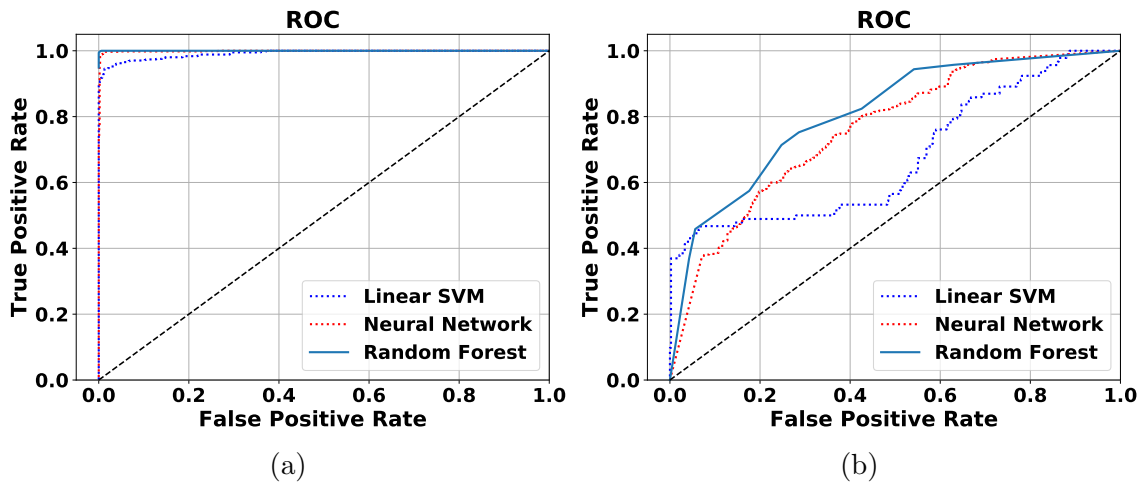


Figure 3.4: ROC of the MLAs for the binary detection problem. (a) Performance evaluation on the simulated dataset. (b) Performance evaluation on the Lynx dataset.

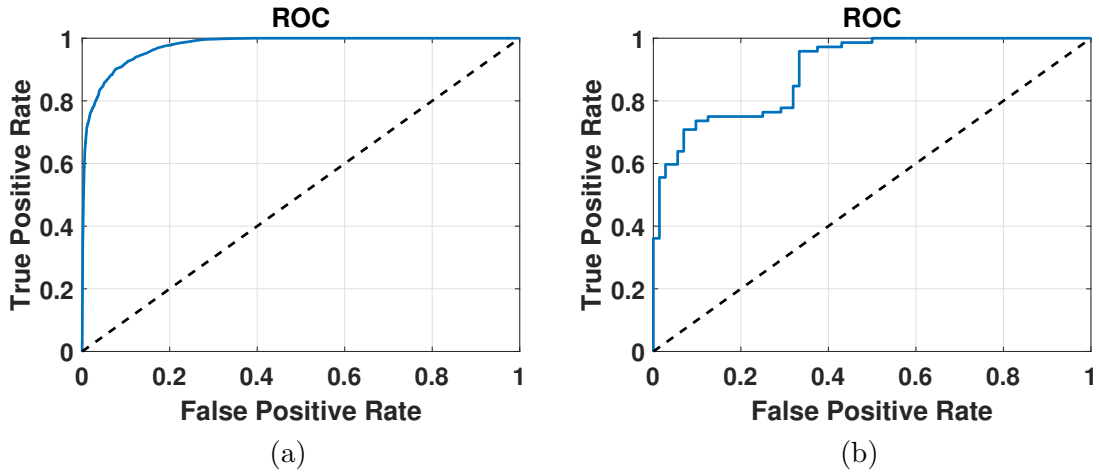


Figure 3.5: ROC curves of the probabilistic detector for the binary detection problem. (a) Performance evaluation on the simulated dataset. (b) Performance evaluation on the Lynx dataset.

Another interesting point is that the performance of the MLAs is slightly better than the performance the probabilistic detector on the simulated dataset. The reason behind this is the high SNR and SCR of this test. A completely different situation

Chapter 3. Binary detection models

Table 3.1: Area under the ROC curve of the proposed detectors for the binary detection problem.

Classifier	Simulated dataset	Lynx dataset
Linear SVM	0.991	0.676
Neural Network	0.999	0.761
RFC	1.000	0.808
Prob. detector	0.975	0.899

occurs in the performance evaluation of the proposed detectors on the Lynx dataset. In this case, the probabilistic detector overperforms the MLAs by 0.04-0.1pts in terms of the AUROC. This indicates that among all the tested detection algorithms, the probabilistic detector tend to be more robust against modeling errors in the data. For example, on the Lynx dataset for a false-alarm ratio of 10%, the linear SVM achieves a true positive rate of 45%, the NN 40%, the RFC 50%, and the probabilistic detector 75%.

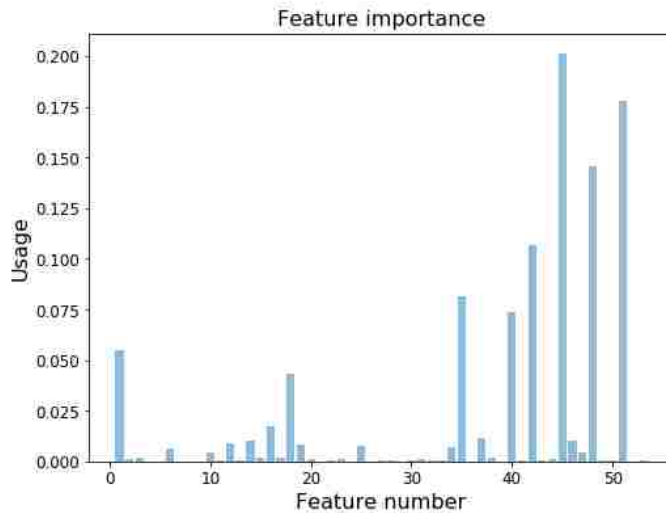


Figure 3.6: Feature usage of the constructed Random Forest classifier for the binary classification problem. The features #1-32 correspond to histogram values. The features #33-35 are statistics. The features #36-53 are the relative magnitude, frequency index and chirp rate index of the 6 highest peaks in the DFRFT plane

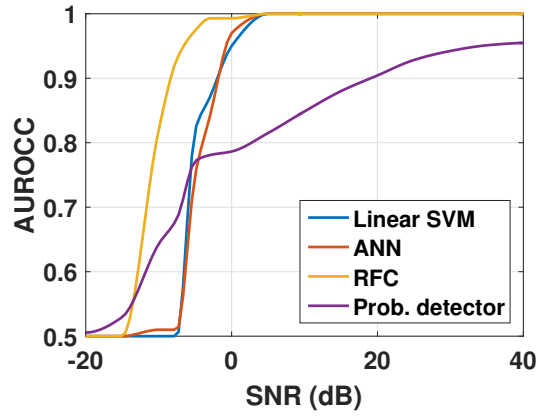
Finally, when analyzing the feature usage in the construction of the Random

Forest classifier, Fig. 3.6, it can be noted that the information contained in the peaks of the DFRFT plane are the most relevant features for classifying IF curves of slow-time history data (features #36-53). The central part of the histogram also contributes with useful features (features #10-20, the histogram range from feature #1 to #32) and, among the statistics contained in the feature vector, only the energy of the signal contributes with useful information (feature #35).

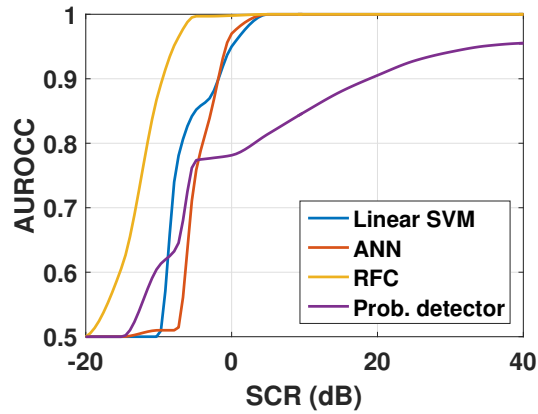
3.3.4 Characterization of performance in the presence of noise and clutter

In this section, the performance of the proposed detection algorithms is evaluated in the presence of noise and clutter at different intensity levels. This task is done using datasets of the same characteristics as the simulated dataset describe in Sec. 3.3.1 but with different values of SNR and SCR. Specifically, two experiments are performed. First, while keeping $SCR = \infty$, the performance of the proposed classifiers is measured in terms of the AUROC at different SNR values. Second, while keeping $SNR = \infty$, the performance of the proposed classifiers is measured in terms of the AUROC at different SCR values. The results are shown in Fig. 3.7.

As can be observed in Fig. 3.7, the RFC is the detector that exhibits the highest performance over all the tested SNR and SCR values. Particularly, in the range of -20 dB to -10 dB, the probabilistic detector overperforms the remaining MLAs, which have a drastic drop in performance. In contrast, the performance of the probabilistic detector drops at a lower rate as the SNR and SCR decreases. Finally, one can observe that the proposed detection algorithms have similar performance curves for clutter contamination and noise contamination.



(a)



(b)

Figure 3.7: Performance characterization of the proposed detector in terms of the AUROCC at various noise and clutter intensity levels. (a) Performance vs. noise. (b) Performance vs. clutter.

Chapter 4

M-ary detection models

4.1 Vibration classification scheme based on machine-learning classifiers and the DFRFT

The vibration detection scheme proposed in Sec. 3.1 is based on a feature extraction process utilizing the DFRFT. Such feature extraction procedure enables one to characterize not only simple sinusoidal vibrations but also more complex types of vibrations such as multi-component sinusoidal functions and multi-component chirp functions. Therefore, the detection procedures described in Sec. 3.1 can be directly applied to address the m-ary detection problem. The only modification that is required to address the M-hypothesis case is that the training dataset, now containing features from SAR signatures of M different types of vibration modes, has to contain the labels of each one of the new M hypotheses for the training of the MLAs.

4.2 Maximum-likelihood *M*-ary detector based on a probabilistic model of the SAR signal and the Karhunen-Loève expansion

In the previous chapter, a probabilistic vibration detection model for addressing the binary hypothesis testing problem for a static object vs an object that exhibits a simple sinusoidal vibration has been mathematically developed. In this section, the probabilistic detection model is extended to a *M*-ary hypothesis testing problem for a point object in a SAR image. Specifically, the detection model is extended to consider multicomponent sinusoidal vibrations and chirped vibrations. Also, the decision function becomes a maximum-likelihood operation as a natural extension of the previously described likelihood-ratio detector.

4.2.1 Probabilistic model of the *M*-ary hypothesis testing problem

For an illustrative purpose consider the following five hypotheses. Let the hypothesis H_0 represent the case in which the SAR slow-time signal $S_0[n]$ is generated from a static object. Let the hypothesis H_1 represent the case for which the slow-time signal $S_1[n]$ is generated from an object exhibiting a simple sinusoidal vibration. Let the hypothesis H_2 represent the case for which the slow-time signal $S_2[n]$ is generated from an object exhibiting a multicomponent sinusoidal vibration with K components. Let the hypothesis H_3 represent the case for which the slow-time signal $S_3[n]$ is generated from an object exhibiting a chirped vibration. Finally, let H_4 represent the case for which the slow-time signal $S_4[n]$ is generated from an object exhibiting a multicomponent chirp-sinusoidal vibration, consisting of K_c chirps and K_s sinusoids. The hypotheses for a random slow-time signal $S[n]$ of a point object

Chapter 4. *M*-ary detection models

in a SAR image can be stated as in (4.1) where $\Sigma \sim U[\sigma_{min}, \sigma_{max}]$ is the reflectivity of the object, $Y \sim U[-y_o, y_o]$ is its cross-range coordinate (deviation from the center of the SAR image) with $y_o > 0$, $\Phi \sim U[-\pi, \pi]$ is a constant (yet random) phase term, and $W \sim \mathcal{CN}(0, \sigma_w^2)$ is circularly-symmetric complex Gaussian clutter-noise, $0 \leq n \leq N - 1$. The reasons supporting these assumptions on $W[n]$ arise from a statistical analysis performed on SAR images, see App. F.

$$\begin{aligned}
 H_0 : S[n] &= S_0[n] + W[n] = \\
 &\quad \Sigma \exp(jf_y Y n + j\Phi) + W[n], \\
 \\
 H_1 : S[n] &= S_1[n] + W[n] = \\
 &\quad \Sigma \exp(jf_y Y n + j\Phi + jA \cos(\Phi_x + 2\pi n F)) + W[n], \\
 \\
 H_2 : S[n] &= S_2[n] + W[n] = \\
 &\quad \Sigma \exp(jf_y Y n + j\Phi + j \sum_{k=1}^K A_k \cos(\Phi_x^k + 2\pi n F_k)) + W[n], \tag{4.1} \\
 \\
 H_3 : S[n] &= S_3[n] + W[n] = \\
 &\quad \Sigma \exp(jf_y Y n + j\Phi + jA \cos(\Phi_x + 2\pi n(F + C_r n))) + W[n], \\
 \\
 H_4 : S[n] &= S_4[n] + W[n] = \\
 &\quad \Sigma \exp(jf_y Y n + j\Phi + j \sum_{i=1}^I A_i \cos(\Phi_x^i + 2\pi n F_i) \\
 &\quad + j \sum_{l=1}^L A_l \cos(\Phi_x^l + 2\pi n(F_l + C_r^l n))) + W[n],
 \end{aligned}$$

The terms in **blue color** are the corresponding vibration induced-phase modulation under each hypothesis. They represent the projection of the instantaneous position of the vibrating object onto the line of sight from the object to the SAR. The random variables that determine these vibration waveforms are defined as indicated below.

Chapter 4. *M*-ary detection models

- Φ_x , Φ_x^i , Φ_x^k and Φ_x^l are $\sim U[-\pi, \pi]$ vibration phase terms, for $1 \leq i, k, l \leq I, K, L$, respectively.
- $F \sim [f_{min}, f_{max}]$, $F_i \sim [f_{i_{min}}, f_{i_{max}}]$, $F_k \sim [f_{k_{min}}, f_{k_{max}}]$ and $F_l \sim [f_{l_{min}}, f_{l_{max}}]$ are directly proportional to the vibration frequency (Hz), with scale factor $1/f_{prf}$, for $1 \leq i, k, l \leq I, K, L$, respectively.
- $A \sim [a_{min}, a_{max}]$, $A_i \sim [a_{i_{min}}, a_{i_{max}}]$, $A_k \sim [a_{k_{min}}, a_{k_{max}}]$ and $A_l \sim [a_{l_{min}}, a_{l_{max}}]$ are directly proportional to the vibration amplitude (m), with scale factor $4\pi f_c/c$, for $1 \leq i, k, l \leq I, K, L$, respectively.
- $C_r \sim [c_{r_{min}}, c_{r_{max}}]$ and $C_r^l \sim [c_{r_{min}}^l, c_{r_{max}}^l]$, are directly proportional to the vibration chirp-rate (Hz/s), with scale factor $(1/f_{prf})^2$, for $1 \leq l \leq L$.

It is important to recall that all the parameters that determine the distribution of these random variables can be estimated from the SAR specifications and the characteristics of the vibration under study. In this work, all the aforementioned random variables are assumed to be independent. In the case of a specific dependency between different components (harmonics) of a vibration pattern, then the proposed model is still valid by introducing the corresponding relations between the involved random variables.

Since in a SAR image the slow-time signal of a point object at a given range position consists of a total of N samples, the previous hypotheses can be expressed as

$$H_j : \mathbf{S} = [S[0], \dots, S[N-1]]^T = \mathbf{S}_j + \mathbf{W} = \begin{bmatrix} S_j[0] \\ \vdots \\ S_j[N-1] \end{bmatrix} + \begin{bmatrix} W[0] \\ \vdots \\ W[N-1] \end{bmatrix} \quad (4.2)$$

In this representation, the samples $S[0], S[1], \dots, S[N-1]$ are not uncorrelated under any hypothesis. However, the clutter-noise samples $W[0], W[1], \dots, W[N-1]$ are independent and identically distributed.

4.2.2 M-ary maximum-likelihood detector based on the KL expansion

Similar to the case of the probabilistic binary detector of Sec. 3.2, the covariance matrices under each one of the M hypotheses are required for performing the KL expansion. This is performed in detail in App. J. Then, based on the KL expansion described in App. I, a likelihood test can be defined as a decision tool for detecting different types of vibrating object in a SAR image. For this purpose, given a SAR image the KL coefficients of the signal under all M hypotheses are determined. Once this has been done, a likelihood function proportional to the probability density function of the KL coefficients under every hypothesis is evaluated. In other words, every probability density function is weighted by the prior probability of the SAR signal belonging to that particular class. Finally, the maximum is taken over the weighted likelihood functions of all hypothesis in order to determine the winner hypothesis. The details of this procedure are given below.

A random slow-time signal $\mathbf{S} = [S[0], \dots, S[N-1]]^T$ can be expanded using the eigenvectors of the covariance matrix computed under each hypothesis. In other words, given \mathbf{S} , the corresponding KL coefficients under H_j , $Z_k^j = (v_k^j)^* \mathbf{S}$ are determined, for $k = 0, 1, 2, \dots, N-1$, and $0 \leq j \leq M-1$ hypotheses. If \mathbf{S} is zero-mean and Gaussian (i.e., zero-mean complex-normal distributed), then resulting KL coefficients are also zero-mean and Gaussian since they are a linear combination of complex-normal distributed random variables (I.3). Therefore, they can be completely described by their first- and second-order statistics. This conclusion leads to

$$Z_k^j \sim \mathcal{CN}(0, \lambda_k^j), \quad k = 0, 1, 2, \dots, N-1, \quad \text{and } j = 0, 1, 2, \dots, M-1, \quad (4.3)$$

where λ_k^j are the eigenvalues of $\mathbf{cov}\{\mathbf{S}\}$ under H_j , $0 \leq j \leq M-1$, respectively. Since the KL coefficients are independent among them, it is possible to compute the value

of the probability density function for a given slow-time signal $\mathbf{s} = [s[0], \dots, s[N-1]]$, i.e., consisting of N KL coefficients under each hypothesis, as

$$p_j(\mathbf{s}) = p_j(\mathbf{z}) = p_j^N(\{z_k^j\}_{k=1}^N) = \prod_{k=1}^N \frac{1}{\pi \lambda_k^j} \exp\left(\frac{-|z_k^j|^2}{\lambda_k^j}\right), \quad 0 \leq j \leq M-1. \quad (4.4)$$

Then, the maximum likelihood *M*-ary detector for the slow-time vector \mathbf{s} can be succinct as

$$\arg \max_{0 \leq j \leq M-1} \pi_j p_j(\mathbf{s}) = \arg \max_{0 \leq j \leq M-1} \pi_j \prod_{k=0}^{N-1} \left(\frac{1}{\pi \lambda_k^j}\right) \exp\left(\frac{-|z_k^j|^2}{\lambda_k^j}\right), \quad (4.5)$$

where $0 \leq \pi_j \leq 1$ and $\sum_{j=0}^{M-1} \pi_j = 1$. If no prior information about the likelihood of the hypothesis is available, then the prior probabilities can be set to $\pi_j = 1/M$, $0 \leq j \leq M-1$, so each hypothesis is equally likely. For implementation purposes and in order to avoid scaling issues arising from the high-magnitude radar parameters (e.g., high-magnitude reflectivity parameters and large SCR or SNR), it is recommendable to group the terms of the form $1/\pi \lambda_k^j$ together with the respective prior probabilities π_j . This is possible since the eigenvalues of the covariance matrix of the SAR slow-time signal are fixed under each hypothesis. Then, the equation for the maximum-likelihood *M*-ary detector can be stated as

$$\arg \max_{0 \leq j \leq M-1} \pi_j p_j(\mathbf{s}) = \arg \max_{0 \leq j \leq M-1} \pi_j \prod_{k=0}^{N-1} \exp\left(\frac{-|z_k^j|^2}{\lambda_k^j}\right), \quad (4.6)$$

with $0 \leq \pi_j \leq 1$ and $\sum_{j=0}^{M-1} \pi_j = 1$.

4.2.3 Optimal data-driven approach for determining the prior probabilities

If one also considers a dataset of SAR signals that have been properly labeled under one of the M hypotheses (e.g., this is possible by generating a SAR dataset using the signal model described before), then it is possible to obtain an optimal solution

Algorithm 3 *M*-ary detection of vibrations using a probabilistic model of the SAR signal and the KLT.

- 1: Based on radar specifications, determine the distributions of the random variables involved ($\Sigma, Y, \Phi, A, f, \Phi_x$, etc).
 - 2: Compute the covariance matrices under each one of the M hypotheses H_j , $0 \leq j \leq M - 1$, using (J.15).
 - 3: For every slow-time vector $\mathbf{s} = [s[0], \dots, s[N - 1]]^T$, compute $\{z_k^j\}_{k=0}^{N-1}$ using (I.3) and the eigenvectors of $\mathbf{cov}(\mathbf{S})$ under H_j , for every j hypothesis, $0 \leq j \leq M - 1$.
 - 4: Initialize the priors π_j or determine their optimal values using (4.7), $0 \leq j \leq M - 1$.
 - 5: Finally, the class of \mathbf{s} is determined by (4.6).
-

for the priors π_j 's of the previously described maximum-likelihood *M*-ary detector. Consider a dataset $\{\mathbf{s}_k\}_{k=1}^{N_s}$ consisting of N_s samples of SAR slow-time vectors $\mathbf{s} = [s[0], \dots, s[N - 1]]$. Then the set of priors $\{\pi_j\}_{j=0}^{M-1}$ can be determined as the ones that minimizes the classification error over the dataset. This is

$$[\pi_0^*, \dots, \pi_{M-1}^*] = \arg \min_{\pi_j} \sum_{k=0}^{N_s-1} p_d(\arg \max_{0 \leq j \leq M-1} \pi_j p_j(\mathbf{s}_k), C(\mathbf{s}_k)) \quad (4.7)$$

where $0 \leq \pi_j \leq 1$ and $\sum_{j=0}^{M-1} \pi_j = 1$, and \mathbf{s}_k is the k -th element of the dataset (\mathbf{s}_k is a vector of N samples) with class (label) $C(\mathbf{s}_k)$, $0 \leq C(\mathbf{s}_k) \leq M - 1$. The discrete metric p_d is zero if the label and the predicted class coincide and one otherwise, i.e.,

$$p_d(x, y) = \begin{cases} 0, & x = y \\ 1, & x \neq y \end{cases} \quad \forall x, y \in \mathbb{Z} \quad (4.8)$$

Finally, Alg. 3 summarizes all the steps involved in the implementation of the proposed *m*-ary detector, based on the probabilistic model of the SAR signal and the KLT, for vibrating objects in SAR images.

4.3 Performance Evaluation

In this section, the performance of the proposed *M*-ary detection schemes is evaluated. Specifically, the performance of the proposed algorithms was tested using simulated SAR data only. This is because at the time this experiment was conducted the author did not count with enough real SAR data to compute statistics for characterizing the performance of the proposed *M*-ary detectors. The purpose of this study is: (i) to understand the limits of the proposed detection schemes, (ii) to characterize their performance in terms of the overall classification accuracy, and (iii) to characterize its performance in the presence of noise and clutter at different intensity levels. Particularly, the capabilities of the proposed *M*-ary detectors are demonstrated using the following quaternary hypothesis testing problem.

- H_0 : Static object.
- H_1 : Vibrating object exhibiting a simple sinusoidal vibration pattern.
- H_2 : Vibrating object exhibiting a multicomponent sinusoidal vibration pattern.
- H_3 : Vibrating object exhibiting a simple chirped vibration pattern.

4.3.1 Specification of classes and dataset description

As indicated in the previous section, four different classes of SAR signatures are investigated. These classes are: (i) static objects (ST), (ii) objects exhibiting a single-component sinusoidal vibration (SC), (iii) objects exhibiting a multi-component sinusoidal vibration (MC), and (iv) objects exhibiting a chirp vibration (CR). The parameters defining the vibratory motion of samples of class (ii), (iii), and (iv) were chosen randomly while assuming uniform distributions. More specifically, the single-component vibration had amplitude defined between 8 mm and 1.5 cm, and frequency

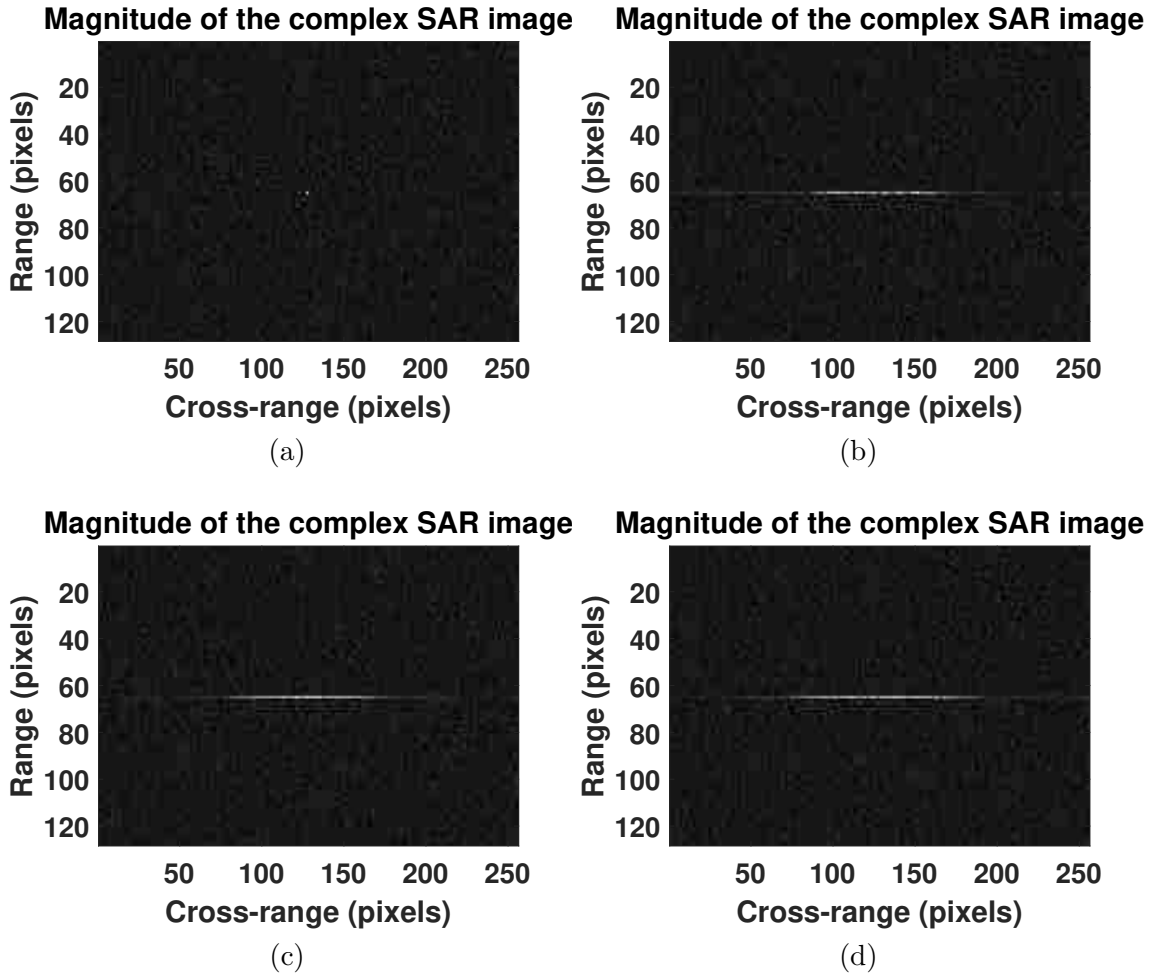


Figure 4.1: Examples of the 4 different types of SAR signatures simulated. SAR image of an (a) static point-object, (b) point-object with a single-component sinusoidal vibration, (c) point-object with a multi-component sinusoidal vibration and (d) point-object with a chirp vibration. Note: for display purposes SAR images of size 128×256 pixels were generated.

between 2 Hz and 10 Hz. The multi-component vibrations were formed by 3 sinusoids with amplitudes between 5 mm and 1 cm, and frequencies in the ranges 2 Hz - 5 Hz, 7 Hz - 10 Hz, 12 Hz - 15 Hz. The chirped vibrations had amplitude defined between 8 mm and 1.5 cm, center frequency between 2 Hz and 10 Hz, and a linear chirp-rate in the range ± 5 Hz/s to ± 10 Hz/s. The simulated data was contaminated

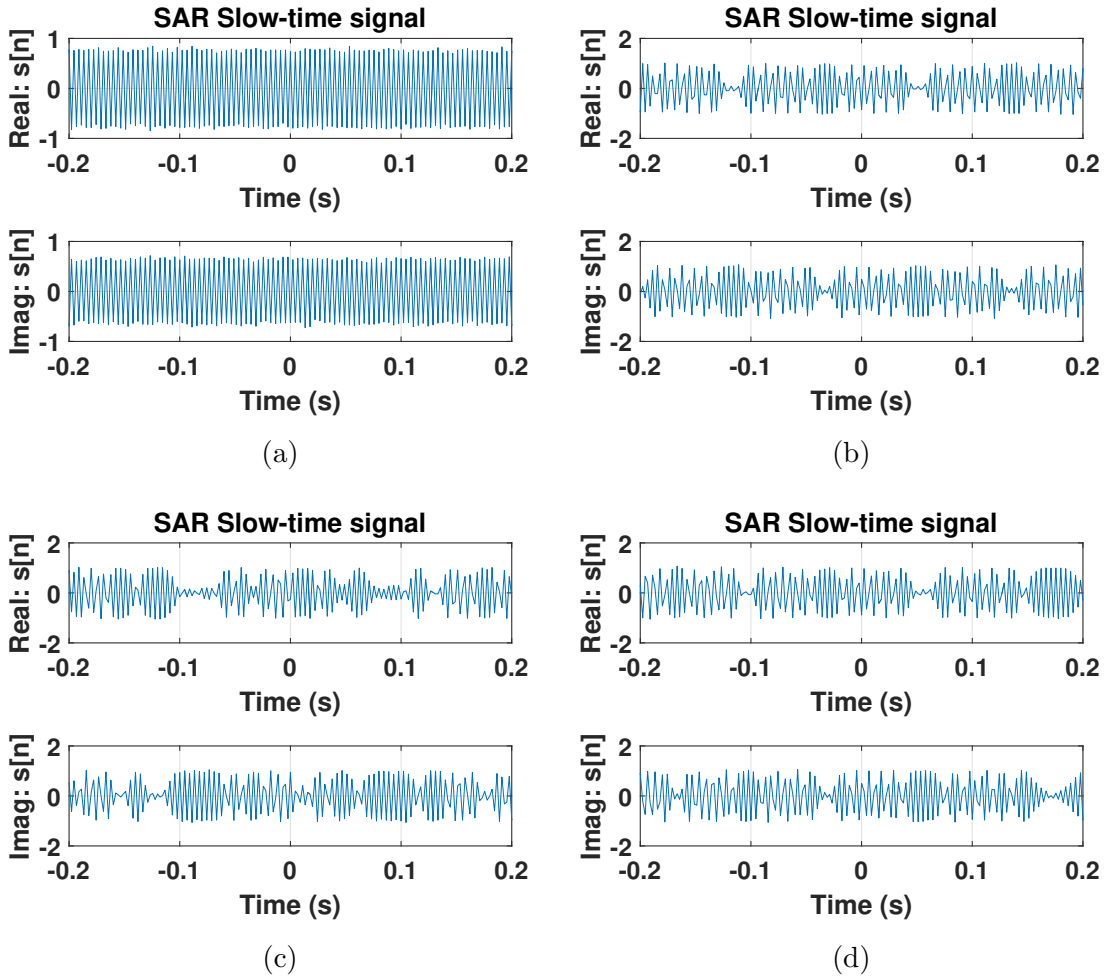


Figure 4.2: Signal of interest of the 4 different types of SAR signatures simulated. Range line 65 of the SAR images of Fig. 4.1 for a (a) static point-object, (b) point-object with a single-component sinusoidal vibration, (c) point-object with a multi-component sinusoidal vibration and (d) point-object with a chirp vibration.

with additive noise at a SNR of 30 dB, and additive clutter at SCR of 30 dB. The noise is simulated as independent circularly symmetric complex Gaussian distributed samples. The clutter magnitude is generated by performing circular averaging filter on uniformly random distributed clutter matrix of the same dimensions of the radar synthetic aperture. The circular averaging filter utilizes a kernel of size of 3×3 pixels.

The clutter phase is uniformly distributed between $-\pi$ and π . In order to generate realistic SAR data, the following parameters were used to emulate the collection process of the Lynx radar in spotlight mode. Figures 4.1 and 4.2 show samples of simulated SAR images for these four different types of objects. As can be observed, especially in the presence of vibrations, it is not easy to distinguish between the different types of signals in the slow-time domain nor in the frequency domain (SAR image).

Two datasets, each one containing of 10,000 slow-time vectors were generated via simulations. Each dataset contained 2,500 samples of each class. One data set is used for testing the final performance of the proposed detection schemes. The other one is used a training dataset for the MLA and also for determining the optimal priors for the maximum-likelihood detector.

4.3.2 Performance metrics

The metric selected for characterizing the classification performance of the selected *m*-ary detectors is the *overall accuracy*, which measures the average accuracy of the detection rate of each class (i.e., average percentage of correct classified samples). This metric is computed from the diagonal of the confusion matrix of each classifier.

4.3.3 Demonstration and performance evaluation

Classification using MLAs:

The performance results of these classification algorithms is presented in Tab. 4.1 and Fig. 4.3. Among the classifiers implemented, it must be noted that the linear SVM classifier is the one with the lower performance. This is an indicator that the features are distributed in a non-linear fashion in the feature space. Nevertheless, for

Chapter 4. *M*-ary detection models

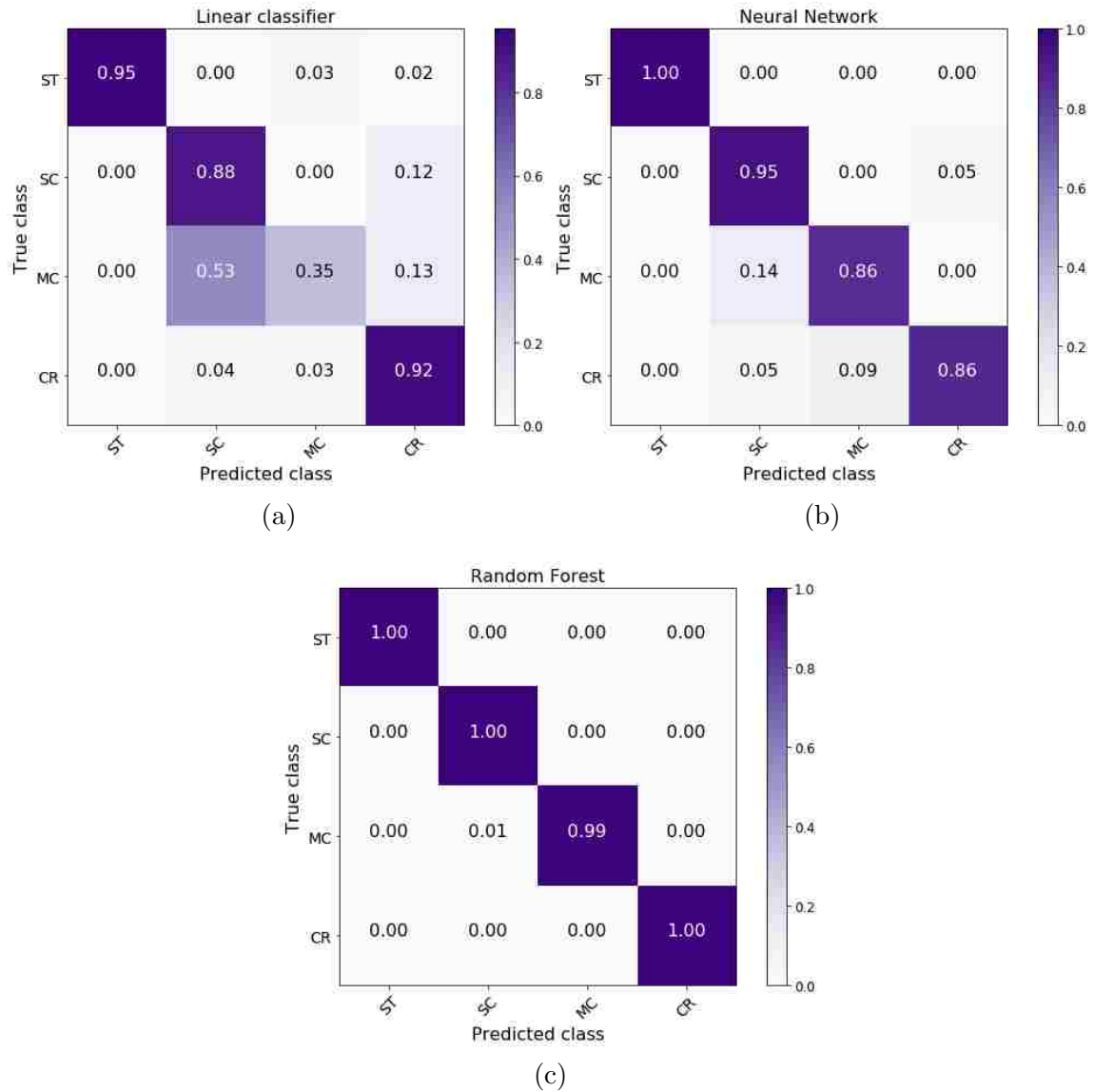


Figure 4.3: Confusion matrices of the MLAs for the quaternary classification problem. (a) Linear support-vector machine. (b) Artificial neural network. (c) Random Forest classifier.

this demonstrative test with high SNR and high SCR, the three MLAs are capable of separating the data based on the features extracted from the SAR signatures.

When analyzing the feature usage of the Random Forest Classifier, Fig. 4.4 , it can

Chapter 4. *M*-ary detection models

Table 4.1: Overall accuracy of the proposed *M*-ary classifiers for the quaternary classification problem.

Classifier	Accuracy
Linear SVM	77.5%
Neural Network	92.6%
RFC	99.8%
MLC	86.3%

be noted that not all the features contribute to the creation of decision boundaries. Specifically, not the whole histogram, but only its outer region is relevant as shown in the usage of features 1-32. Also, the figure shows that the statistics (features 32-35) and the 6 peaks extracted from the DFRFT plane (features 36-53) are all relevant for this classification problem.

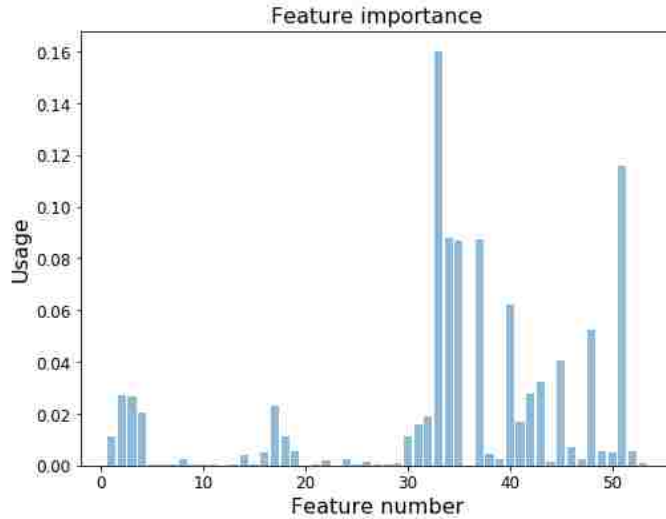


Figure 4.4: Feature usage of the constructed Random Forest classifier for the quaternary classification problem. The features #1-32 correspond to histogram values. The features #33-35 are statistics. The features #36-53 are the relative magnitude, frequency index and chirp rate index of the 6 highest peaks in the DFRFT plane

Classification using the maximum-likelihood classifier (MLC):

Three different cases are studied for the priors that weight the likelihood functions.

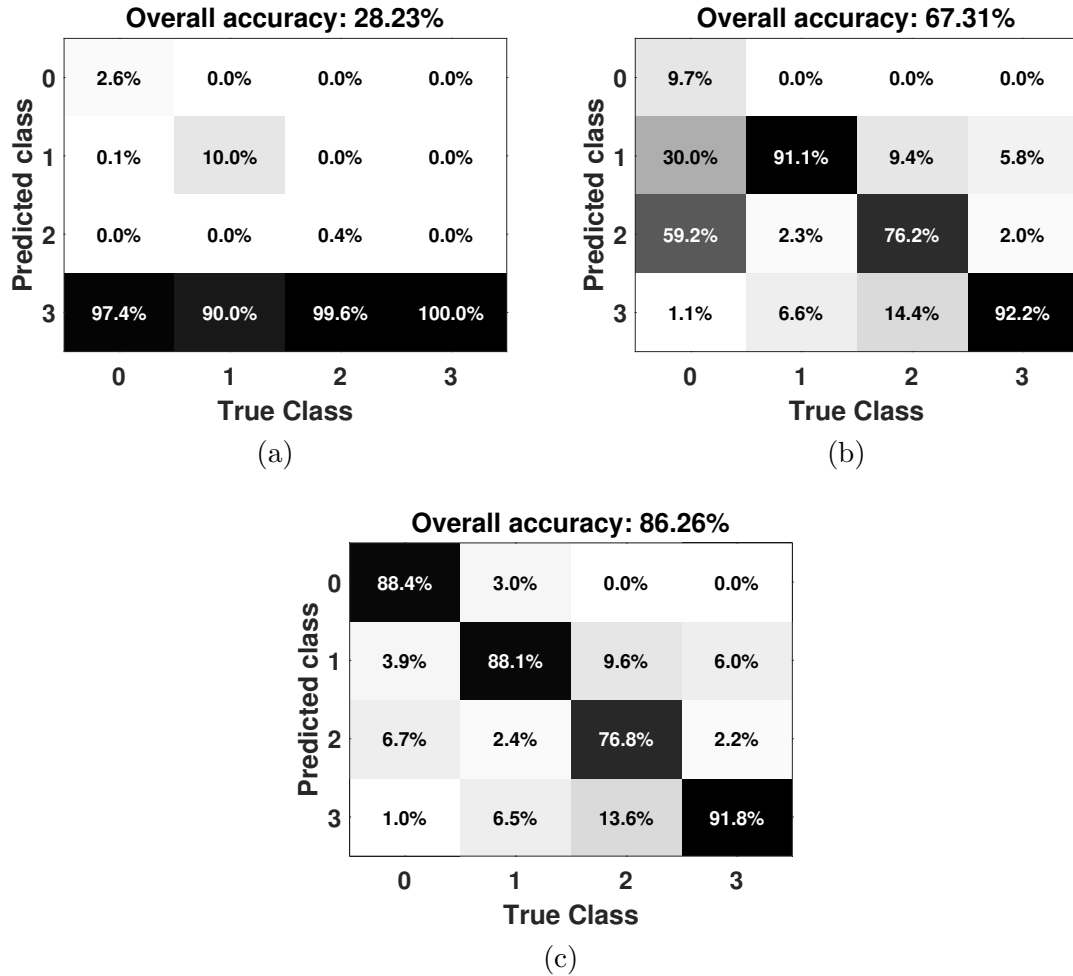


Figure 4.5: Confusion matrices of the maximum-likelihood *M*-ary classifier for the quaternary classification problem. (a) Case of equal priors. (b) Case of priors determined by trial-and-error. (c) Case of priors determined by the proposed optimal approach.

The first case assumes that all the hypothesis has been weighted equally by the priors, i.e., $\pi_1 = \pi_2 = \pi_3 = \pi_4 = 0.25$. For the second case, the weights are $\pi_1 = \pi_2 = \pi_3 = 0.3$ and $\pi_4 = 0.1$, and they were obtained by a trial-and-error procedure on the training dataset. The third case makes use of the optimal solution described in the previous section and produces the following weights $\pi_1 = 0.3157$, $\pi_2 = \pi_3 = 0.2955$

and $\pi_4 = 0.0933$. Figure 4.5 presents the confusion matrices for each one of these two cases. As observed in Fig. 4.5 (a), the use of equal priors does not produce a balanced classifier. This is caused by the fact that the eigenvalues that scale each exponential function have been removed for easing the computation of the likelihood function. However, this operation is necessary since numerical issues tend to arise due to the high number of multiplications involved in the computation of the PDFs (For a SAR signal consisting of 1024 samples, the joint pdf of the slow-time vector is the multiplication of the 1024 PDFs corresponding to each sample). Fig. 4.5 (b) shows that by removing weight from hypothesis 3 (the hypothesis that captured the most number of samples in Fig. 4.5 (a)) a more balanced detector can be obtained. As shown in Figure 4.5 (c), the proposed procedure for optimally determining the priors for the likelihood ratio function is the one that produces the best classifier with an overall accuracy of 86.26%. Finally, when comparing the performance of the maximum-likelihood classifier with the performance of the MLAs as shown in Tab. 4.1, one can observe that the situation is similar to the binary detection problem. In particular, the maximum-likelihood classifier ranks third in performance in this demonstrative example using simulated SAR data.

4.3.4 Characterization of the performance in presence of noise and clutter

In this section, the performance of the proposed classification algorithms is evaluated in the presence of noise and clutter at different intensity levels. This task is done using datasets of the same characteristics as the simulated dataset describe in Sec. 4.3.1 but with different values of SNR and SCR. Specifically, two experiments are performed. First, while keeping $SCR = \infty$, the performance of the proposed classifiers is measured in terms of the overall classification accuracy at different SNR values. Second, while keeping $SNR = \infty$, the performance of the proposed classifiers

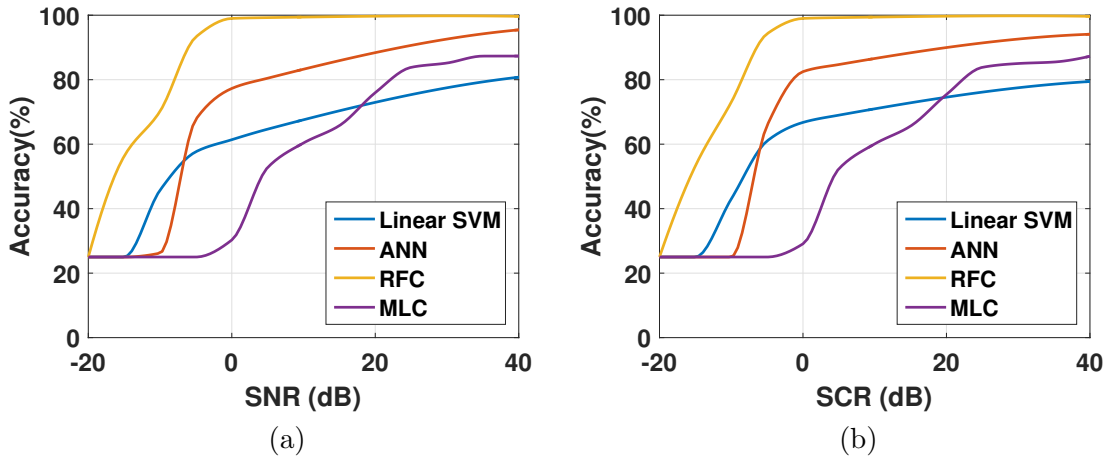


Figure 4.6: Performance characterization of the proposed *M*-ary detectors in terms of the overall classification accuracy at various noise and clutter intensity levels. (a) Performance vs. noise. (b) Performance vs. clutter.

is measured in terms of the overall accuracy at different SCR values. The results are shown in Fig. 4.6.

As can be observed in Fig. 4.6, the RFC is the detector that exhibits the best performance over all the tested SNR and SCR values. Particularly, the RFC shows to be reliable up to an SNR and SCR of -5 dB. For SNR and SCR values higher than 20 dB, the maximum-likelihood classifier ranks third. For any other SNR and SCR value, the maximum-likelihood classifier is the one that exhibits the lowest performance among the 4 tested classifiers. Finally, as in the case of the binary detection methodologies, the proposed classification algorithms have similar similar performance curves for clutter contamination and noise contamination.

Chapter 5

Preservation of class-separability of vibrations in SAR images

Preservation of class-separability of vibrations in SAR images is one important characteristic to study because it is an indicator of how appropriate is SAR as a tool for studying vibrations. Particularly, it is interesting to confirm that vibration waveforms, that are well-separable as displacement functions, remains well-separable as slow-time signals collected by a SAR. This study is performed by training MLAs with a library of vibrations of machinery from the Ford Utility Building (FUB) and the Structural Engineering and Materials Laboratory at *The University of New Mexico* (UNM). The analysis focuses on a library of machine vibrations containing vibration history data from 8 different sources: a car engine, an industrial cooling fan, an industrial exhaust, a power generator, a laboratory mixer, an industrial ventilation system, a turbine enclosure, and a laboratory ventilation system. Specifically, the MLAs presented in Sec. 3.1 are used to study the capability to separate these types of vibrations. First, the separability of these 8 types of vibrations is analyzed by studying MLAs trained with features extracted directly from the displacement waveforms. In other words, Alg. 1 is applied directly to the vibration displacement

history data instead of IF curves. Second, the preservation of the separability of these classes is studied using MLAs trained with features extracted from simulated SAR images generated by the recorded displacement history data and the SAR signal model (2.6). In this case, the feature extraction process is performed on simulated SAR slow-time data via estimation of the IF of the signal as its indicated in Alg. 1. Finally, the classification performance of the MLAs is studied to analyze the effect that SAR produces as a sensor. Figure 5.1 summarizes all the steps involved in this analysis.

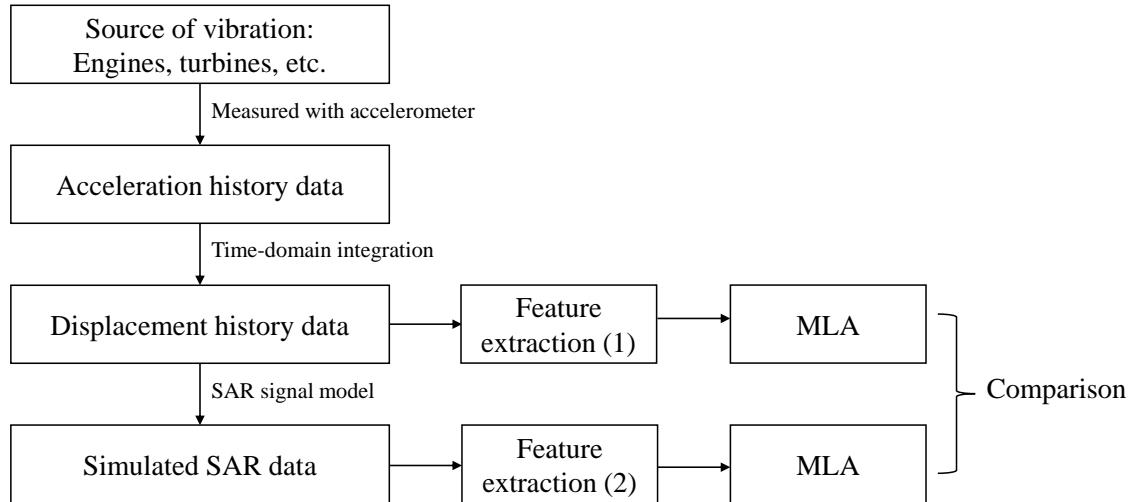


Figure 5.1: Steps involved in the study of the preservation of class-separability of vibrations in SAR images. The feature extraction process (2) uses the IF of the slow-time signal as an estimation of the displacement history data in Alg. 1. The feature extraction process (1) uses directly the displacement history data instead of the IF in Alg. 1.

5.1 Library of machine vibrations

For this study a library consisting of machine vibrations of 8 different sources was compiled. The vibration history data was collected at the Ford Utility Building

(UNM's power plant) and the Structural Engineering and Materials Laboratory at UNM. The 8 classes of vibrations are: (i) a car engine idling, (ii) an industrial cooling fan, (iii) an industrial exhaust, (iv) a power generator, (v) a laboratory mixer, (vi) an industrial ventilation system, (vii) a turbine enclosure and (viii) a laboratory ventilation system. The library contains a total of 6960 samples (870 samples per class) and each sample is a 1 second acceleration history data. In order to study the separability and its preservation under SAR processing, a total of 5600 samples (700 samples per class) are used to train classifiers and the remaining 1360 samples (170 samples per class) are used to test their performance. Prior feature extraction and SAR processing, the acceleration history data is converted to displacement history data via time-domain integration. Figures 5.2, 5.3, and 5.4 presents pictures of the 8 classes of machines and plots of their respective displacement history data. As can be observed, some vibration patterns are very unique, e.g. class 1 and 4, but others have certain resemblance, e.g. class 3 and 7.

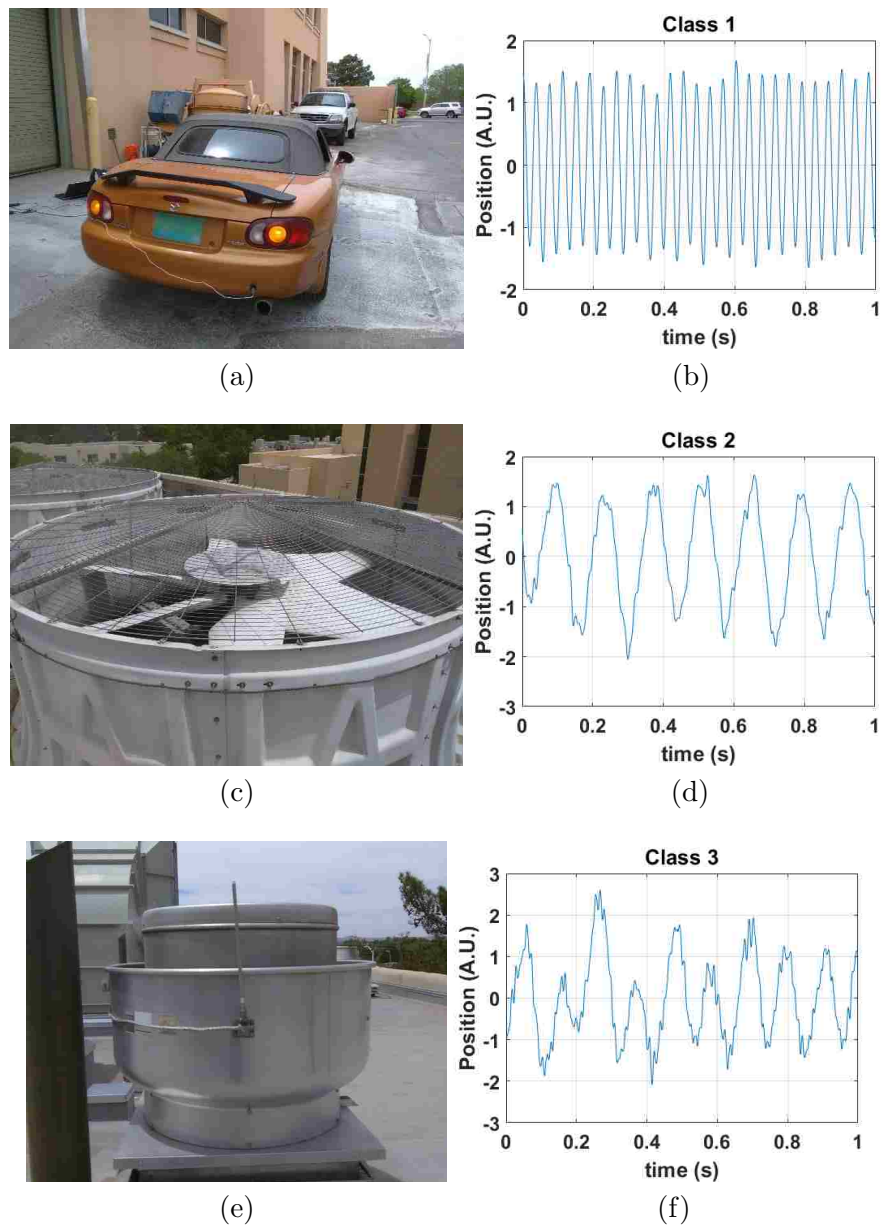


Figure 5.2: Classes that conform the machine vibration library, Fig. No. 1 of 3. Left-handside column: machine, right-handside column: its respective vibration displacement waveforms. (a,b) Car, (c,d) cooling fan (Ford Utility Building), (e,f) exhaust (Ford Utility Building). The displacement functions have been normalized by their standard deviation.

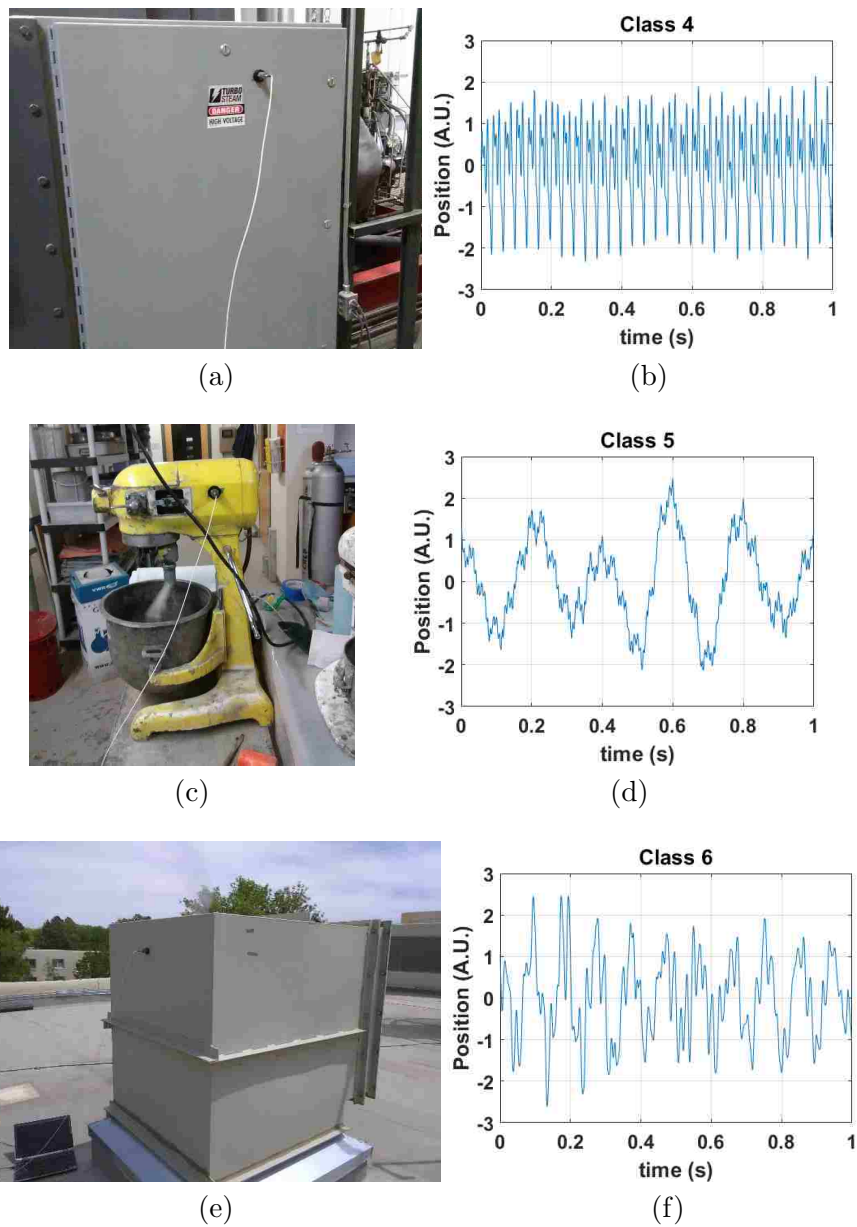


Figure 5.3: Classes that conform the machine vibration library, Fig. No. 2 of 3. Left-handside column: machine, right-handside column: its respective vibration displacement waveforms. (a,b) steam power generator (Ford Utility Building), (c,d) mixer (Structural Engineering and Materials Laboratory), (e,f) square vent (Ford Utility Building). The displacement functions have been normalized by their standard deviation.

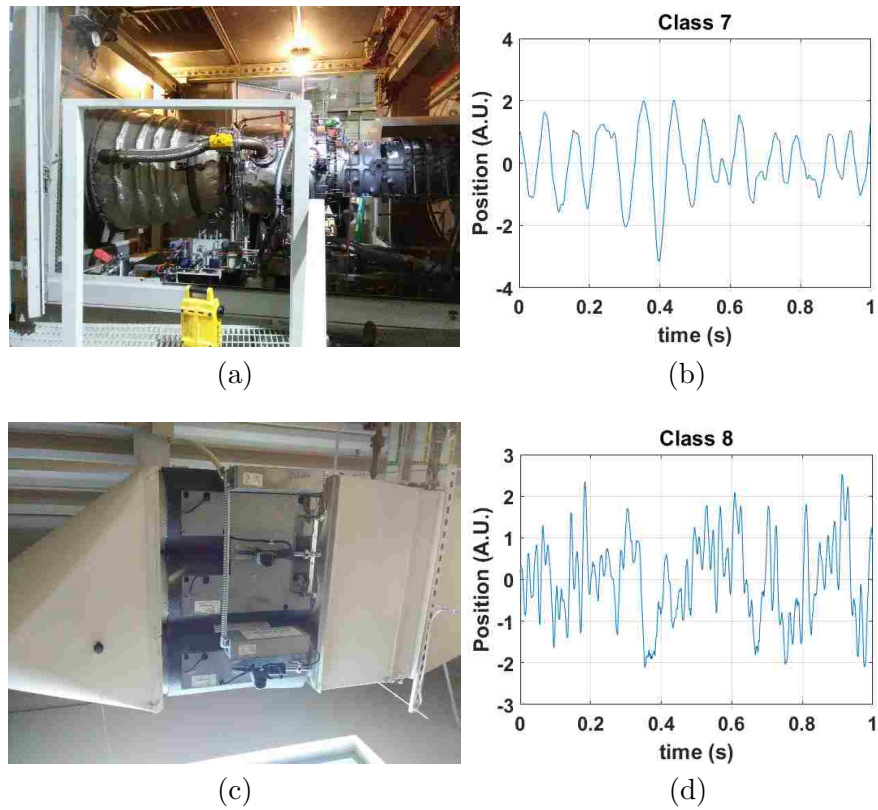


Figure 5.4: Classes that conform the machine vibration library, Fig. No. 3 of 3. Left-handside column: machine, right-handside column: its respective vibration displacement waveforms. (a,b) turbine (Ford Utility Building), (c,d) vent (Structural Engineering and Materials Laboratory). The displacement functions have been normalized by their standard deviation.

5.2 Separability test

This study is carried out by using displacement history data recovered from the integration of the vibration acceleration data. Then, the feature extraction process described in Sec. 3.1 directly applied on the vibration displacement waveform instead of the IF. As studied in Sec. 3.1, a linear SVM classifier, a neural network with 2 hidden layers and a random forest classifier are trained for comparison. The perfor-

mance of each classifier is reported using the accuracy metric, confusion matrices and ROC curves. The feature usage in the construction of the random forest classifier is also investigated.

As can be observed in Table 5.1 and Figs. 5.5 and 5.6, the random forest and the neural network achieve high performance on this classification problem. The lower performance of the linear classifier is in direct relation with features distributed in a non-linear in the feature space. Also, Fig. 5.7 reveals that the most important features for the classification of these 8 type of vibrations are the vibrations statistics and peaks in the DFRFT plane. However, it seems that the histogram is also assisting the classification process. Based on the results reported here, it can be established that the classes are separable and that the feature extraction approach ensures high-performance classification of machine-specific types of vibrations.

Table 5.1: Separability of displacement waveforms. Average accuracy (%) of the classifiers when distinguishing between 8 classes.

Classifier	Simulated training set	Simulated testing set
Linear SVM	58.31	47.94
Neural Network	73.33	64.20
RFC	93.56	93.89

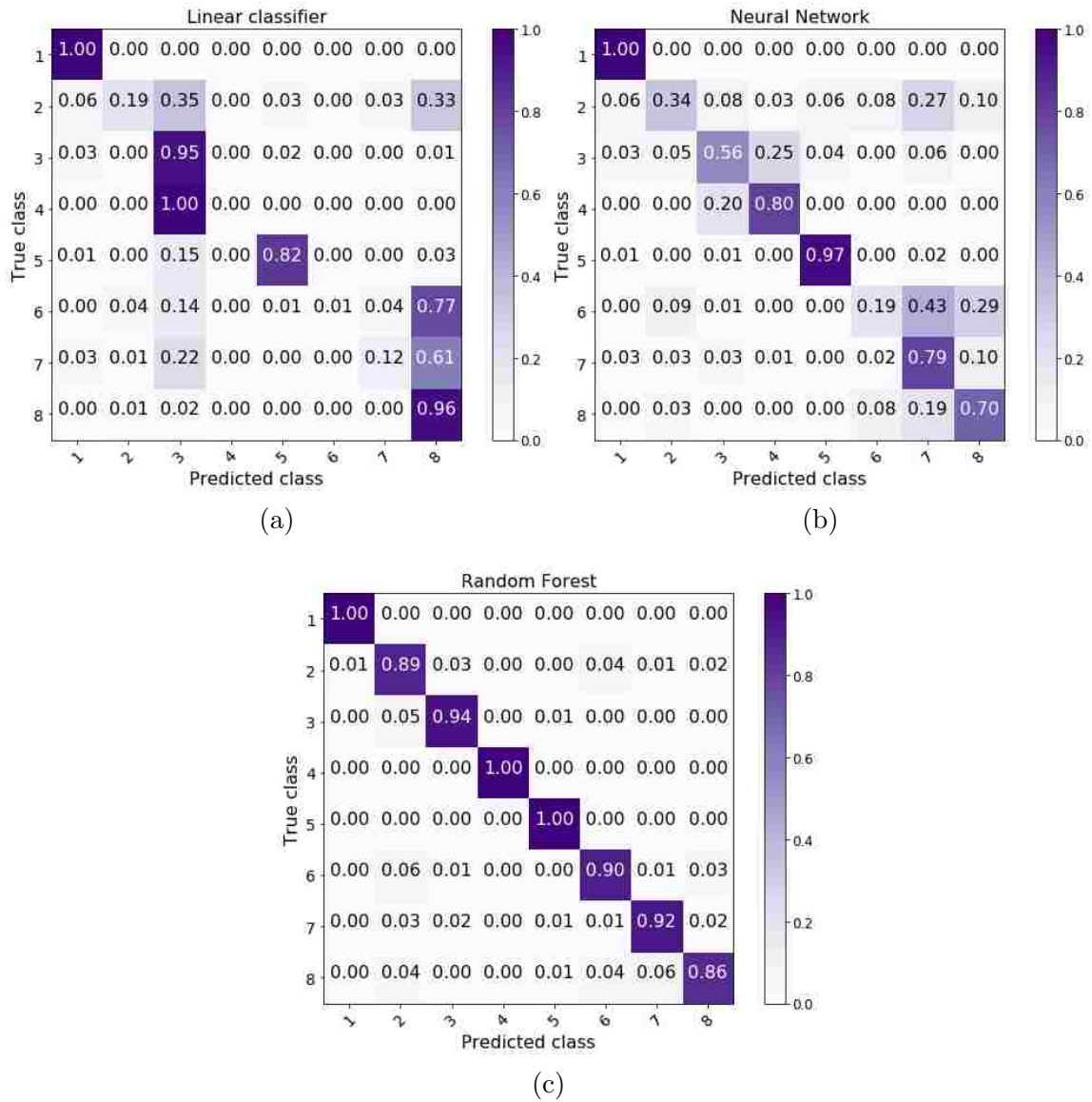


Figure 5.5: Normalized confusion matrices evaluated on a testing set formed by vibration displacement waveforms. (a) Linear classifier. (b) Neural Network. (c) Random Forest.

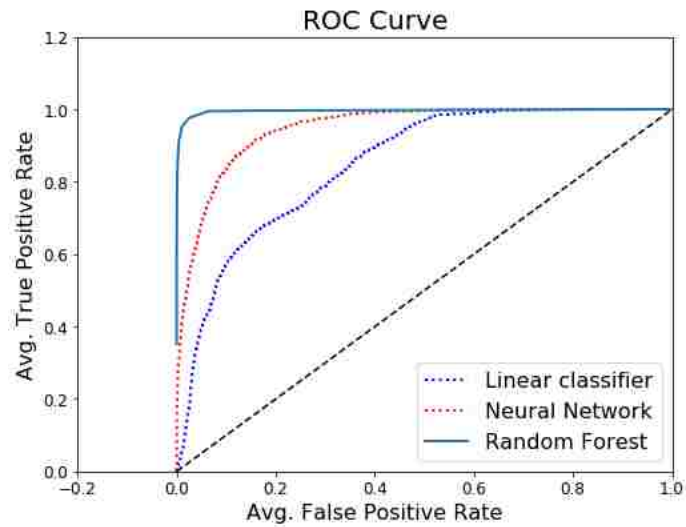


Figure 5.6: Eight-class average ROC curve evaluated on a testing set formed by vibration displacement waveforms. The corresponding area under the ROC curve is 0.848 for the Linear SVM, 0.947 for the Neural Network and 0.995 for the Random Forest classifier.

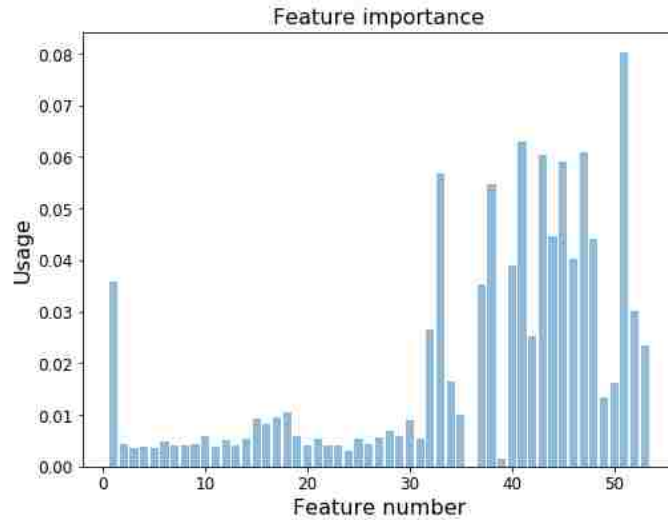


Figure 5.7: Feature usage of the constructed Random Forest classifier, 8-class classification problem. The training was performed on a dataset formed by vibration displacement waveforms. The features #1-32 correspond to histogram values. The features #33-35 are statistics. The features #36-53 are the relative magnitude, frequency index and chirp rate index of the 6 highest peaks in the DFRFT plane.

5.3 Preservation of the separability in SAR sensing

For this study simulated slow-time SAR data is generated using displacement history data from the 8 classes of vibrating objects. Then, the feature extraction process described in Sec. 3.1 is applied. The goal is to verify that the SAR processing does not cause detriment on the separability of the 8 classes. As in the previous case, a linear classifier, a neural network with 2 hidden layers and a random forest classifier are trained for comparison. The performance of each classifier is reported using the accuracy metric, confusion matrices and ROC curves. The feature usage in the construction of the random forest classifier is also studied.

Table 5.2: Separability of SAR signals generated from displacement waveforms. Average accuracy (%) of the classifiers when distinguishing between 8 classes.

Classifier	Simulated training set	Simulated testing set
Linear SVM	53.64	51.61
Neural Network	86.66	77.90
RFC	94.75	95.00

As can be observed in Table 5.2 and Figs. 5.8 and 5.9, the performance of classifier trained with the new SAR simulated data is similar to the performance of the previous classifiers trained directly with the displacement waveforms. More specifically, it can be observed a small drop in performance in the linear classifier and an improvement in the performance of the neural network and random forest. The increment in performance is caused by the non-linear processing of the SAR signal which employs the Pseudo-Wigner Ville time-frequency distribution to estimate the IF (vibration displacement waveform). This shows that non-linear processing of a vibration waveform can help to improve the classification performance of some classifiers. Also, Fig. 5.10 reveals that the most important features for the classification

Chapter 5. Preservation of class-separability of vibrations in SAR images

of these 8 type of vibrations are the vibrations statistics and peaks in the DFRFT plane. However, in contrast with the previous case, we observe that less relevance is assigned to the histogram values in comparison with the statistic and DFRFT peaks. Based on the results reported here, it can be establish that SAR processing preserves the separability property of different types of vibrations. Furthermore, the results show that the approach used here can be employed to build robust classifiers that can deal with machine-specific types of vibrations

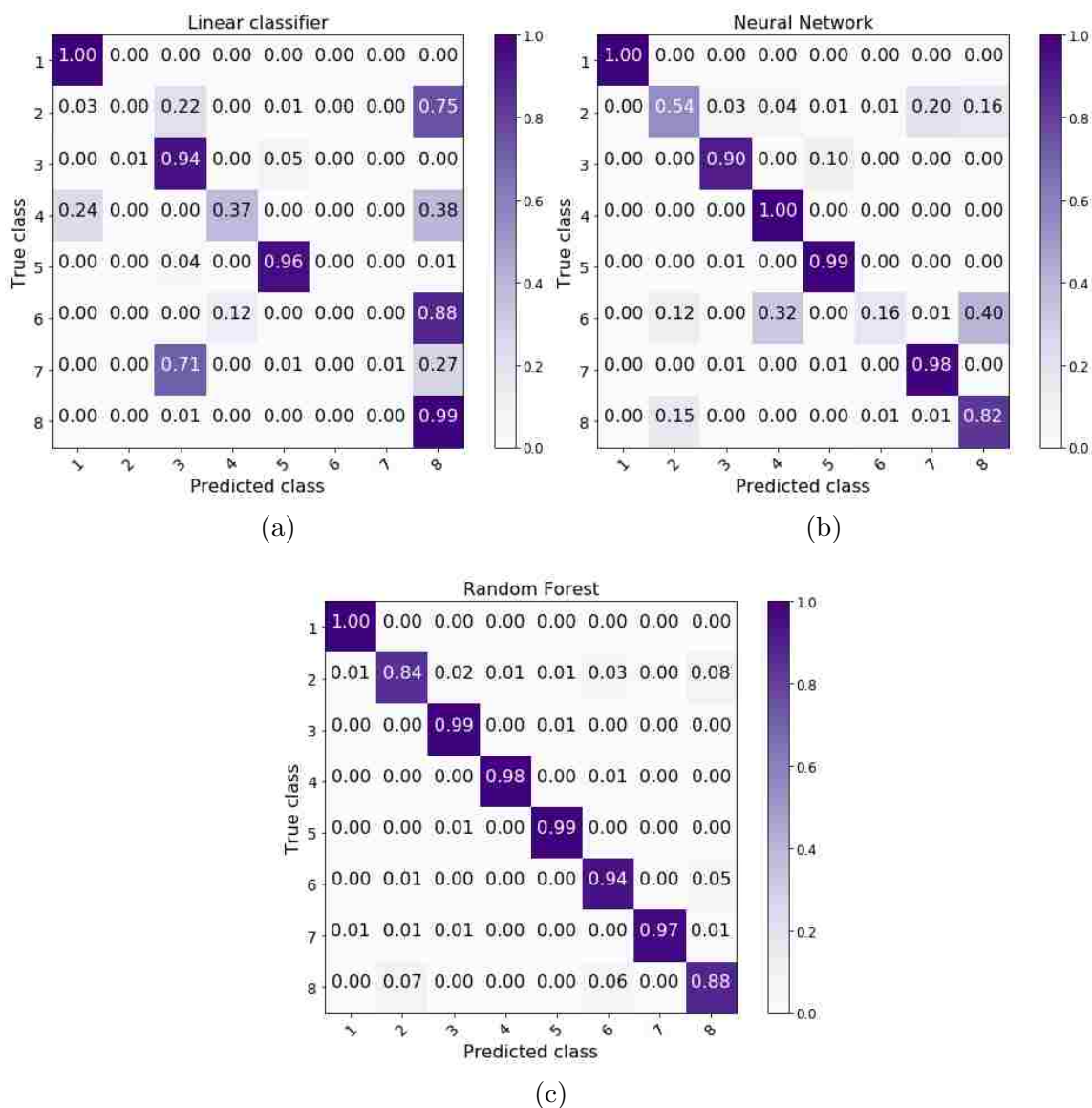


Figure 5.8: Normalized confusion matrices evaluated on a testing set formed by SAR signals generated from vibration displacement waveforms. (a) Linear classifier. (b) Neural Network. (c) Random Forest.

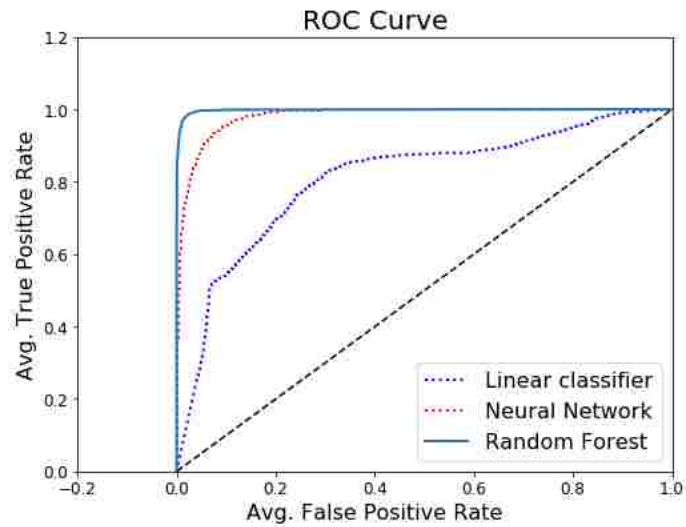


Figure 5.9: Eight-class average ROC curve evaluated on a testing set formed by SAR signals generated from vibration displacement waveforms. The corresponding area under the ROC curve is 0.808 for the Linear SVM, 0.980 for the Neural Network and 0.997 for the Random Forest classifier.

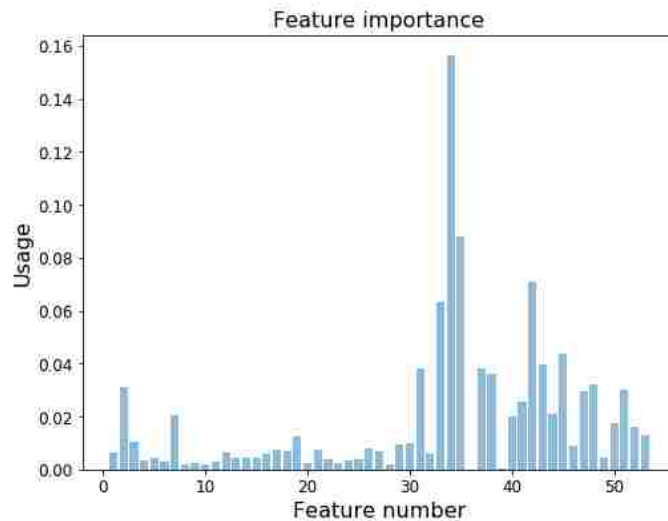


Figure 5.10: Feature usage of the constructed Random Forest classifier using simulated SAR data, 8-class classification problem. The training was performed on a dataset formed by SAR signals generated from vibration displacement waveforms. The features #1-32 correspond to histogram values. The features #33-35 are statistics. The features #36-53 are the relative magnitude, frequency index and chirp rate index of the 6 highest peaks in the DFRFT plane.

5.4 Classification test using pre-built classifiers

The simulated SAR data generated with the the library of machine vibration was also tested using the MLAs trained to distinguish between vibrating and non-vibrating object of Sec. 3.1. It must be noted that for this experiment all the data correspond to simulated SAR signals from vibrating objects, since the library of machine of vibration do not contain static objects. The classification results are summarized in Table 5.3. As can be observed, the overall classification performance is high. Particularly, the NN overperforms the RFC and the linear SVM, being the last one the worse of the three. The reason behind the poor performance of the linear classifier may be mainly attributed to a non-linear distribution of the features of these 8 classes in the feature space.

Table 5.3: Classification of machine vibration data using the binary MLA of Sec. 3.1. Each column contains the total % of samples classified in each class.

Class \ Classifier	Linear SVM	Neural Network	RFC
Static Object	36.44%	3.26%	10.53%
Vibrating Object	63.56%	96.74%	89.47%

Chapter 6

Clutter-noise suppression via Hankel rank reduction

The HRR is a technique that, by pre-arranging the data in a Hankel matrix and performing rank reduction via singular value decomposition, suppresses noise of a time-history vector comprised of the superposition of a finite number of sinusoids [16, 34–36]. Previously in [16], the author of this dissertation demonstrated the capabilities of the HRR technique for enhancing a DFRFT-based vibration estimation algorithm for SAR. In this chapter, the HRR technique is studied for aiding on the detection and classification of vibrating objects in SAR images at low values of SNR and SCR. Specifically, the SAR data is pre-processed using the HRR technique before it is presented to the detection and classification algorithms.

6.1 The Hankel rank reduction method

Let $s[n]$, $n = 1, \dots, N$ be a sampled signal composed of m superimposed sinusoids, whose instantaneous frequencies vary slowly with time. Then, the Hankel matrix of

size $(N - L + 1) \times L$ of the time series $s[n]$ can be written as

$$\mathbf{H} = \begin{pmatrix} s[1] & s[2] & \dots & s[L] \\ s[2] & s[3] & \dots & s[L+1] \\ \vdots & \vdots & \ddots & \vdots \\ s[N-L+1] & s[N-L+1] & \dots & s[N] \end{pmatrix}, \quad (6.1)$$

where $L \ll N$ and L is of order $3m$. It has been demonstrated that when the instantaneous frequencies of the sinusoids do not vary significantly over L time steps, the rank of \mathbf{H} will be close to $2m$, [34]. On the other hand, if the instantaneous frequencies are strongly time-varying, \mathbf{H} will be full rank. By means of SVD, the Hankel matrix \mathbf{H} can be expressed as

$$\mathbf{H} = \mathbf{U}\mathbf{S}\mathbf{V}^T = \sum_{j=1}^P \sigma_j \mathbf{u}_j \mathbf{v}_j^T \quad (6.2)$$

where $\mathbf{S} = \text{diag}[\sigma_1, \dots, \sigma_P]$ and $\sigma_1, \dots, \sigma_P$ are the singular values of \mathbf{H} in decreasing order of magnitude; and \mathbf{U} and \mathbf{V} are matrices containing the left- and right-singular vectors, \mathbf{u}_j and \mathbf{v}_j , $j = 1, \dots, P$, respectively. If the instantaneous frequencies of the sinusoids do not present significant variations and if the intensity of the noise is moderate or low, then most of the power of the signal $s[n]$ will be concentrated in the largest K singular values. Then, the $P - K$ smallest singular values can be neglected and \mathbf{H} can be approximated by

$$\tilde{\mathbf{H}} = \mathbf{U}_1 \mathbf{S}_1 \mathbf{V}_1^T = \sum_{j=1}^K \sigma_j \mathbf{u}_j \mathbf{v}_j^T. \quad (6.3)$$

Since $\tilde{\mathbf{H}}$ contains an ordered time structure, similar to that of \mathbf{H} in (6.1), then an approximation of $s[n]$ (after rank reduction) can be constructed by concatenating the first row with the last column of $\tilde{\mathbf{H}}$. In this manner, for cases in which the true signal $s[n]$ is contaminated with additive clutter and noise, one can recover a cleaner version of the $s[n]$ whenever the singular values of these perturbations have magnitude less than the largest K singular values of $s[n]$, [34–38].

6.2 Application to the machine-learning-based detection and classification framework

The objective of this study is to characterize the improvement in performance that the HRR technique provides to the detection and classification techniques based on MLAs when the SAR data presents low SCR and low SNR. Specifically, the study of performance described in Chapters 3.3 and 4.3 is repeated for SNR and SCR values from -20 dB to 0 dB. In this range of SNR and SCR, only a few singular values contain information from the return of the vibrating object, while the rest correspond to the clutter-noise signal. In consideration of this, a Hankel matrix of order 128 was constructed and only the 3 most significant singular values were preserved in the rank reduction step.

Figure 6.1 shows a comparison of the performance of the proposed detection and classification algorithms before and after pre-processing the SAR data with the HRR technique. As can be observed, there is a substantial improvement of the performance of all the studied algorithms. Particularly, in the detection problem the proposed algorithms now reach the 0.5 AUROC barrier at -15 dB for both SNR and SCR. This extends the use of this algorithms to -10 dB. Besides of extending the operating region of the proposed detectors, these results demonstrate the capabilities of the HRR for suppressing noise and clutter in the problem detecting and classifying vibrations in SAR images. A completely different situation happens in the m-ary classification problem where the proposed algorithms tend to perform worse in terms of the overall accuracy when the SAR data is pre-processed with the HRR technique. Similar results were obtained when retaining 6, 12 and 24 singular values in the rank reduction process. The reason behind this phenomenon is likely to be the fact that the signal subspace is different for each one of the classes under study and, consequently, the number of singular values that correspond to the signal is not the same in all

the cases. Therefore, since the class of each slow-time signal is not known, the ideal number of singular values cannot be known a priori. This conclusion renders the HRR unusable for the M-ary classification problem using MLAs unless a methodology for addressing this issue is developed.

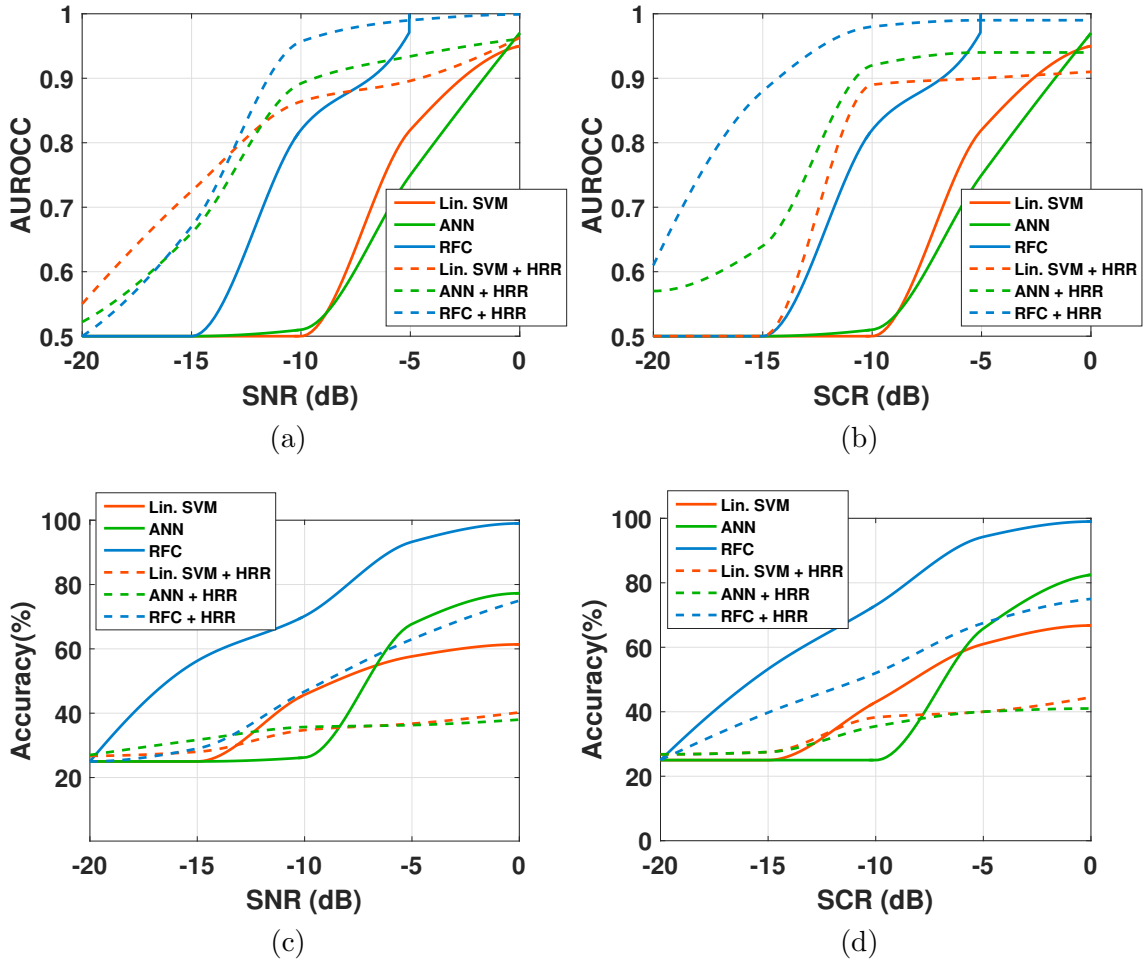


Figure 6.1: Performance characterization of the detection and classification algorithms based on MLAs using the HRR technique for noise and clutter suppression. (a,b) Performance of the MLAs for the detection problem in the presence of noise and clutter, respectively. (c,d) Performance of the MLAs for the classification problem in the presence of noise and clutter, respectively.

6.3 Application to the probabilistic detection and classification framework

The objective of this study is to characterize the improvement in performance that the HRR technique affords to the probabilistic detection and classification techniques when the SAR data presents low SCR and low SNR. Specifically, the study of performance described in Chapters 3.3 and 4.3 is repeated for SNR and SCR values from -20 dB to 0 dB. Similarly to the previous section, a Hankel matrix of order 128 was constructed and only the 3 most significant singular values were preserved in the rank reduction step.

Figure 6.2 shows a comparison of the performance of the proposed detection and classification algorithms before and after pre-processing the SAR data with the HRR technique. As can be observed, there is a substantial improvement in the performance of all the studied algorithms. Particularly, there is an improvement of 0.15 to 0.20 points in terms of the AUROC of the detection algorithm and an improvement of 3% to 8% in terms of the overall accuracy of the classification algorithm. These results extend the operating region of the proposed detectors and classifiers, and demonstrate the capabilities of the HRR for suppressing noise and clutter in the problem detecting and classifying vibrations in SAR images.

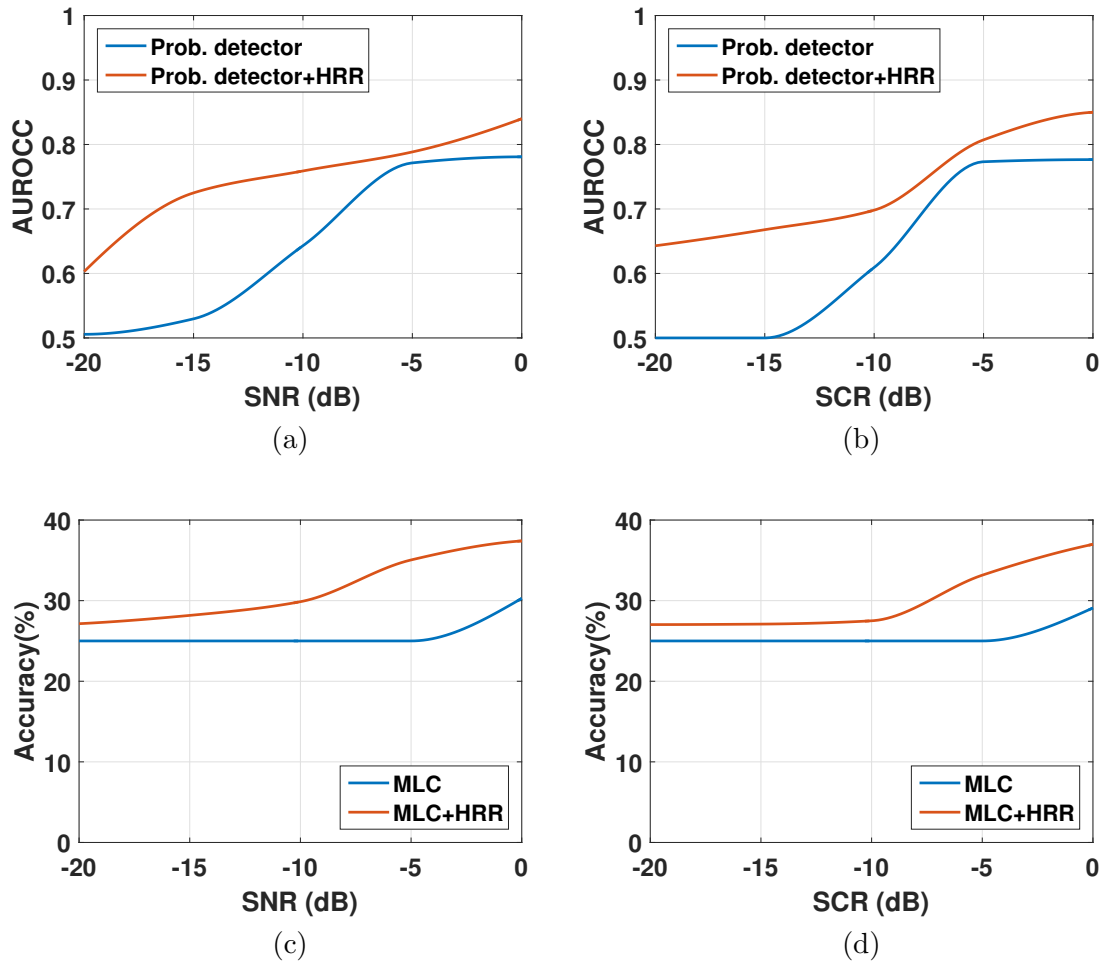


Figure 6.2: Performance characterization of the probabilistic detection and classification algorithms using the HRR technique for noise and clutter suppression (a,b) Performance of the prob. detector in the presence of noise and clutter, respectively. (c,d) Performance of the prob. M-ary classifier in the presence of noise and clutter, respectively.

Chapter 7

Conclusions

7.1 Summary and conclusions

In this dissertation, novel algorithms have been developed to classify and detect vibrating objects using SAR images. The capability of remote detection and classification of vibration signals would greatly benefit both the diagnosis of failures and the characterization of operating condition of structures and machines with limited physical accessibility. Since the vibrations observed on the exterior surface of buildings and structures are intrinsically linked to the machinery and equipment operating inside of them, the capability of remotely detect vibrations also enables one to perform identification of concealed machinery. Furthermore, the introduction of this new functionality to SAR enriches the diversity of applications for which a SAR would be preferred over other remote-sensing technologies.

The work performed in this dissertation was conducted around following three central claims. First, the non-linear transformation that the micro-Doppler return of a vibrating object suffers through SAR sensing does not destroy its information. Second, the IF of the SAR signal has sufficient information to characterize vibrating

Chapter 7. Conclusions

objects. Third, it is possible to develop a detection model that encompasses multiple scenarios including both mono-component and multi-component vibrating objects immersed in noise and clutter.

These claims have been cemented by the development and study of two different schemes for both the detection and M-ary classification of vibrating objects in SAR images. The first scheme is data-driven and utilizes features extracted with the help of the DFRFT to feed MLAs. Specifically, the DFRFT is applied to the IF of the slow-time SAR data, which is reconstructed using enhanced spectrograms based on the SPWVTFD and the DFRFT. The MLAs studied in this work are: a linear SVM, a 3-layer fully-connected NN, and a RFC. The second scheme is model-based and employs a probabilistic model of the SAR slow-time signal, the KLT, and a likelihood-based decision function. Particularly, the KLT is used to decorrelate the samples of the SAR slow-time signal via SVD. The performance of the two proposed detection schemes is characterized using simulated data as well as real SAR data collected with the Lynx SAR system. The results shows that the two proposed schemes can be used to achieve high-performance vibrating-object detectors and classifiers for SNRs and SCRs greater than -5 dB. Among the proposed detection methodologies, the data-driven detection scheme based on MLAs showed to be superior to the probabilistic detection scheme for moderate to high SNR and SCR values. In the case of low SNR and SCR and, in the presence of modeling errors, the probabilistic detection methodology was shown to be superior to the machine-learning-based methodology.

The suitability of SAR for sensing surface vibrations is demonstrated by showing that the separability of different classes of vibrating objects is preserved even after non-linear SAR processing. For this purpose, an empirical experiment has been performed using MLAs, a library of vibration data from real machines (instantaneous position data) and simulated SAR data. Specifically, the simulated SAR data was generated using the machine-vibration data as input for the micro-Doppler return of

a vibrating object (point-object). The classification results of a set of two MLAs, one trained with the real vibration data and the other with the simulated SAR data, show that the separation of classes produced by the MLA trained with simulated SAR data is the same that the one provided by the MLA trained with the machine-vibration data.

Finally, in order to loosen the SNR and SCR requirements, the HRR technique, previously used for suppressing ocean clutter in ground-wave radar, was adapted to suppress clutter-noise in SAR images. The result shows that the proposed detection schemes yields reliable results for SNRs and SCRs greater than -10 dB when the SAR images are pre-processed with the HRR method. This extends the capabilities of the proposed detection and classification algorithms in presence of noise and clutter, and also corroborates the fitness of the HRR technique for performing noise and clutter suppression in SAR imaging.

7.2 Suggestions for future work

The experimental and theoretical results presented in this dissertation in regard to the problem of detection and classification of vibrating objects in SAR images open numerous possibilities for future research including:

- The extension of the proposed detection models to multiple objects exhibiting different vibrations patterns, which can be coupled or not. This will render the proposed detection techniques useful in a larger number of scenarios not limited to the case of isolated objects.
- The extension of the detection model from a point object to more complex object-models, such as cars, fans, or any piece of equipment of interest, will

Chapter 7. Conclusions

certainly improve the performance of the proposed detection methodologies in a real-case scenario.

- The study of more advanced types of MLAs such as complex kernels for SVMs, recurrent neural networks, long short-term memory networks, or convolutional neural networks, can also improve the performance of the proposed methodology based on MLAs in the case of low SNR and low SCR, and be useful for overcoming modeling errors in the datasets. Also, another possibility when features do not provide an evident separation of the classes, is the usage of feature weighting as proposed in [39].
- The adaptation of the proposed detection and classification methodologies to a *displaced-phase-center antenna* (DPCA)-SAR framework is also of great interest since this remote sensing technique provides for clutter and noise suppression in a natural way by combining the information of two perfectly timed SAR images. This will certainly improve the performance of the detection and classification of vibrating objects at very low SNRs and SCRs.
- The development of computationally-optimized forms of the proposed detection and classification methodologies is also very appealing for their implementation in real-time applications in SAR systems. For instance, most of the computational load of the proposed technique based on MLAs is in the feature extraction step that uses the DFRFT. In this regards, it would be appealing to develop new algorithms to reduce the computational burden of constructing the matrix of Grünbaum (or QMFD) eigenvectors.

Appendix A

Vibration detection based on the CSD of the SAR signal

Consider the signal model presented in Chapter 2. The detection model proposed by *Subotic et al.* [19] can be summarized as follows:

Algorithm 4 Vibration detection via the generalized likelihood ratio of the CSD.

- 1: $\mathbf{s} = [s[0], \dots, s[N - 1]]^T$: a slow-time vector from a SAR image.
 - 2: Regenerate all the cyclic frequencies contained in the slow-time vector via CSD, i.e.:
 - 3: **for all** $\alpha \in \{k/T\}_{-\infty}^{\infty}$: cyclic frequencies **do**
 - 4: Compute the CACF: $R_s^\alpha(\tau)$
 - 5: Compute the CSD: $S_s^\alpha(f)$
 - 6: **end for**
 - 7: $\forall \alpha \in \{k/T\}_{-\infty}^{\infty}$, correlate $S_s^\alpha(f)$ with a stored template $S_v^\alpha(f)$ of the expected SAR signal of the vibration.
 - 8: Sum all the correlation results for $\alpha \in \{k/T\}_{-\infty}^{\infty}$.
 - 9: Compare the sum with a threshold to determine if \mathbf{s} belongs either to H_0 or H_1 .
-

Appendix B

Smoothed pseudo Wigner-Ville time-frequency distribution

Below the description of the *Wigner-Ville time-frequency distribution* (WVTFD) and SPWVTFD is presented. The implementation of these time-frequency distributions for a discrete-time signal is straightforward and the details are provided in [40].

The WVTFD of an analytic signal $x(t)$ is a bilinear transform defined as the Fourier transform of the time-dependent autocorrelation function

$$W_x(t, \omega) = \int_{-\infty}^{\infty} x\left(t + \frac{\tau}{2}\right) x^*\left(t - \frac{\tau}{2}\right) \exp(-j\omega\tau) d\tau, \quad (\text{B.1})$$

where $x(t + \tau/2)x^*(t - \tau/2)$ is a time-dependent autocorrelation operation, [10, 27, 40, 41]. The WVTFD has better joint time-frequency resolution than any linear transform, but suffers from a problem of cross-term interference, i.e., the WVD of the sum of two signals is not the sum of their individual WVDs, [10, 27]. If a signal contains more than one component in the joint time-frequency domain, its WVD will contain cross terms that occur halfway between each pair of auto-terms. The magnitude of these oscillatory cross terms can be twice as large as the

Appendix B. Smoothed pseudo Wigner-Ville time-frequency distribution

auto-terms [10]. To reduce the cross-term interference, while maintaining high time-frequency resolution, a couple of filtered versions of the WVD has been proposed. Particularly, the pseudo WVTFD with separable-smoothing, [27, 40], also known as SPWVTFD, is defined as

$$SPW_x(t, \omega) = \int_{-\infty}^{\infty} h'(\tau) \left[\int_{-\infty}^{\infty} g(s-t) x \left(s + \frac{\tau}{2} \right) x^* \left(s - \frac{\tau}{2} \right) ds \right] \exp(-j\omega\tau) d\tau, \quad (\text{B.2})$$

which employs a window of the form $h'(\tau) = h^*(\tau/2)h(-\tau/2)$ and a window $g(t)$ for providing frequency and temporal smoothing on (B.1), respectively. Here the separable smoothing function can be succinct as $k(\varepsilon, \tau) = G(\varepsilon)h'(\tau)$ or equivalently by its Fourier transform $K(t, \omega) = g(t)H'(-\omega)$.

Note: If $g(t) = \delta(t)$, (B.2) is reduced to the commonly known pseudo WVTFD and if, in addition, $h(\tau) \rightarrow 1$, then the resulting time-frequency distribution tends to the original WVTFD with no smoothing applied.

Appendix C

Multi-angle centered-discrete fractional Fourier transform

The continuous-time fractional Fourier transform is a time-frequency analysis tool for non-stationary signals that was first introduced by V. Namias in 1980 [42]. Santhanam and McClellan [43] were the first to introduce a formulation of the DFRFT. While a variety of formulations of the DFRFT can be found in the literature [44], the DFRFT formulation used in this work is specifically referred to as the MA-CDFRFT in the literature [45]. Without ambiguity, the term DFRFT is used to refer to the MA-CDFRFT for the rest of this work.

Let \mathbf{W} denote the transformation matrix of the centered-DFT. The fractional power of \mathbf{W} is defined as $\mathbf{W}_\alpha = \mathbf{V}_G \mathbf{\Lambda}^{\frac{2\alpha}{\pi}} \mathbf{V}_G^T$ where \mathbf{V}_G is the matrix of Grünbaum eigenvectors of \mathbf{W} , and $\mathbf{\Lambda}^{\frac{2\alpha}{\pi}}$ is a diagonal matrix with the fractional powers of the eigenvalues of \mathbf{W} . Assume $x[n]$ is a sequence of N samples. The DFRFT of $x[n]$ is the DFT of an intermediate signal $\hat{x}_k[p]$ for each index k , that is

$$X_k[r] = \sum_{p=0}^{N-1} \hat{x}_k[p] \exp\left(-j \frac{2\pi}{N} pr\right), \quad (\text{C.1})$$

Appendix C. Multi-angle centered-discrete fractional Fourier transform

where $r = 0, 1, \dots, N - 1$ is the angular index and the corresponding α equals to $2\pi r/N$. The intermediate signal $\hat{x}_k[p]$ is calculated by

$$\hat{x}_k[p] = v_p^{(k)} \sum_{n=0}^{N-1} x[n] v_p^{(n)}, \quad (\text{C.2})$$

where $v_p^{(k)}$ is the k th element of v_p , and v_p is the p th column vector of \mathbf{V}_G .

The DFRFT has the ability to concentrate a linear chirp into a few coefficients, producing an impulse-like transform analogous to what the DFT produces for a sinusoid, [45–47]. It has also been proven that the mapping from the angular position of the peak in the DFRFT plane to the chirp rate of a signal is one-to-one [45]. Because the chirp rates induced by mechanical vibrations tend to be very small, a resolution enhancement algorithm, called the *chirp z-transform* (CZT), is usually incorporated as a final step of the DFRFT. Specifically, the CZT produces a more finely spaced interpolation of the DFT spectrum and its application to the DFRFT is intended for enhancing the angular resolution of the transform, [48–50].

Note: The description of the DFRFT presented here corresponds to the common form of the MA-CDFRFT. For implementation purposes is highly recommendable to use the formulations provided in [51, 52].

Appendix D

DFRFT-based spectrogram

The DFRFT-based spectrograms [28–30] are improved spectrogram that assumes a multicomponent chirp model over the analysis frame by using the centered DFRFT and the MA-CDFRFT to decompose the signal frame into a superposition of chirp signals. Particularly, a fractional spectrogram overcomes the problem that traditional spectrograms have for focusing chirp signals. Among the reported fractional spectrogram [30], one of the most appealing implementations is the piece-wise linear fractional spectrogram due to its simplicity and performance. Specifically, a piece-wise linear fractional spectrogram is constructed as follows. For every analysis frame, first the DFRFT is computed. Then, the peaks on the DFRFT plane are connected via a piece-wise linear fitting. Then, the points on the piece-wise linear function are used to populate the spectrogram for that particular frame. Finally, by applying this procedure over each frame, a spectrogram with sharper features than the conventional spectrogram is constructed. The mathematical details of this are provided below.

Piece-wise linear fractional spectrogram, [29]

The chirp term of signals manifest as peaks in the DFRFT plane. When one has

Appendix D. DFRFT-based spectrogram

prior knowledge of the number of chirps in the signal, one can use the location of all the peaks while calculating the spectrogram rather than using only the largest peak. This enables one to construct a sharp spectrogram even if the peaks do not lie on the same line. The piece-wise linear spectrogram uses the coordinates of the chirp peaks to calculate line segments. Let $[k_p^i, r_p^i]$ be the coordinates of peaks in the DFRFT-plane, M the number of chirps terms and N the size of DFRFT. Then, the piece-wise linear spectrogram r_{pw} for a frame is calculated as:

$$\begin{aligned}
 r_{pw}^1(k) &= \frac{r_p^2 - r_p^1}{k_p^2 - k_p^1} (k - k_p^1) + r_p^1, & 0 \leq k < k_p^2 \\
 r_{pw}^2(k) &= \frac{r_p^3 - r_p^2}{k_p^3 - k_p^2} (k - k_p^2) + r_p^2, & k_p^2 \leq k < k_p^3 \\
 r_{pw}^i(k) &= \frac{r_p^{i+1} - r_p^i}{k_p^{i+1} - k_p^i} (k - k_p^i) + r_p^i, & k_p^i \leq k < k_p^{i+1} \\
 &\vdots \\
 r_{pw}^{M-1}(k) &= \frac{r_p^M - r_p^{M-1}}{k_p^M - k_p^{M-1}} (k - k_p^{M-1}) + r_p^{M-1}, & k_p^{M-1} \leq k < N
 \end{aligned} \tag{D.1}$$

Applying this method to each frame, we construct the piece-wise linear spectrogram that is sharper than a common slanted fractional spectrogram [28–30]. For real signals, the DFrFT spectrum is mirrored, therefore one can only have an even number of peaks, while for a complex signal one can have either an even or odd number of peaks. In the special case, a complex signal having only one chirp component, the line is calculated using the the zero chirp-rate and zero frequency coordinates.

Appendix E

Recovering IF signals: SPWVTFD and DFRFT-based spectrogram

In this section, a qualitative analysis between the SPWVTFD and the piece-wise linear DFRFT-based spectrogram is performed for recovering the IF of SAR slow-time signals. Particularly, the following cases are analyzed in which the IF of the slow-time signal contains a vibration-induced term by: a static object (i.e., no vibration), vibrating object with a single-component sinusoidal vibration, vibrating object with a multi-component sinusoidal vibration and vibrating object with a chirped vibration. Figure E.1 shows the real displacement functions used for the generation of the simulated SAR returns. Figure E.2 shows the results of applying the SPWVTFD to each one respective SAR signals.

Figure E.3 shows the results of applying the piece-wise linear DFRFT-based spectrogram to each one respective SAR signals. As can be observed when analyzing the three figures, the results of both techniques are quite similar in every case and both techniques are capable of reconstructing the original vibration waveform almost perfectly. The only case in which both techniques produce slightly distorted results, is

Appendix E. Recovering IF signals: SPWVTFD and DFRFT-based spectrogram

the case of the SAR signal containing a vibration-induced modulation from an object exhibiting a chirped vibration. In this case, the amplitude of the original signal is scaled as its frequency varies. Nevertheless, the representation produced in this case, even it is distorted, is sufficiently good to be distinguished from the other cases. Finally, it can be observed that definition of the Piece-wise linear spectrogram is higher than the one produced by the SPWVTFD. This is due to the parameters required to tune these time-frequency analysis to the SAR signal model simulated with the Lynx specifications, Tab. 2.1. Specifically, the SPWVTFD requires to be computed with a transformation of 32 samples, while the piece-wise linear DFRFT-based spectrogram requires at least the use of a transformation of 256 samples. Nevertheless, because of the same previous reason, the computation of the SPWVTFD is faster than the DFRFT-based spectrogram for this problem.

Appendix E. Recovering IF signals: SPWTFD and DFRFT-based spectrogram

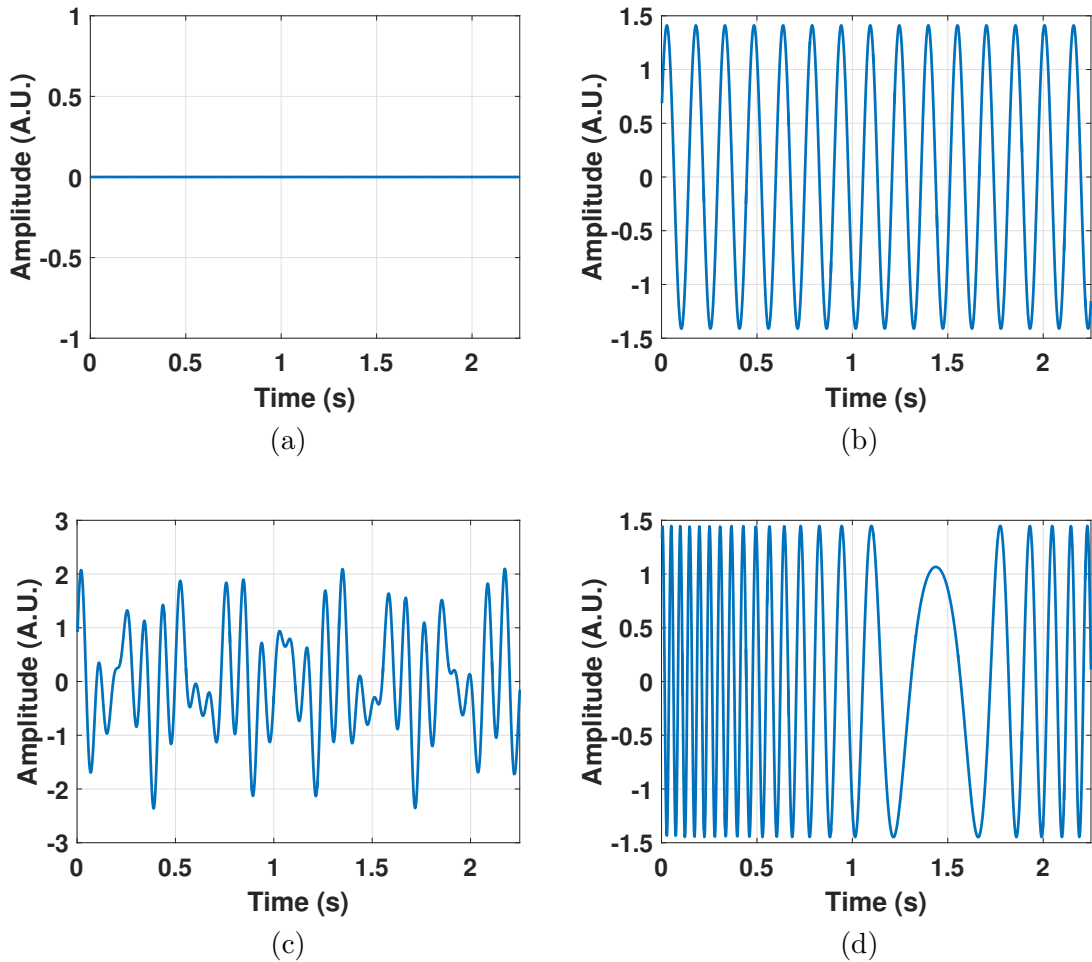


Figure E.1: Displacement functions used for the characterization of the SPWTFD and the Piece-wise linear DFRFT-based spectrogram. (a) Static object. (b) Mono-component sinusoidal vibration. (c) Multi-component sinusoidal vibration. (d) Chirped vibration.

Appendix E. Recovering IF signals: SPWVTFD and DFRFT-based spectrogram

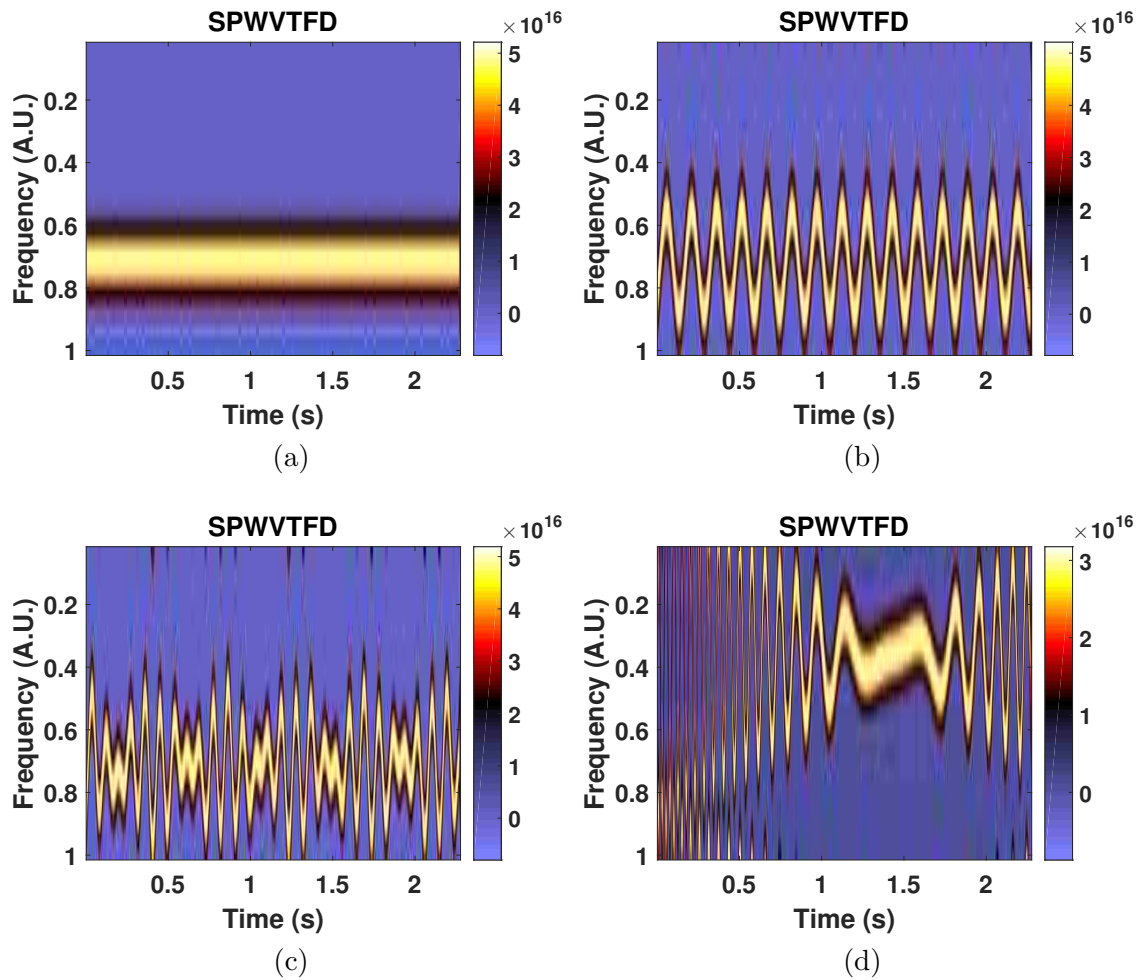


Figure E.2: SPWVTFD applied to slow-time signals with different vibration modulation. (a) Static object. (b) Mono-component sinusoidal vibration. (c) Multi-component sinusoidal vibration. (d) Chirped vibration.

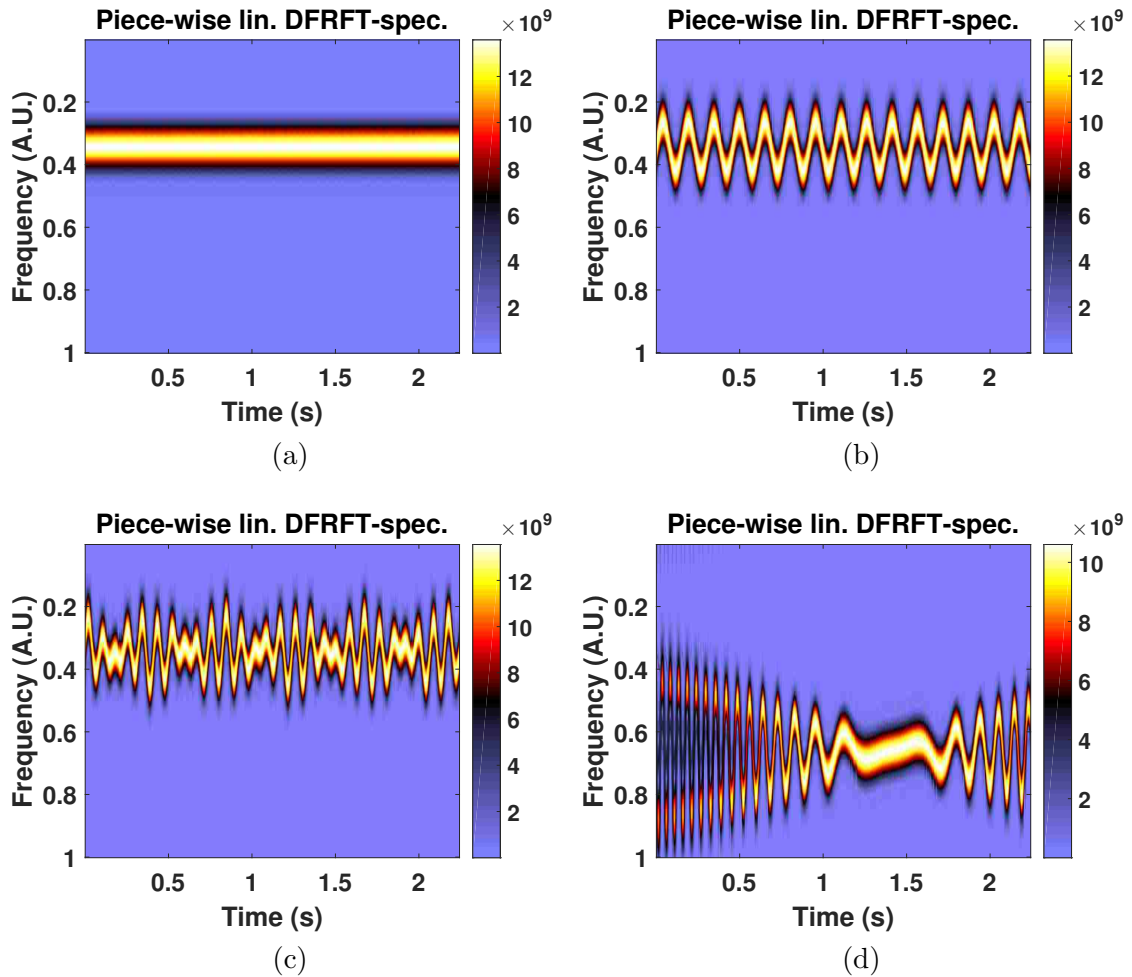


Figure E.3: Piece-wise linear DFRFT-based spectrogram applied to slow-time signals with different vibration modulation. (a) Static object. (b) Mono-component sinusoidal vibration. (c) Multi-component sinusoidal vibration. (d) Chirped vibration.

Appendix F

Statistical analysis of clutter-noise in SAR images

In this dissertation, it is assumed that clutter-noise term $W[n]$ in the probabilistic models (3.1) and (4.1) is zero-mean, circularly-symmetric complex normal, independent and identically distributed for $0 \leq n \leq N - 1$. This assumption is supported by the following analysis. Figure F.1 shows a SAR image acquired with Lynx-SAR system in a vibrometry experiment and its respective range-compressed phase history data. Four points of analysis were chosen at the cross-range points 250, 750, 1250 and 1750. Then, a normalized histogram was computed using the range data along each one of these four selected points. These histograms are shown in Fig. F.2. As can be observed, in the totality of the presented cases the histograms have a normal shape, the center value is zero and the spread (variance) is the same. In fact, the kurtosis of the analyzed data varies from 2.6 to 3.2 and its skewness from -0.05 to 0.08. Since the kurtosis of a standard gaussian distribution is 3 and its skewness is zero, the results suggest that the data is normal distributed. Furthermore, as shown in Fig. F.3, the distribution of the real part and the imaginary part of the samples in the complex plane is circularly symmetric. Finally, the independence assumption

Appendix F. Statistical analysis of clutter-noise in SAR images

can be proven in a similar fashion by showing that the joint PDF of $W[n]$ and $W[m]$ (i.e., joint histogram) is the product of their marginal PDFs (simple histograms), $\forall 0 \leq n \neq m \leq N - 1$.

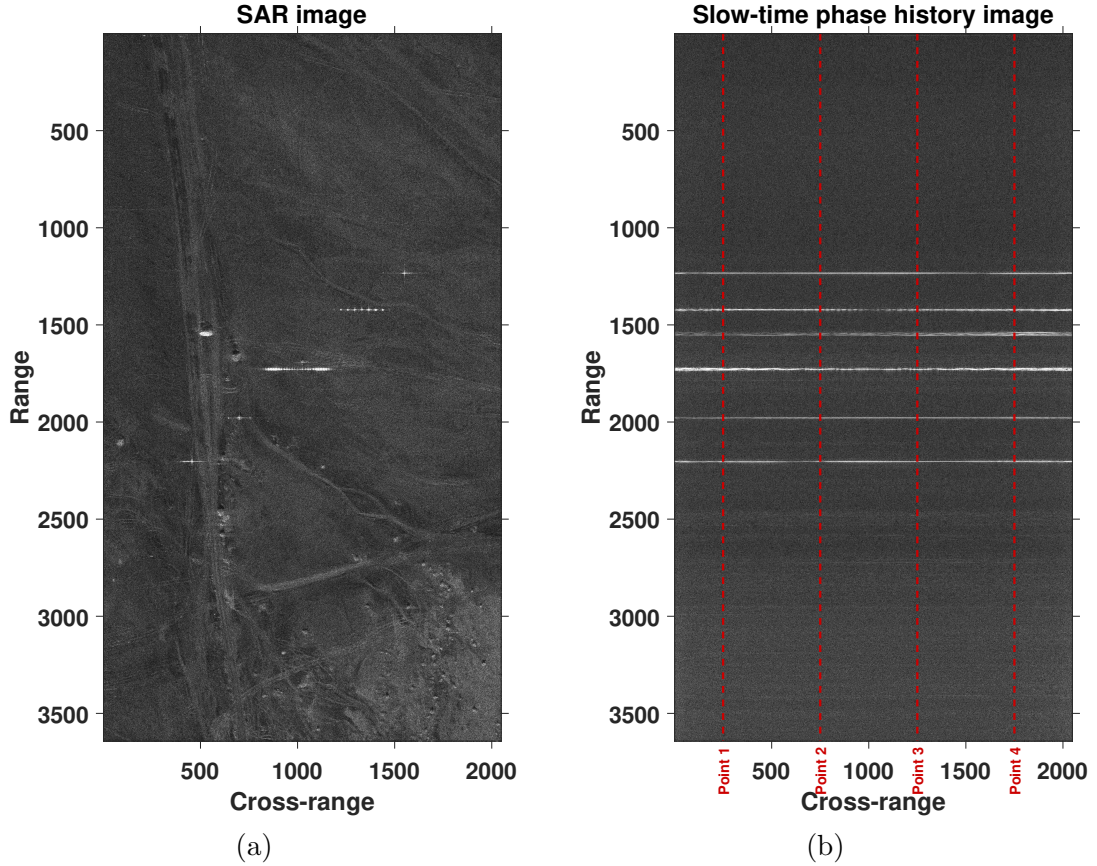


Figure F.1: SAR image used for clutter-noise characterization (a) and its respective range-compressed phase-history data (b). In (b) the four analysis points at the cross-range values 250, 750, 1250 and 1750 and the corresponding lines of range data used for computing the histograms are highlighted in red color.

Appendix F. Statistical analysis of clutter-noise in SAR images

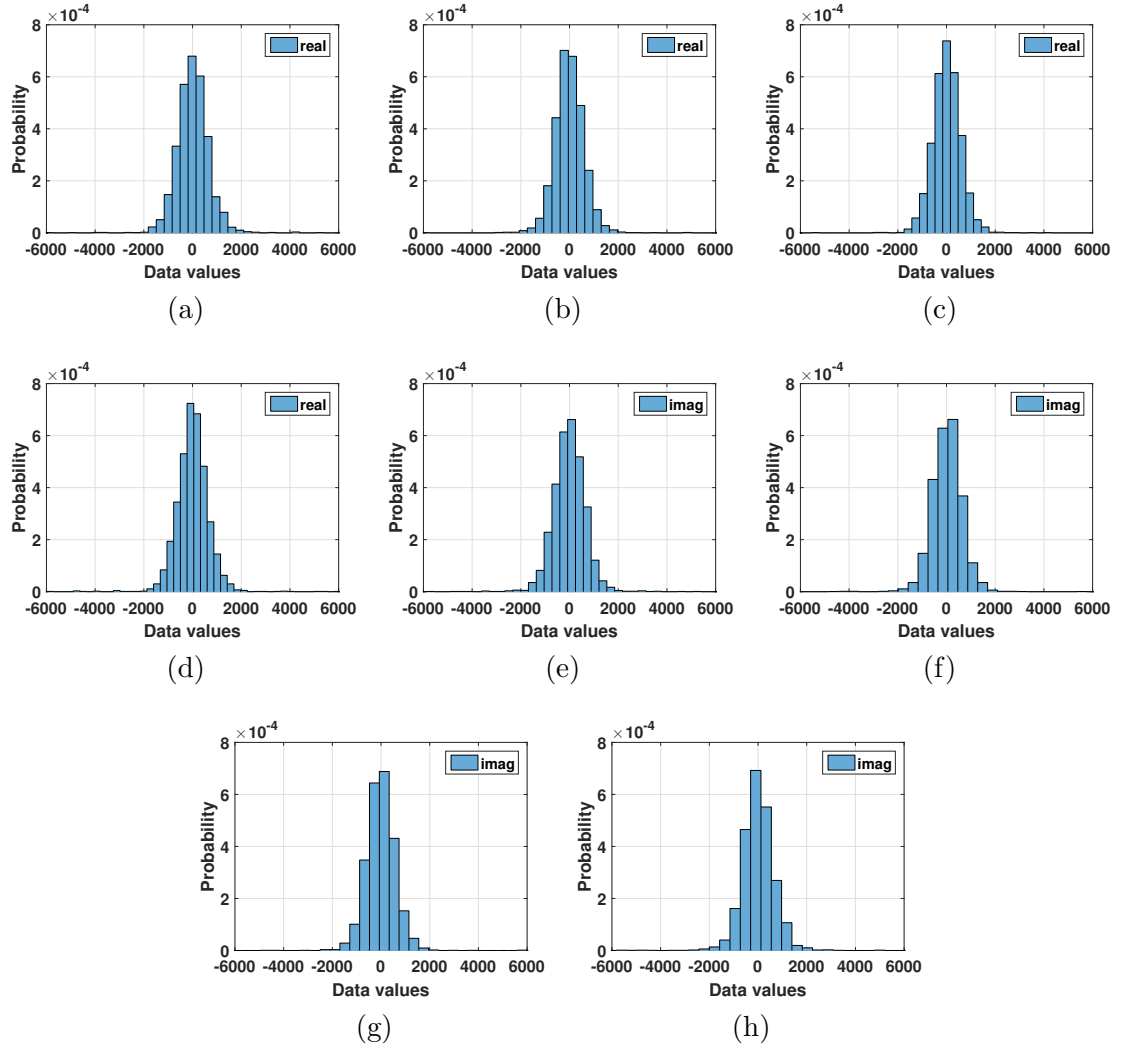


Figure F.2: Analysis of the clutter-noise signal using histograms. (a,b,c,d) Histogram of the real part of the range slices at the cross-range points 250, 750, 1250 and 1750, respectively. (e,f,g,h) Histogram of the imaginary part of the range slices at the cross-range points 250, 750, 1250 and 1750, respectively.

Appendix F. Statistical analysis of clutter-noise in SAR images

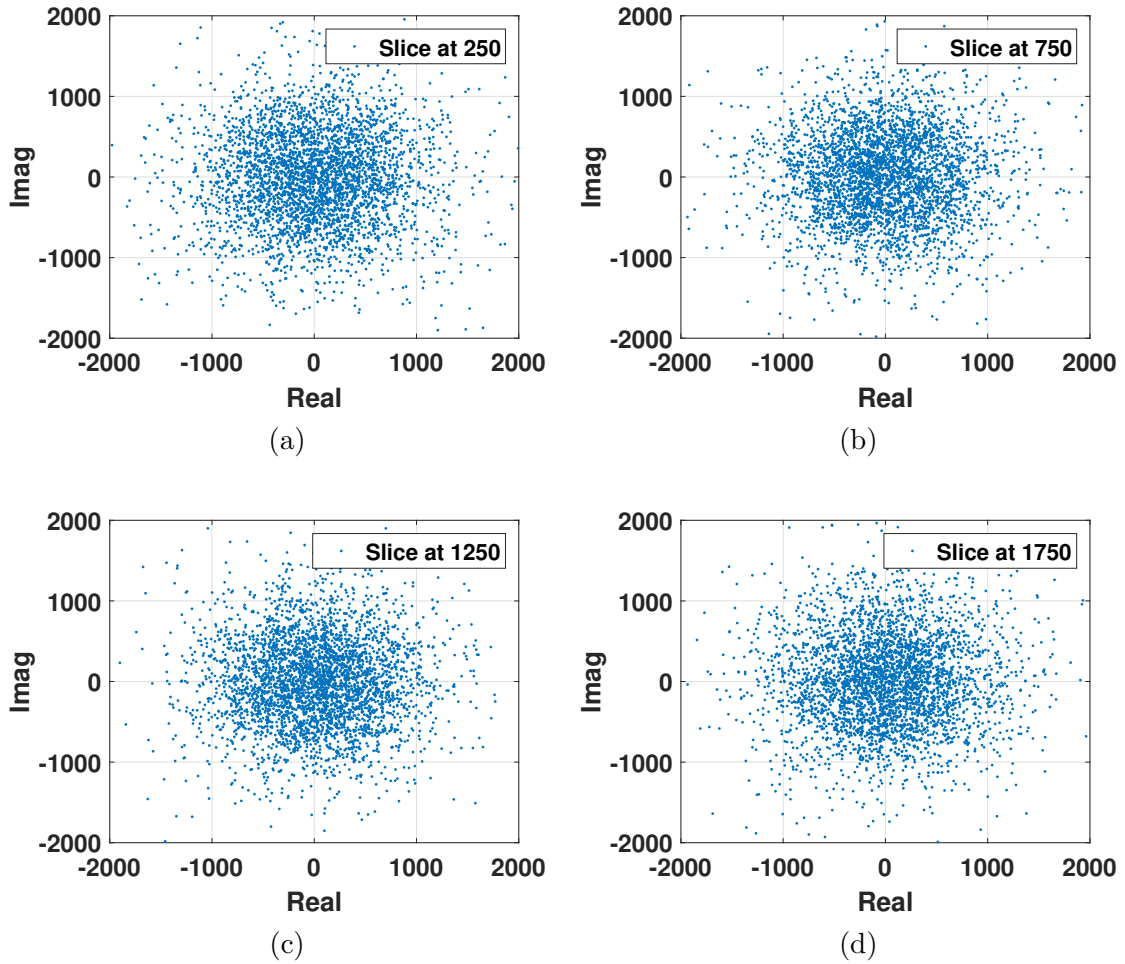


Figure F.3: Distribution of the real part of the clutter-noise signal vs its imaginary part in the complex plane (a,b,c,d) Range slices at the cross-range points 250, 750, 1250 and 1750, respectively.

Appendix G

Probability density functions of the direct binary-detection approach

In order to compute the probability density functions of the direct binary-detection approach, the following reduction is introduced. Let $s[n] = c_n \exp(j\beta_n)$ be the complex value of the n -th sample of the slow-time signal in Euler's notation. Then, under H_0 it can be obtained that

$$\begin{aligned} |s[n] - s_0[n]|^2 &= |s[n] - \sigma \exp(jf_y y n + j\phi)|^2 \\ &= c_n^2 + \sigma^2 - 2c_n \sigma \cos(\phi + f_y y n - \beta_n), \end{aligned} \tag{G.1}$$

and under H_1 ,

$$\begin{aligned} |s[n] - s_1[n]|^2 &= |s[n] - \sigma \exp(jf_y y n + j\phi + ja \cos(\phi_x + 2\pi n f))|^2 \\ &= c_n^2 + \sigma^2 - 2c_n \sigma \cos(\phi + f_y y n + a \cos(\phi_x + 2\pi n f) - \beta_n). \end{aligned} \tag{G.2}$$

Appendix G. Probability density functions of the direct binary-detection approach

Now, integrating over the marginalized random variables in (3.2):

$$\begin{aligned}
f_{\mathbf{s}}(\mathbf{s})|_{H_0} &= f_{\mathbf{s}}(s[0], s[1], \dots, s[N-1])|_{H_0} = \int_{\Sigma, \Phi, Y} f_{\mathbf{s}|\Sigma, \Phi, Y}(\mathbf{s}|\sigma, \phi, y)|_{H_0} \\
&= \left(\frac{1}{\pi\sigma_w^2}\right)^N \int_{\Sigma, \Phi, Y} \exp\left(-\sum_{n=0}^{N-1} \frac{|s[n] - s_0[n]|^2}{\sigma_w^2}\right) \\
&= \left(\frac{1}{\pi\sigma_w^2}\right)^N \int_{\Sigma, \Phi, Y} \exp\left(-\frac{\sum_{n=0}^{N-1} c_n^2}{\sigma_w^2} - \frac{\sum_{n=0}^{N-1} \sigma^2 - 2c_n\sigma \cos(\phi + f_y y n - \beta_n)}{\sigma_w^2}\right) \\
&= \left(\frac{1}{\pi\sigma_w^2}\right)^N \exp\left(-\frac{\sum_{n=0}^{N-1} c_n^2}{\sigma_w^2}\right) \cdot I_1,
\end{aligned} \tag{G.3}$$

where

$$I_1 = \int_{\Sigma, \Phi, Y} \exp\left(-\frac{\sum_{n=0}^{N-1} \sigma^2 - 2c_n\sigma \cos(\phi + f_y y n - \beta_n)}{\sigma_w^2}\right). \tag{G.4}$$

In I_1 the integration with respect to Σ is the only one that produces a closed-form expression. The integration with respect to Φ and Y must be carried out numerically no matter if it is done before or after the integral with respect to Σ . The integral of I_1 with respect to Σ is of the form

$$I = \frac{1}{b-a} \int_a^b \exp\left(\frac{Nx^2 - xd}{c}\right) dx, \tag{G.5}$$

with $a = \sigma_{min}$, $b = \sigma_{max}$, $c = -\sigma_w^2$ and $d = 2\sum_{n=0}^{N-1} c_n \cos(\phi + f_y y n - \beta_n)$. The solution of this integral is given by

$$I = \frac{\sqrt{\pi} \exp(-d^2/(4cN))}{2\sqrt{-N/c}} \left(\operatorname{erf}\left(\frac{2bN - d}{2N} \sqrt{-N/c}\right) - \operatorname{erf}\left(\frac{2aN - d}{2N} \sqrt{-N/c}\right) \right), \tag{G.6}$$

and

$$\operatorname{erf}(x) = \frac{2}{\sqrt{\pi}} \int_0^x \exp(-t^2) dt. \tag{G.7}$$

After computing the integral with respect to Σ , the integrand of I_1 is a function of ϕ and y . This function is redefined as $G_0(y, \phi; c_0, \dots, c_{N-1}, \beta_0, \dots, \beta_{N-1}) = G_0(y, \phi; \mathbf{s})$,

Appendix G. Probability density functions of the direct binary-detection approach

and the PDF of \mathbf{S} under the hypothesis H_0 can be written as

$$f_{\mathbf{S}}(\mathbf{s})|_{H_0} = \left(\frac{1}{\pi\sigma_w^2} \right)^N \exp \left(- \frac{\sum_{n=0}^{N-1} c_n^2}{\sigma_w^2} \right) \int_{\Phi, Y} G_0(y, \phi; \mathbf{s}). \quad (\text{G.8})$$

Let

$$K_0(y; \mathbf{s}) = \int_{\Phi} G_0(y, \phi; \mathbf{s}) = \frac{1}{2\pi} \int_{-\pi}^{\pi} G_0(y, \phi; \mathbf{s}) d\phi, \quad (\text{G.9})$$

and

$$L_0(\mathbf{s}) = \int_Y K_0(y; \mathbf{s}) = \frac{1}{2y_o} \int_{-y_o}^{y_o} K_0(y; \mathbf{s}) dy. \quad (\text{G.10})$$

Then, the PDF for the hypothesis H_0 (static object) can be stated as

$$f_{\mathbf{S}}(\mathbf{s})|_{H_0} = \left(\frac{1}{\pi\sigma_w^2} \right)^N \exp \left(- \frac{\sum_{n=0}^{N-1} c_n^2}{\sigma_w^2} \right) L_0(\mathbf{s}) \quad (\text{G.11})$$

where $\mathbf{s} = [s[0], \dots, s[N-1]]^T$ and $s[n] = c_n \exp(j\beta_n)$ for $n = 0, \dots, N-1$. The procedure to determine $f_{\mathbf{S}}|_{H_1}$ is similar to the previous one, with the only exception that there are 3 extra random variables that model the vibration of the object.

$$\begin{aligned} f_{\mathbf{S}}(\mathbf{s})|_{H_1} &= f_{\mathbf{S}}(s[0], s[1], \dots, s[N-1])|_{H_1} \\ &= \int_{\Sigma, \Phi, Y, A, F, \Phi_x} f_{\mathbf{S}|\Sigma, \Phi, Y, A, F, \Phi_x}(\mathbf{s}|\sigma, \phi, y, a, f, \phi_x)|_{H_1} \\ &= \left(\frac{1}{\pi\sigma_w^2} \right)^N \int_{\Sigma, \Phi, Y, A, F, \Phi_x} \exp \left(- \sum_{n=0}^{N-1} \frac{|s[n] - s_1[n]|^2}{\sigma_w^2} \right) \\ &= \left(\frac{1}{\pi\sigma_w^2} \right)^N \int_{\Sigma, \Phi, Y, A, F, \Phi_x} \exp \left(- \frac{\sum_{n=0}^{N-1} c_n^2}{\sigma_w^2} \right. \\ &\quad \left. - \frac{\sum_{n=0}^{N-1} \sigma^2 - 2c_n \sigma \cos(\phi + f_y y n + a \cos(\phi_x + 2\pi n f) - \beta_n)}{\sigma_w^2} \right) \\ &= \left(\frac{1}{\pi\sigma_w^2} \right)^N \exp \left(- \frac{\sum_{n=0}^{N-1} c_n^2}{\sigma_w^2} \right) \cdot I_2, \end{aligned} \quad (\text{G.12})$$

where

$$I_2 = \int_{\Sigma, \Phi, Y, A, F, \Phi_x} \exp \left(- \frac{\sum_{n=0}^{N-1} \sigma^2 - 2c_n \sigma \cos(\phi + f_y y n + a \cos(\phi_x + 2\pi n f) - \beta_n)}{\sigma_w^2} \right). \quad (\text{G.13})$$

Appendix G. Probability density functions of the direct binary-detection approach

Similar to the previous case, the integral with respect to Σ is of the form of (G.5), with solution given by (G.6) and with $a = \sigma_{min}$, $b = \sigma_{max}$, $c = -\sigma_w^2$ and $d = 2 \sum_{n=0}^{N-1} c_n \cos(\phi + f_y y n + a \cos(\phi_x + 2\pi n f) - \beta_n)$. After computing the integral with respect to Σ , the integrand of I_2 is a function of ϕ , y , a , f , and ϕ_x . Let this function be denoted as $G_1(y, \phi, a, f, \phi_x; c_0, \dots, c_{N-1}, \beta_0, \dots, \beta_{N-1}) = G_0(y, \phi, a, f, \phi_x; \mathbf{s})$, then the PDF of \mathbf{S} under H_1 can be written as

$$f_{\mathbf{s}}(\mathbf{s})|_{H_1} = \left(\frac{1}{\pi\sigma_w^2}\right)^N \exp\left(-\frac{\sum_{n=0}^{N-1} c_n^2}{\sigma_w^2}\right) \int_{\Phi, Y, A, F, \Phi_x} G_1(y, \phi, a, f, \phi_x; \mathbf{s}). \quad (\text{G.14})$$

Next, consider the following definitions for ease of notation.

$$K_1(y, a, f, \phi_x; \mathbf{s}) = \int_{\Phi} G_1(y, \phi, a, f, \phi_x; \mathbf{s}) = \frac{1}{2\pi} \int_{-\pi}^{\pi} G_1(y, \phi, a, f, \phi_x; \mathbf{s}) d\phi \quad (\text{G.15})$$

$$L_1(a, f, \phi_x; \mathbf{s}) = \int_Y K_1(y, a, f, \phi_x; \mathbf{s}) = \frac{1}{2y_o} \int_{-y_o}^{y_o} K_1(y, a, f, \phi_x; \mathbf{s}) dy \quad (\text{G.16})$$

$$P_1(f, \phi_x; \mathbf{s}) = \int_A L_1(a, f, \phi_x; \mathbf{s}) = \frac{1}{a_{max} - a_{min}} \int_{a_{min}}^{a_{max}} L_1(a, f, \phi_x; \mathbf{s}) da \quad (\text{G.17})$$

$$Q_1(\phi_x; \mathbf{s}) = \int_F P_1(f, \phi_x; \mathbf{s}) = \frac{1}{f_{max} - f_{min}} \int_{f_{min}}^{f_{max}} P_1(f, \phi_x; \mathbf{s}) df \quad (\text{G.18})$$

$$R_1(\mathbf{s}) = \int_{\Phi_x} Q_1(\phi_x; \mathbf{s}) = \frac{1}{2\pi} \int_{-\pi}^{\pi} Q_1(\phi_x; \mathbf{s}) d\phi_x \quad (\text{G.19})$$

Then, the probability density function for hypothesis H_1 (vibrating object) can be stated as

$$f_{\mathbf{s}}(\mathbf{s})|_{H_1} = \left(\frac{1}{\pi\sigma_w^2}\right)^N \exp\left(-\frac{\sum_{n=0}^{N-1} c_n^2}{\sigma_w^2}\right) R_1(\mathbf{s}) \quad (\text{G.20})$$

where $\mathbf{s} = [s[0], \dots, s[N-1]]^T$ and $s[n] = c_n \exp(j\beta_n)$ for $n = 0, \dots, N-1$.

Appendix H

Covariance matrices for the binary probabilistic detector

Recall that the hypothesis testing problem can be written in vector form as in (2.8). Under hypothesis H_0 the slow-time vector $\mathbf{S} = \mathbf{S}_0 + \mathbf{W}$. Thus, the mean value (expected value) of \mathbf{S} is given by

$$\begin{aligned} E\{\mathbf{S}\} &= E\{[S[0], \dots, S[N-1]]^T\} = [E\{S[0]\}, \dots, E\{S[N-1]\}]^T \\ &= [E\{S_0[0]\}, \dots, E\{S_0[N-1]\}]^T, \end{aligned} \quad (\text{H.1})$$

where

$$E\{S_0[n]\} = \int_{\Sigma, \Phi, Y} \sigma \exp(jf_y n + j\phi) f_{\Sigma, \Phi, Y}(\sigma, \phi, y) d(\sigma, \phi, y), \quad 0 \leq n \leq N-1. \quad (\text{H.2})$$

Since Σ , Φ and Y are independent random variables with uniform distributions, then

$$E\{S_0[n]\} = \frac{1}{\sigma_{max} - \sigma_{min}} \frac{1}{2y_o} \frac{1}{2\pi} \int_{-y_o}^{y_o} \int_{\sigma_{min}}^{\sigma_{max}} \int_{-\pi}^{\pi} \sigma \exp(jf_y n + j\phi) d\phi d\sigma d_y. \quad (\text{H.3})$$

Note that the integral is zero because

$$\int_{-\pi}^{\pi} \sigma \exp(jf_y n + j\phi) d\phi = 0, \quad (\text{H.4})$$

Appendix H. Covariance matrices for the binary probabilistic detector

then, $E\{S_0[n]\} = 0$, $0 \leq n \leq N - 1$, and therefore

$$E\{\mathbf{S}\} = \mathbf{0}_{N \times 1}. \quad (\text{H.5})$$

Since \mathbf{S} is zero-mean, the auto-covariance of \mathbf{S} is given by

$$\mathbf{cov}\{\mathbf{S}\} = E\{\mathbf{S}\mathbf{S}^*\}, \quad (\text{H.6})$$

where the symbol “*” represents the conjugate transpose.

$$\begin{aligned} \mathbf{cov}\{\mathbf{S}\} &= E\{(\mathbf{S}_0 + \mathbf{W})(\mathbf{S}_0 + \mathbf{W})^*\}, \\ &= E\{\mathbf{S}_0\mathbf{S}_0^*\} + E\{\mathbf{S}_0\mathbf{W}^*\} + E\{\mathbf{W}\mathbf{S}_0^*\} + E\{\mathbf{W}\mathbf{W}^*\}, \\ &= E\{\mathbf{S}_0\mathbf{S}_0^*\} + E\{\mathbf{W}\mathbf{W}^*\}, \end{aligned} \quad (\text{H.7})$$

because $E\{\mathbf{W}\} = \mathbf{0}_{N \times 1}$, and \mathbf{S}_0 and \mathbf{W} are independent. The value for the entry in the n -th position of the diagonal of the covariance matrix $\mathbf{cov}\{\mathbf{S}\}$ is given by

$$\mathbf{cov}\{S[n], S[n]\} = E\{S_0[n]S_0^*[n]\} + E\{W[n]W^*[n]\} = E\{|S_0[n]|^2\} + E\{|W[n]|^2\}, \quad (\text{H.8})$$

where $E\{|W[n]|^2\} = \sigma_w^2$ and

$$\begin{aligned} E\{|S_0[n]|^2\} &= E\{|\Sigma \exp(jf_y Y n + j\Phi)|^2\} = E\{|\Sigma|^2 |\exp(jf_y Y n + j\Phi)|^2\} \\ &= E\{|\Sigma|^2\} \end{aligned} \quad (\text{H.9})$$

$$\begin{aligned} E\{|\Sigma|^2\} &= \frac{1}{\sigma_{max} - \sigma_{min}} \int_{\sigma_{min}}^{\sigma_{max}} \sigma^2 d\sigma \\ &= \frac{1}{3} (\sigma_{max}^2 + \sigma_{max}\sigma_{min} + \sigma_{min}^2) \\ &=: \frac{1}{3} k_\sigma \end{aligned} \quad (\text{H.10})$$

Hence, $\mathbf{cov}\{S[n], S[n]\} = \frac{1}{3} k_\sigma + \sigma_w^2$. The value for off-diagonal entries of $\mathbf{cov}\{\mathbf{S}\}$ are given by

$$\mathbf{cov}\{S[n], S[k]\} = E\{S_0[n]S_0^*[k]\} + E\{W[n]W^*[k]\} = E\{S_0[n]S_0^*[k]\}, \quad (\text{H.11})$$

Appendix H. Covariance matrices for the binary probabilistic detector

because the clutter-noise samples are assumed to be independent.

$$\begin{aligned}
\mathbf{cov}\{S[n], S[k]\} &= E\{S_0[n]S_0^*[k]\} \\
&= E\{(\Sigma \exp(jf_y Y n + j\Phi))(\Sigma \exp(jf_y Y k + j\Phi))^*\} \quad (\text{H.12}) \\
&= E\{|\Sigma|^2\}E\{\exp(jf_y Y(n-k))\},
\end{aligned}$$

because the random variables Σ , Φ and Y are independent. Since

$$E\{\exp(jf_y Y(n-k))\} = \frac{1}{2y_o} \int_{-y_o}^{y_o} \exp(jf_y y(n-k)) dy = \frac{\sin(y_o f_y(n-k))}{y_o f_y(n-k)}, \quad (\text{H.13})$$

then

$$\mathbf{cov}\{S[n], S[k]\} = \frac{1}{3}k_\sigma \text{sinc}(y_o f_y(n-k)), \quad \forall n \neq k. \quad (\text{H.14})$$

Finally, the (n, k) th entry of the $N \times N$ covariance matrix of \mathbf{S} under H_0 is

$$\mathbf{cov}\{S[n], S[k]\} = \begin{cases} \frac{1}{3}k_\sigma + \sigma_w^2, & 0 \leq n = k \leq N-1 \\ \frac{1}{3}k_\sigma \text{sinc}(y_o f_y(n-k)), & \forall n \neq k. \end{cases} \quad (\text{H.15})$$

Under hypothesis H_1 the slow-time vector $\mathbf{S} = \mathbf{S}_1 + \mathbf{W}$. Proceeding in the same fashion as before, it is possible to obtain that

$$E\{S_1[n]\} = 0, \quad 0 \leq n \leq N-1. \quad (\text{H.16})$$

Therefore,

$$E\{\mathbf{S}\} = \mathbf{0}_{N \times 1}. \quad (\text{H.17})$$

Then, because \mathbf{S} is zero-mean, the covariance matrix of \mathbf{S} under H_1 is given by

$$\begin{aligned}
\mathbf{cov}\{\mathbf{S}\} &= E\{\mathbf{S}\mathbf{S}^*\} \\
&= E\{(\mathbf{S}_1 + \mathbf{W})(\mathbf{S}_1 + \mathbf{W})^*\} \\
&= E\{\mathbf{S}_1\mathbf{S}_1^*\} + E\{\mathbf{S}_1\mathbf{W}^*\} + E\{\mathbf{W}\mathbf{S}_1^*\} + E\{\mathbf{W}\mathbf{W}^*\} \\
&= E\{\mathbf{S}_1\mathbf{S}_1^*\} + E\{\mathbf{W}\mathbf{W}^*\},
\end{aligned} \quad (\text{H.18})$$

Appendix H. Covariance matrices for the binary probabilistic detector

because $E\{\mathbf{W}\} = \mathbf{0}_{N \times 1}$ and \mathbf{W} and \mathbf{S}_1 are independent. The value for the entry in the n -th position of the diagonal of $\mathbf{cov}\{\mathbf{S}\}$ is given by

$$\begin{aligned} \mathbf{cov}\{S[n], S[n]\} &= E\{S_1[n]S_1^*[n]\} + E\{W[n]W^*[n]\} \\ &= E\{|S_1[n]|^2\} + E\{|W[n]|^2\}, \end{aligned} \quad (\text{H.19})$$

where $E\{|W[n]|^2\} = \sigma_w^2$ and

$$\begin{aligned} E\{|S_1[n]|^2\} &= E\{|\Sigma \exp(jf_y Y n + j\Phi + jA \cos(\Phi_x + 2\pi n F))|^2\} \\ &= E\{|\Sigma|^2 \exp(jf_y Y n + j\Phi + jA \cos(\Phi_x + 2\pi n F))|^2\} \\ &= E\{|\Sigma|^2\} \\ &= \frac{1}{3}k_\sigma. \end{aligned} \quad (\text{H.20})$$

Hence, $\mathbf{cov}\{S[n], S[n]\} = \frac{1}{3}k_\sigma + \sigma_w^2$. The value for off-diagonal entries of $\mathbf{cov}\{\mathbf{S}\}$ are given by

$$\mathbf{cov}\{S[n], S[k]\} = E\{S_1[n]S_1^*[k]\} + E\{W[n]W^*[k]\} = E\{S_1[n]S_1^*[k]\}, \quad (\text{H.21})$$

because the clutter-noise samples are assumed to be independent.

$$\begin{aligned} \mathbf{cov}\{S[n], S[k]\} &= E\{S_1[n]S_1^*[k]\} \\ &= E\{(\Sigma \exp(jf_y Y n + j\Phi + jA \cos(\Phi_x + 2\pi n F))) \\ &\quad (\Sigma \exp(jf_y Y k + j\Phi + jA \cos(\Phi_x + 2\pi k F)))^*\} \\ &= E\{|\Sigma|^2\} \cdot E\{\exp(jf_y Y(n-k))\} \\ &\quad E\{\exp(jA(\cos(\Phi_x + 2\pi n F) - \cos(\Phi_x + 2\pi k F)))\}, \end{aligned} \quad (\text{H.22})$$

because all the involved random variables are independent. The expected value $g_{A,F,\Phi_x} = E\{\exp(jA(\cos(\Phi_x + 2\pi n F) - \cos(\Phi_x + 2\pi k F)))\}$ does not have a closed-form solution and it has to be carried out by numerical integration. Since

$$E\{|\Sigma|^2\}E\{\exp(jf_y Y(n-k))\} = \frac{1}{3}k_\sigma \text{sinc}(y_o f_y(n-k)), \quad \forall n \neq k, \quad (\text{H.23})$$

the (n, k) th entry of the $N \times N$ covariance matrix of \mathbf{S} under H_1 is given by

$$\mathbf{cov}\{S[n], S[k]\} = \begin{cases} \frac{1}{3}k_\sigma + \sigma_w^2, & 0 \leq n = k \leq N - 1 \\ \frac{1}{3}k_\sigma \text{sinc}(y_o f_y(n-k))g_{A,F,\Phi_x}, & \forall n \neq k. \end{cases} \quad (\text{H.24})$$

Appendix H. Covariance matrices for the binary probabilistic detector

Note:

(1) Both resulting covariance matrices under hypothesis H_0 (H.15) and H_1 (H.24) are real-valued.

(2) A similar procedure can be followed to show that the pseudo-covariance matrix of \mathbf{S} under both hypothesis, H_0 and H_1 , is zero, i.e., $E_{H_j}\{\mathbf{S}\mathbf{S}^T\} = \mathbf{0}_{N \times N}$, $j = 0, 1$.

Appendix I

Karhunen-Loève transform

The KL expansion, also known as KLT in finite dimensional spaces, provides a mechanism for converting a discrete-time random process (i.e., random vector) into an equivalent sequence with diagonal autocovariance matrix. This is, the samples of the equivalent sequence are statistically independent among them. Specifically, the KL expansion of a random vector is carried out by projecting it onto the eigenvectors of its autocovariance matrix. Given a zero-mean random vector $\mathbf{S} = [S[0], \dots, S[N-1]]^T$, with $N \times N$ autocovariance matrix $\mathbf{cov}\{\mathbf{S}\}$, the spectral decomposition of its autocovariance matrix is given by

$$\mathbf{cov}\{\mathbf{S}\} = \sum_{k=0}^{N-1} \lambda_k \mathbf{v}_k \mathbf{v}_k^*, \quad (\text{I.1})$$

where $\{\lambda_k\}_{k=0}^{N-1}$ and $\{\mathbf{v}_k\}_{k=0}^{N-1}$ are the eigenvalues and the orthonormal eigenvectors of $\mathbf{cov}\{\mathbf{S}\}$, respectively. The KL expansion of \mathbf{S} [33] (pp. 274-277) is defined as

$$\mathbf{S} = \sum_{k=0}^{N-1} Z_k \mathbf{v}_k, \quad (\text{I.2})$$

where the KL coefficients are

$$Z_k = \mathbf{v}_k^* \mathbf{S}, \quad 0 \leq k \leq N-1. \quad (\text{I.3})$$

Appendix I. Karhunen-Loève transform

The KL expansion provides for a separation of the randomness and the time-variation characteristic of the discrete-time random process $\mathbf{S} = [S[0], \dots, S[N-1]]^T$. In particular, the randomness in \mathbf{S} is summarized in the sequence $\mathbf{Z} = \{Z_k\}_{k=0}^{N-1}$ while the time variation in the process is captured in the sequence of eigenvectors $\{\mathbf{v}_k\}_{k=0}^{N-1}$. In this way, the expansion (I.2) combines these two properties to represent the process. Since $\{Z_k\}_{k=0}^{N-1}$ is determined from \mathbf{S} via (I.3) and \mathbf{S} is determined from $\{Z_k\}_{k=0}^{N-1}$ via (I.2), the sequence \mathbf{Z} is an equivalent observation of the discrete-time process \mathbf{S} . Also, note that

$$E\{Z_k\} = E\{\mathbf{v}_k^* \mathbf{S}\} = \mathbf{v}_k^* E\{\mathbf{S}\} = 0, \quad (\text{I.4})$$

and

$$\begin{aligned} \mathbf{cov}\{Z_k, Z_m\} &= E\{Z_k Z_m^*\} = E\{\mathbf{v}_k^* \mathbf{S} \times (\mathbf{v}_m^* \mathbf{S})^*\} \\ \mathbf{cov}\{Z_k, Z_m\} &= E\{\mathbf{v}_k^* \mathbf{S} \mathbf{S}^* \mathbf{v}_m\} = \mathbf{v}_k^* \mathbf{cov}\{\mathbf{S}\} \mathbf{v}_m. \end{aligned} \quad (\text{I.5})$$

Since $\mathbf{v}_k^* \mathbf{v}_m = \delta_{k,m}$ where $\delta_{k,m}$ is the Kronecker delta function and $\mathbf{cov}\{\mathbf{S}\}$ is given by (I.1), then

$$\mathbf{cov}\{Z_k, Z_m\} = \begin{cases} \lambda_k, & k = m \\ 0, & k \neq m. \end{cases} \quad (\text{I.6})$$

Hence, $\mathbf{cov}\{\mathbf{Z}\} = \text{diag}(\{\lambda_k\}_{k=0}^{N-1})$. Finally, since under both hypotheses H_0 and H_1 the covariance matrices are real, then eigenvectors $\{\mathbf{v}_k\}_{k=0}^{N-1}$ are real. Furthermore, since $E\{Z_k, Z_m\} = 0$, the KL coefficients are uncorrelated.

Appendix J

Covariance matrices of the M-ary detection problem

For the implementation of a M-ary vibration detection framework based on the KL expansion, it is important to compute the covariance matrix of the slow-time signal S under every hypothesis. This is because the KL transformation is based on the eigenvectors of such covariance matrices. The computation of such covariance matrices is divided into two steps, diagonal entries and off-diagonal entries. For simplicity of notation, consider that the slow-time vector \mathbf{S} consisting of N samples has the following form

$$S[n] = S_j[n] + W[n] = \Sigma \exp(jf_y Y n + j\Phi + jX_v[n]) + W[n], \quad (\text{J.1})$$

for $0 \leq j \leq 4$ and $0 \leq n \leq N - 1$, where $X_v[n]$ represents the corresponding vibration waveform for each hypothesis, being identically zero for H_0 .

Diagonal entries of the covariance matrix of \mathbf{S}

Under all hypothesis, the diagonal terms of the covariance matrix $\mathbf{cov}\{\mathbf{S}\}$ is given

Appendix J. Covariance matrices of the M-ary detection problem

by

$$\begin{aligned} E\{S[n]S^*[n]\} &= E\{(S_j[n] + W[n])(S_j[n] + W[n])^*\} \\ E\{S[n]S^*[n]\} &= E\{S_j[n]S_j^*[n]\} + E\{W[n]W^*[n]\} = E\{|S_j[n]|^2\} + E\{|W[n]|^2\}, \end{aligned} \quad (\text{J.2})$$

because $S_j[n]$ and clutter-noise are zero-mean and independent. Since

$$E\{|S_j[n]|^2\} = E\{|\Sigma|^2 \exp(jf_y Y n + j\Phi + jX_v[n])|^2\} = E\{|\Sigma|^2\} \quad (\text{J.3})$$

and

$$E\{|\Sigma|^2\} = \frac{1}{\sigma_{max} - \sigma_{min}} \int_{\sigma_{min}}^{\sigma_{max}} \sigma^2 d\sigma = \frac{1}{3}k_\sigma, \quad (\text{J.4})$$

then $E\{S[n]S^*[n]\} = \frac{1}{3}k_\sigma + \sigma_w^2$, for all hypothesis H_j , $0 \leq j \leq 4$.

Off-diagonal entries of the covariance matrix of \mathbf{S}

Since the involved random variables are independent, we have that

$$E\{S[n]S^*[m]\} = E\{(S_j[n] + W[n])(S_j[m] + W[m])^*\} = E\{S_j[n]S_j^*[m]\}, \quad (\text{J.5})$$

for $j \neq m$. because $S_j[n]$ and the clutter-noise are zero-mean and independent, and the noise samples are independent among them.

Case H_0 : Static object

$$\begin{aligned} E\{S_0[n]S_0^*[m]\} &= E\{(\Sigma \exp(jf_y Y n + j\Phi))(\Sigma \exp(jf_y Y n + j\Phi))^*\} \\ E\{S_0[n]S_0^*[m]\} &= E\{\Sigma^2 \exp(jf_y Y(n-m))\} = E\{\Sigma^2\}E\{\exp(jf_y Y(n-m))\}, \end{aligned} \quad (\text{J.6})$$

because the random variables Σ and Y are independent. Since

$$E\{\exp(jf_y Y(n-m))\} = \frac{1}{2y_o} \int_{-y_o}^{y_o} \exp(jf_y Y(n-m)) = \frac{\sin(y_o f_y(n-m))}{y_o f_y(n-m)} \quad (\text{J.7})$$

Appendix J. Covariance matrices of the M-ary detection problem

then

$$E\{S[n]S^*[m]\} = \frac{1}{3}k_\sigma \text{sinc}(y_o f_y(n-m)), \quad 1 \leq n \neq m \leq N \quad (\text{J.8})$$

Case H_1 : Vibrating object exhibiting a simple sinusoidal vibration

$$\begin{aligned} E\{S_1[n]S_1^*[m]\} &= \\ &= E\{(\Sigma \exp(jf_y Y n + j\Phi + jX_v[n]))(\Sigma \exp(jf_y Y n + j\Phi + jX_v[n]))^*\} \\ &= E\{\Sigma^2 \exp(jf_y Y(n-m)) \exp(jX_v[n] - jX_v[m])\} \quad (\text{J.9}) \\ &= E\{\Sigma^2\} E\{\exp(jf_y Y(n-m))\} E\{\exp(jA(\cos(\Phi_x + 2\pi F n) - \cos(\Phi_x + 2\pi F m)))\} \\ &= \frac{1}{3}k_\sigma \text{sinc}(y_o f_y(n-m)) g_{A, \Phi_x, F}(n, m), \quad 1 \leq n \neq m \leq N, \end{aligned}$$

where $g_{A, \Phi_x, F}(n, m) = E\{\exp(jA(\cos(\Phi_x + 2\pi F n) - \cos(\Phi_x + 2\pi F m)))\}$ must be computed via numerical integration. Then,

$$E\{S[n]S^*[m]\} = \frac{1}{3}k_\sigma \text{sinc}(y_o f_y(n-m)) g_{A, \Phi_x, F}(n, m), \quad 1 \leq n \neq m \leq N \quad (\text{J.10})$$

Case H_2 : Vibrating object exhibiting a multicomponent sinusoidal vibration

Proceeding in a similar fashion as in the previous case,

$$\begin{aligned} E\{S_2[n]S_2^*[m]\} &= \\ &= E\{(\Sigma \exp(jf_y Y n + j\Phi + jX_v[n]))(\Sigma \exp(jf_y Y n + j\Phi + jX_v[n]))^*\} \\ &= E\{\Sigma^2 \exp(jf_y Y(n-m)) \exp(jX_v[n] - jX_v[m])\} \quad (\text{J.11}) \\ &= E\{\Sigma^2\} E\{\exp(jf_y Y(n-m))\} E\{\exp(\sum_{k=1}^K jA_k(\cos(\Phi_x^k + 2\pi F_k n) - \cos(\Phi_x^k + 2\pi F_k m)))\} \\ &= \frac{1}{3}k_\sigma \text{sinc}(y_o f_y(n-m)) \prod_{k=1}^K g_{A_k, \Phi_x^k, F_k}(n, m), \quad 1 \leq n \neq m \leq N, \end{aligned}$$

Therefore,

$$E\{S[n]S^*[m]\} = \frac{1}{3}k_\sigma \text{sinc}(y_o f_y(n-m)) \prod_{k=1}^K g_{A_k, \Phi_x^k, F_k}(n, m), \quad 1 \leq n \neq m \leq N \quad (\text{J.12})$$

Appendix J. Covariance matrices of the M-ary detection problem

Case H_3 : Vibrating object exhibiting a chirp vibration

$$\begin{aligned}
& E\{S_3[n]S_3^*[m]\} = \\
& = E\left\{\left(\sum \exp(jf_y Y n + j\Phi + jX_v[n])\right)\left(\sum \exp(jf_y Y n + j\Phi + jX_v[n])\right)^*\right\} \\
& = E\left\{\sum^2 \exp(jf_y Y(n-m)) \exp(jX_v[n] - jX_v[m])\right\} \tag{J.13} \\
& = E\{\sum^2\} E\left\{\exp(jf_y Y(n-m))\right\} E\left\{\exp(jA(\cos(\Phi_x + 2\pi(F+C_r n)n) - \cos(\Phi_x + 2\pi(F+C_r m)m)))\right\} \\
& = \frac{1}{3}k_\sigma \text{sinc}(y_o f_y(n-m)) h_{A,\Phi_x,F,C_r}(n,m), \quad 1 \leq n \neq m \leq N,
\end{aligned}$$

where $h_{A,\Phi_x,F,C_r}(n,m) = E\left\{\exp(jA(\cos(\Phi_x + 2\pi(F+C_r n)n) - \cos(\Phi_x + 2\pi(F+C_r m)m)))\right\}$ must be computed via numerical integration. Then,

$$E\{S[n]S^*[m]\} = \frac{1}{3}k_\sigma \text{sinc}(y_o f_y(n-m)) h_{A,\Phi_x,F,C_r}(n,m), \quad 1 \leq n \neq m \leq N \tag{J.14}$$

Case H_4 : Vibrating object exhibiting a multicomponent chirp-sinusoidal vibration

By repeating the same procedure as in the case of H_2 and H_3 it can be obtained that the off-diagonal entries of the covariance matrix for the hypothesis H_4 are

$$\begin{aligned}
& E\{S[n]S^*[m]\} = \frac{1}{3}k_\sigma \text{sinc}(y_o f_y(n-m)) \prod_{i=1}^I g_{A_i,\Phi_x^i,F_i}(n,m) \prod_{l=1}^L h_{A_l,\Phi_x^l,F^l,C_r^l}(n,m), \\
& 0 \leq n \neq m \leq N-1.
\end{aligned} \tag{J.15}$$

In summary, the vibration-induced phase-modulation on the slow-time vector \mathbf{S} only affects the off-diagonal entries of the resulting covariance matrices. Furthermore, as the complexity of the vibration increases due to the addition of independent components, the resulting expression for the covariance matrix is modulated in amplitude by a function $g_{A,\Phi_x,F}(n,m)$ in the case of the addition of a sinusoidal component or by a function $h_{A,\Phi_x,F,C_r}(n,m)$ in the case of the addition of a chirp component. Under all hypothesis and for any type of vibration, the diagonal entries of the covariance matrix of the slow-time vector \mathbf{S} are identical with value $\frac{1}{3}k_\sigma + \sigma_w^2$.

Appendix J. Covariance matrices of the M-ary detection problem

Remarks

1. All the covariance matrices for H_j , $0 \leq j \leq 4$, are symmetric-toeplitz matrices. This symmetry can be exploited to save time while computing their entries via numerical integration. Also all these matrices are real since $g_{A,\Phi_x,F}(n, m)$ and $h_{A,\Phi_x,F,C_r}(n, m)$ are always real.
2. For H_j , $0 \leq j \leq 4$, the entries of the corresponding pseudo-covariance matrices of the complex random vector \mathbf{S} are defined by

$$\begin{aligned}
 E\{S[n]S[m]\} &= E\{\Sigma^2 \exp(2j\Phi_x) \exp(jf_y Y(n+m)) \exp(jX_v[n] + X_v[m])\} \\
 E\{S[n]S[m]\} &= E\{\exp(2j\Phi_x)\} E\{\Sigma^2 \exp(jf_y Y(n+m)) \exp(jX_v[n] + X_v[m])\} \\
 E\{S[n]S[m]\} &= 0, \forall \quad 0 \leq n, m \leq N-1, \text{ because } E\{\exp(2j\Phi_x)\} = 0, \\
 &\text{since } \Phi_x \sim U[-\pi, \pi].
 \end{aligned}$$

3. Since under all hypothesis H_j , $0 \leq j \leq 4$, the covariance matrices are real, finite and the corresponding pseudo-covariance matrices are all zero, then \mathbf{S} is always a proper complex random vector.

References

- [1] A. W. Doerry and F. M. Dickey, “Synthetic aperture radar,” *Opt. Photon. News*, vol. 15, no. 11, pp. 28–33, Nov 2004. [Online]. Available: <http://www.osa-opn.org/abstract.cfm?URI=opn-15-11-28>
- [2] S. I. Tsunoda, F. Pace, J. Stence, M. Woodring, W. H. Hensley, A. W. Doerry, and B. C. Walker, “Lynx: a high-resolution synthetic aperture radar,” in *Proc. SPIE*, vol. 3704, 1999, pp. 20–27. [Online]. Available: <http://dx.doi.org/10.1117/12.354602>
- [3] S. Chiu, “An analysis of radarsat2 sar-gmti performance for standard beam mode,” DTIC Document, Tech. Rep., 2000.
- [4] A. W. Doerry, “Basics of polar-format algorithm for processing synthetic aperture radar images,” *Sandia National Laboratories report SAND2012-3369, Unlimited Release*, 2012.
- [5] R. K. Raney, “Synthetic aperture imaging radar and moving targets,” *IEEE Transactions on Aerospace and Electronic Systems*, vol. AES-7, no. 3, pp. 499–505, May 1971.
- [6] T. Sparr and B. Krane, “Micro-doppler analysis of vibrating targets in sar,” *IEE Proceedings - Radar, Sonar and Navigation*, vol. 150, no. 4, pp. 277–83–, Aug 2003.
- [7] B. D. Rigling, “Image-quality focusing of rotating sar targets,” *IEEE Geoscience and Remote Sensing Letters*, vol. 5, no. 4, pp. 750–754, Oct 2008.
- [8] M. Ruegg, E. Meier, and D. Nuesch, “Constant motion, acceleration, vibration, and rotation of objects in sar data,” in *Proc. SPIE*, vol. 5980, 2005, pp. 598 005–598 005–12. [Online]. Available: <http://dx.doi.org/10.1117/12.626529>

References

- [9] —, “Vibration and rotation in millimeter-wave sar,” *IEEE Transactions on Geoscience and Remote Sensing*, vol. 45, no. 2, pp. 293–304, Feb 2007.
- [10] V. C. Chen, F. Li, S. S. Ho, and H. Wechsler, “Micro-doppler effect in radar: phenomenon, model, and simulation study,” *IEEE Transactions on Aerospace and Electronic Systems*, vol. 42, no. 1, pp. 2–21, Jan 2006.
- [11] X. Bai, M. Xing, F. Zhou, G. Lu, and Z. Bao, “Imaging of micromotion targets with rotating parts based on empirical-mode decomposition,” *IEEE Transactions on Geoscience and Remote Sensing*, vol. 46, no. 11, pp. 3514–3523, Nov 2008.
- [12] Q. Wang, M. Xing, G. Lu, and Z. Bao, “High-resolution three-dimensional radar imaging for rapidly spinning targets,” *IEEE Transactions on Geoscience and Remote Sensing*, vol. 46, no. 1, pp. 22–30, Jan 2008.
- [13] X. Li, B. Deng, Y. Qin, H. Wang, and Y. Li, “The influence of target micromotion on sar and gmti,” *IEEE Transactions on Geoscience and Remote Sensing*, vol. 49, no. 7, pp. 2738–2751, July 2011.
- [14] Q. Wang, M. Pepin, R. Dunkel, T. Atwood, A. W. Doerry, B. Santhanam, W. Gerstle, and M. M. Hayat, “Reduction of vibration-induced artifacts in synthetic-aperture-radar imagery using the fractional fourier transform,” in *2012 19th IEEE International Conference on Image Processing*, Sept 2012, pp. 2677–2680.
- [15] F. Pérez, J. B. Campbell, M. Jaramillo, R. Dunkel, T. Atwood, A. Doerry, W. H. Gerstle, B. Santhanam, and M. M. Hayat, “Exploiting synthetic aperture radar imagery for retrieving vibration signatures of concealed machinery,” in *Proc.SPIE*, vol. 9829, 2016, pp. 9829 – 9829 – 12. [Online]. Available: <https://doi.org/10.1117/12.2224148>
- [16] F. Pérez, B. Santhanam, R. Dunkel, and M. M. Hayat, “Clutter suppression via hankel rank reduction for dfrft-based vibrometry applied to sar,” *IEEE Geoscience and Remote Sensing Letters*, vol. 14, no. 11, pp. 2052–2056, Nov 2017.
- [17] Q. Wang, M. Pepin, R. J. Beach, R. Dunkel, T. Atwood, B. Santhanam, W. Gerstle, A. W. Doerry, and M. M. Hayat, “Sar-based vibration estimation using the discrete fractional fourier transform,” *IEEE Transactions on Geoscience and Remote Sensing*, vol. 50, no. 10, pp. 4145–4156, Oct 2012.

References

- [18] J. B. Campbell, F. Pérez, Q. Wang, B. Santhanam, R. Dunkel, A. W. Doerry, T. Atwood, and M. M. Hayat, “Remote vibration estimation using displaced-phase-center antenna sar for strong clutter environments,” *IEEE Transactions on Geoscience and Remote Sensing*, vol. 56, no. 5, pp. 2735–2747, May 2018.
- [19] N. S. Subotic, B. J. Thelen, and D. A. Carrara, “Cyclostationary signal models for the detection and characterization of vibrating objects in sar data,” in *Conference Record of Thirty-Second Asilomar Conference on Signals, Systems and Computers (Cat. No.98CH36284)*, vol. 2, Nov 1998, pp. 1304–1308 vol.2.
- [20] C. V. Jakowatz, D. E. Wahl, P. H. Eichel, D. C. Ghiglia, and P. A. Thompson, *Spotlight-mode Synthetic Aperture Radar: A Signal Processing Approach*. New York, NY: Springer Science+Business Media, 1996.
- [21] M. Soumekh, *Synthetic Aperture Radar Signal Processing with MATLAB Algorithms*. New York: Wiley, 1999.
- [22] I. G. Cumming and F. H. Wong, *Digital Processing of Synthetic Aperture Radar Data: Algorithms and Implementation*. Norwood, MA: Artech House, 2005.
- [23] Q. Wang, M. Pepin, B. Santhanam, T. Atwood, and M. M. Hayat, “Sar-based vibration retrieval using the fractional fourier transform in slow time,” in *Radar Sensor Technology XIV*, ser. Proc. SPIE, K. I. Ranney and A. W. Doerry, Eds., vol. 7669, 2010, doi: 10.1117/12.849671.
- [24] M. Rüegg, E. Meier, and D. Nüesch, “Vibration and rotation in millimeter-wave sar,” *IEEE trans. Geoscience and Remote Sensing*, vol. 45, no. 2, Feb. 2007.
- [25] R. K. Raney, “Synthetic aperture imaging radar and moving targets,” *IEEE trans. on Aerospace and Electronic Systems*, vol. 7, no. 3, pp. 499–505, May 1971.
- [26] J. G. Vargas-Rubio and B. Santhanam, “On the multiangle centered discrete fractional fourier transform,” *IEEE Signal Processing Letters*, vol. 12, no. 4, pp. 273–276, April 2005.
- [27] P. Flandrin, *Time-Frequency/Time-Scale Analysis.*, ser. Wavelet Analysis and Its Applications. Academic Press, 1999, no. v. 10.
- [28] J. G. Vargas-Rubio and B. Santhanam, “An improved spectrogram using the multiangle centered discrete fractional fourier transform,” in *Proceedings. (ICASSP '05). IEEE International Conference on Acoustics, Speech, and Signal Processing, 2005.*, vol. 4, March 2005, pp. iv/505–iv/508 Vol. 4.

References

- [29] A. Jelili, B. Santhanam, and M. Hayat, “Limitations and capabilities of the slanted spectrogram analysis tool for sar-based detection of multiple vibrating targets,” in *2014 48th Asilomar Conference on Signals, Systems and Computers*, Nov 2014, pp. 172–176.
- [30] O. Agcaoglu, B. Santhanam, and M. Hayat, “Improved spectrograms using the discrete fractional fourier transform,” in *2013 IEEE Digital Signal Processing and Signal Processing Education Meeting (DSP/SPE)*, Aug 2013, pp. 80–85.
- [31] A. Gron, *Hands-On Machine Learning with Scikit-Learn and TensorFlow: Concepts, Tools, and Techniques to Build Intelligent Systems*, 1st ed. O’Reilly Media, Inc., 2017.
- [32] M. Abadi, A. Agarwal, P. Barham, E. Brevdo, Z. Chen, C. Citro, G. S. Corrado, A. Davis, J. Dean, M. Devin, S. Ghemawat, I. Goodfellow, A. Harp, G. Irving, M. Isard, Y. Jia, R. Jozefowicz, L. Kaiser, M. Kudlur, J. Levenberg, D. Mané, R. Monga, S. Moore, D. Murray, C. Olah, M. Schuster, J. Shlens, B. Steiner, I. Sutskever, K. Talwar, P. Tucker, V. Vanhoucke, V. Vasudevan, F. Viégas, O. Vinyals, P. Warden, M. Wattenberg, M. Wicke, Y. Yu, and X. Zheng, “TensorFlow: Large-scale machine learning on heterogeneous systems,” 2015, software available from tensorflow.org. [Online]. Available: <http://tensorflow.org/>
- [33] H. V. Poor, *An introduction to signal detection and estimation*. Springer Science & Business Media, 2013.
- [34] C. L. DiMonte and K. S. Arun, “Tracking the frequencies of superimposed time-varying harmonics,” in *International Conference on Acoustics, Speech, and Signal Processing*, Apr 1990, pp. 2539–2542 vol.5.
- [35] M. W. Y. Poon, “A clutter suppression scheme for high frequency (hf) radar,” *Master’s thesis*, Faculty of Engineering and Applied Science, Memorial University of Newfoundland, Newfoundland and Labrador, Canada, 1991.
- [36] M. W. Y. Poon, R. H. Khan, and S. Le-Ngoc, “A singular value decomposition (svd) based method for suppressing ocean clutter in high frequency radar,” *IEEE Transactions on Signal Processing*, vol. 41, no. 3, pp. 1421–1425, Mar 1993.
- [37] R. H. Khan, “Ocean-clutter model for high-frequency radar,” *IEEE Journal of Oceanic Engineering*, vol. 16, no. 2, pp. 181–188, Apr 1991.
- [38] R. Khan, D. Power, and J. Walsh, “Ocean clutter suppression for an hf ground wave radar,” in *Electrical and Computer Engineering, 1997. Engineering Innovation: Voyage of Discovery. IEEE 1997 Canadian Conference on*, vol. 2, May 1997, pp. 512–515 vol.2.

References

- [39] D. Boutte and B. Santhanam, “A feature weighted hybrid ica-svm approach to automatic modulation recognition,” in *2009 IEEE 13th Digital Signal Processing Workshop and 5th IEEE Signal Processing Education Workshop*, Jan 2009, pp. 399–403.
- [40] F. Auger and P. Flandrin, “Improving the readability of time-frequency and time-scale representations by the reassignment method,” *IEEE Transactions on Signal Processing*, vol. 43, no. 5, pp. 1068–1089, May 1995.
- [41] T. Claasen and W. Mecklenbrauker, “The wigner distribution—a tool for time-frequency signal analysis,” *Philips J. Res*, vol. 35, no. 3, pp. 217–250, 1980.
- [42] V. Namias, “The fractional order fourier transform and its applications to quantum mechanics,” *J. Inst. Math Appl.*, vol. 25, pp. 241–265, 1980.
- [43] B. Santhanam and J. H. McClellan, “The discrete rotational fourier transform,” *IEEE Trans. Signal Processing*, vol. 44, no. 4, pp. 994–998, 1996.
- [44] S. C. Pei and J. J. Ding, “Relations between fractional operations and time-frequency distributions and their applications,” *IEEE trans. Signal Processing*, vol. 49, pp. 1638–1655, 2001.
- [45] J. G. Vargas-Rubio and B. Santhanam, “On the multiangle centered discrete fractional fourier transform,” *IEEE Signal Processing Letters*, vol. 12, pp. 273–276, 2005.
- [46] —, “An improved spectrogram using the multiangle centered discrete fractional fourier transform,” *Proc. ICASSP-05*, vol. 4, pp. 505–508, 2005.
- [47] —, “The centered discrete fractional fourier transform and linear chirp signals,” *Proc. 11th DSP Workshop*, pp. 163–167, 2004.
- [48] L. R. Rabiner, R. W. Schafer, and C. M. Rader, “The chirp z-transform algorithm,” *IEEE trans. Audio Electroacoustics*, vol. 17, no. 2, pp. 86–92, 1969.
- [49] A. V. Oppenheim, R. W. Schafer, and J. R. Buck, *Discrete-Time Signal Processing*, 2nd ed. Upper Saddle River, New Jersey: Prentice Hall Inc., 2002.
- [50] L. S. Reddy, B. Santhanam, and M. M. Hayat, “Multicomponent chirp demodulation using discrete fractional fourier transform,” in *Digital Signal Processing Workshop, 12th*, 2006, pp. 418–422, doi: 10.1109/DSPWS.2006.265423.
- [51] B. Santhanam, T. S. Santhanam, and S. Mandai, “On the effects of windowing on the discretization of the fractional fourier transform,” in *2017 51st Asilomar Conference on Signals, Systems, and Computers*, Oct 2017, pp. 233–237.

References

- [52] S. Mandal, “On improved accuracy chirp parameter estimation using the dfrft with application to sar-based vibrometry,” *2018 52nd Asilomar Conference on Signals, Systems, and Computers*, pp. 1098–1102, 2018.